Investigating the relationship between kimberlites and large low shear velocity provinces over the African continent

by

Vivian Onyinye Nechi

B.S., Nnamdi Azikiwe University, 2021

A THESIS

submitted in partial fulfillment of the requirements for the degree

MASTER OF SCIENCE

Department of Geology
College of Arts and Sciences

KANSAS STATE UNIVERSITY
Manhattan, Kansas

2026

Approved by:

Major Professor
Dr. Claudia Adam

Copyright

© Vivian Nechi 2026.

Abstract

Kimberlites are relatively rare ultramafic igneous rocks commonly emplaced on Archean cratons. They are widely distributed, and several hypotheses have been proposed to explain their emplacement. In this study, we provide new constraints on the African kimberlites' emplacement by backtracking their locations using the free GPlately software, as well as a kinematic model that allows us to go as far back as 1,800 Myr. By considering several new, state-of-the-art tomography models, we quantitatively assess the correlation between Large Low Shear Velocity Provinces (LLSVPs) and backtracked kimberlite locations. Most kimberlites emplaced over the African continent were generated during the 260-0 Myr period (~59%). During this period, most of the kimberlites were generated on the African LLSVPs or along their margins. Our results indicated that the African LLSVPs have remained stable for at least 260 Myr. In contrast, kimberlites older than 260 Ma are mostly not associated with LLSVPs. More precisely, kimberlites emplaced between 590 and 490 Myr show no association with LLSVPs, presenting an intriguing pattern, as the present-day locations of these kimberlites seem to define a NE-SW alignment. We consider constraints from lithosphere-asthenosphere boundary (LAB) and rifting to see if they can account for the kimberlite within this interval. Indeed, our results show that edge-driven convection (EDC) may have played a role in the emplacement of some kimberlite clusters, but there is no clear indication of that for kimberlites emplaced between 590 and 490 Myr. In addition, we show that the comparison between rift and present-day location of kimberlites suggests that the African kimberlites generally emplaced far away from rifts, thus negating the rift's influence on their emplacement. However, rifts may have helped the emplacement of kimberlites with ages between 590 and 490 Myr.

Table of Contents

List of Figures vi
List of Tables xiii
Acknowledgements xiv
Dedication xv
Chapter 1 - Introduction 1
Chapter 2 - Background 6
2.1 Previous Models Proposed for Kimberlite Emplacement 6
2.1.1 Mantle Plumes 6
2.1.2 Subduction Fluids 8
2.1.3 Large Low Shear Velocity Province 9
2.1.4 Edge-driven Convection (EDC) 12
2.1.5 Kimberlites and Continental Rifting 13
Chapter 3 - Methods 15
3.1 Kimberlite Database and Clusters 15
3.2 Kinematic Models 18
3.3 Plate Reconstructions Using GPlates and the GPlates Web Service (GWS) 20
3.4 GPlately 22
3.5 Seismic Tomography Models 22
3.6 Lithosphere-asthenosphere boundary (LAB) 25
3.7 Method for Quantitative Assessment of Correlation Between Kimberlites and LLSVPs .. 26
3.8 African Rifts Digitization 26
Chapter 4 - Results 28
4.1 Correlation between backtracked kimberlite positions and present-day LLSVPs locations 29
4.1.1 Influence of the tomography models used to assess the correlation between backtracked kimberlites and LLSVPs 30
4.1.2 Periods defined by looking at the correlation between backtracked kimberlites positions and LLSVPs 33

4.1.3 Influence of the threshold value, *dvs,* used to assess the correlation between backtracked kimberlites and LLSVPs 36
4.2 Correlations between present-day kimberlite locations and LAB 37
4.3 Correlation between present-day kimberlite locations and rifts 39
Chapter 5 - Discussion 42
5.1 The spatio-temporal distribution of backtracked kimberlite locations and LLSVPs 42
5.2 LAB gradient and temporal distribution of kimberlite locations. 51
5.3 Rifting and temporal distribution of kimberlite locations 54
Chapter 6 - Conclusion 58
References 61
Appendix A - Cluster Description 71
Appendix B - Results for “unclustered” kimberlites 106

List of Figures

Figure 2.1: Great Meteor hotspot track and the emplacement of Rankin, Attawapiskat, and Kirkland Lake kimberlites; from Heaman and Kjarsgaard (2000). 7
Figure 2.2: Kimberlite corridor and distribution of kimberlites, lamproites, and volcanics on the North American plate with the possible location of the Juan de Fuca (JDF) plate. Red symbols indicate Cretaceous ages; white symbols indicate Cenozoic ages (from Currie and Beaumont, 2011). 9
Figure 2.3: Reconstructed kimberlite locations and LLSVPs (from Giuliani et al., 2021). The yellow circles represent kimberlites with a PREMA-like composition and an association with LLSVPs at the time of eruption, whereas the black diamonds represent those lacking a PREMA-composition. The color map shows the seismic velocity anomalies. 10
Figure 2.4: Correlation between LLSVPs and backtracked kimberlite positions from Adam and Kempton (2025). The colormap is the seismic velocity anomaly, dvs, near the core-mantle boundary extracted from the TX2019slab tomography model (Lu et al., 2019). The LLSVP locations, associated with negative seismic velocity anomalies, dvs, are reported in red. The present-day and backtracked locations of kimberlites are displayed by purple circles and black diamonds, respectively. Panels a-e show the reconstruction for different time periods. 12
Figure 2.5: Model of the flow field (arrows) for edge-driven convection from King and Anderson (1998). The arrows represent the flow created by variations in the lithosphere thickness. .. 13
Figure 3.1: Kimberlite database used in this study over the African continent. Data presented are from Tappe et al. (2018). The figure summarizes the defined clusters. The color circles display the ages and locations of kimberlites. The numbers are the number of clusters created in our study. The grey colormap shows the topography; data from Tozer et al. (2019). The yellow lines are the country boundaries; data from ICPAC GEOPORTAL. (a) Global view over the African continent; (b) Enlarged view of central-southern African continent; (c) Enlarged view of southwestern Africa. 17
Figure 3.2: Seismic tomography models considered in this study. (a) SAVANI tomography model (Auer et al., 2014), (b) TX2019slab tomography model (Lu et al., 2019), and (c)

SPiRaL tomography model (Simmons et al., 2021), at a depth of ~2800 km. The LLSVP locations are reported in red (region associated with negative seismic velocity anomalies, *dvs*). The blue line represents the 0 isobath; data from Tozer et al. (2019). 24
Figure 3.3: Lithosphere-Asthenosphere Boundary (LAB) and LAB gradient. LAB shown in panel (a) obtained using data from Priestley et al. (2024). Panel (b) shows the corresponding LAB gradient shown in panel. Country boundaries are shown as white lines in (a) and black lines in (b). 25
Figure 3.4: The African Rift System; data from Sengör and Natalin. (2000), showing digitized rifts colored by age. Precambrian age is reported in green, Paleozoic is reported in yellow, Mesozoic is reported in magenta, and Cenozoic is reported in cyan. The grey co colormap shows the topography; data from Tozer et al. (2019). 27
Figure 4.1: Kimberlite database used in this study over the African continent. The figure summarizes the defined clusters (see text). The color circles display the ages and locations of kimberlites. The numbers are some of the cluster numbers created in our study. The grey colormap shows the topography; data from Tozer et al. (2019). The yellow lines are the country boundaries; data from ICPAC GEOPORTAL. 29
Figure 4.2: Correlation between LLSVPs and backtracked kimberlite positions. The colormap shows the seismic velocity anomaly, dvs, near the core-mantle boundary extracted from three different global tomography models: SPiRaL (Simmons et al., 2021), TX2019slab (Lu et al., 2019), and SAVANI (Auer et al., 2014) as shown in panels a-c. The LLSVP locations are reported in red, that is, associated with negative seismic velocity anomalies, *dvs*. The *dvs* = − 1% isocontour is reported in black. Isobath 0 is reported in blue. The present-day and backtracked locations of kimberlites emplaced over LLSVPs are displayed by green circles and black diamonds, respectively, while the present-day and backtracked locations of kimberlites not emplaced over LLSVP are displayed in blue circles and white diamonds. . 32
Figure 4.3: Correlation between LLSVPs and backtracked kimberlite positions. The colormap shows the seismic velocity anomaly, dvs, near the core-mantle boundary provided by the TX2019slab tomography model (Lu et al., 2019). The LLSVP locations are reported in red, that is, associated with negative seismic velocity anomalies, dvs. The dvs = − 1% isocontour is reported in black. Isobath 0 is reported in blue. The present-day and backtracked locations of kimberlites emplaced over LLSVPs are displayed in green circles and black diamonds,

respectively, while the present-day and backtracked locations of kimberlites not emplaced over LLSVP are displayed in blue circles and white diamonds. Panels (a-h) show the reconstruction for different time periods. 34
Figure 4.4:Quantitative correlation between backtracked kimberlites positions and LLSVPs as a function of the kimberlites' age. The kimberlites clusters emplaced over LLSVPs are reported in panel a, while the ones not emplaced over LLSVPs are displayed in panel b. The correlation is based on three tomography models. The color lines represent the 260, 490, 590, 1100, 1160, 1620, 1680, and 1800 Ma ages discussed in the text. 35
Figure 4.5: Influence of varying threshold value, dvs_{min}, on the correlation between backtracked kimberlites and LLSVPs. The kimberlites clusters emplaced over LLSVPs are reported in panel a, while those not emplaced over LLSVPs are displayed in panel b. The correlation is based on three tomography models. The color lines represent the 260, 490, 590, 1110, 1160, 1620, 1680, and 1800 Ma. 37
Figure 4.6: Lithosphere-Asthenosphere Boundary (LAB), LAB horizontal gradient, and kimberlite distributions. The color circles display the ages and locations of kimberlites according to the database developed for this study (see text). The LAB shown in panel (a) is obtained using the data from Priestley et al. (2024). Panel (b) shows the LAB horizontal gradient. Country boundaries are shown as white lines in (a) and black lines in (b). 38
Figure 4.7: Lithosphere-Asthenosphere Boundary (LAB), LAB horizontal gradient, and distribution of kimberlites with ages between 1800 and 260 Ma. Major cratonic regions: West African craton, Congo craton, and Kalahari craton are indicated for reference. The color circles display the ages and locations of kimberlites according to the database developed for this study (see text). The LAB shown in panel (a) is obtained using the data from Priestley et al. (2024). Panel (b) shows the LAB horizontal gradient. Country boundaries are shown as white lines in (a) and black lines in (b)..... 39
Figure 4.8: The African Rift System; data from Sengör and Natalin (2000), showing digitized rifts colored by age and the ages and locations of kimberlite clusters. Precambrian age is reported in green, Paleozoic is reported in yellow, Mesozoic is reported in magenta, and Cenozoic is reported in cyan. The grey colormap shows the topography; data from Tozer et al. (2019). 40

Figure 5.1: Correlation between LLSVPs and backtracked kimberlite positions. The colormap shows the seismic velocity anomaly, *dvs*, near the core-mantle boundary. The data are extracted from the TX2019slab tomography model (Lu et al. 2019). The LLSVP locations are reported in red, that is, associated with negative seismic velocity anomalies, *dvs*. The *dvs* = − 1% isocontour is reported in black. Isobath 0 is reported in blue. The present-day and backtracked locations of kimberlites emplaced over LLSVPs are displayed by green circles and black diamonds, respectively, while the present-day and backtracked locations of kimberlites not emplaced over LLSVP are displayed in blue circles and white diamonds. Panels (a-h) show the reconstruction for different periods. 44

Figure 5.2: Quantitative correlation between backtracked kimberlites positions and LLSVPs as a function of the kimberlites' age. The kimberlites clusters emplaced over LLSVPs are reported in panel a, while the ones not emplaced over LLSVPs are displayed in panel b. The correlation is based on three tomography models. The color lines represent the 260, 490, 590, 1110, 1160, 1620, 1680, and 1800 Ma, respectively. 45

Figure 5.3: Correlation between LLSVPs and backtracked kimberlite positions. The colormap shows the seismic velocity anomaly, dvs, near the core-mantle boundary. The data are extracted from the TX2019slab tomography model (Lu et al. 2019). The LLSVP locations are reported in red, that is, associated with negative seismic velocity anomalies, *dvs*. The *dvs* = − 1% isocontour is reported in black. Isobath 0 is reported in blue. The present-day and backtracked locations of kimberlites emplaced over LLSVPs are displayed by green circles and black diamonds, respectively, while the present-day and backtracked locations of kimberlites not emplaced over LLSVP are displayed in blue circles and white diamonds. Panels a and b show the reconstruction for different time periods. 48

Figure 5.4: Lithosphere-Asthenosphere Boundary (LAB), LAB gradient, and kimberlite clusters not emplaced over LLSVPs. The color circles display the ages and locations of kimberlites (1800-0 Ma not emplaced over LLSVPs). LAB shown in panel (a) obtained using data from Priestley et al. (2024). Panel (b) shows the corresponding LAB gradient. Country boundaries are shown as white lines in (a) and black lines in (b)..... 52

Figure 5.5: Lithosphere-Asthenosphere Boundary (LAB), LAB gradient, and kimberlite clusters. The color circles display the ages and locations of kimberlites clusters with ages between 590 and 490 Ma. LAB shown in panel (a) obtained using data from Priestley et al. (2024).

Panel (b) shows the corresponding LAB gradient. Country boundaries are shown as white lines in (a) and black lines in (b). 53
Figure 5.6: Zoom on the southern part of the Lithosphere-Asthenosphere Boundary (LAB) gradient showing the kimberlite clusters with ages between 590 and 490 Ma. The color circles display the ages and locations of kimberlites. LAB shown in panel (a) obtained using data from Priestley et al. (2024). Panel (b) shows the corresponding LAB gradient shown in panel. Country boundaries are shown as white lines in (a) and black lines in (b). 53
Figure 5.7: Relationship between rift systems and kimberlite locations (590-490 Ma). Precambrian age (~ >541Ma) is reported in green, Paleozoic (~541-252 Ma) is reported in yellow, Mesozoic (~252-66 Ma) is reported in magenta, and Cenozoic (~66 to present) is reported in cyan. Open green circles show kimberlite locations from the 490–590 Ma interval. The grey colormap shows the topography; data from Tozer et al. (2019)..... 55
Figure 5.8: Locations of different blocks constituting the present-day African plate at selected periods and backtracked kimberlite for different time periods reported in each panel (a-e). The present-day locations of the continents are shown in grey, while the reconstructed African blocks are shown in blue.....**Error! Bookmark not defined.**

Appendix Figure A.1: Kimberlite database designed in this study over the African continent based on data from Tappe et al. (2018). The color circles display the ages and locations of kimberlites. The numbers are the number of clusters created in our study. The grey colormap shows the topography: data from Tozer et al. (2019). The yellow lines are the country boundaries (data from ICPAC GEOPORTAL). (a) Global view over the African continent; (b) Enlarged view of central-southern African continent; (c) Enlarged view of southwestern Africa. 72
Appendix Figure A.2: Database designed by Dalton et al. (2024) over the African continent. The color circles display the ages and locations of kimberlites. The grey colormap shows the topography: data from Tozer et al. (2019). The yellow lines are the country boundaries (data from ICPAC GEOPORTAL). 73
Appendix Figure B.1: The kimberlite database over the African continent. The color circles display the ages and locations of kimberlites. The grey colormap shows the topography;

data from Tozer et al. (2019). The yellow lines are the country boundaries; data from ICPAC GEOPORTAL 106
Appendix Figure B.2: Correlation between LLSVPs and backtracked kimberlite positions for the "unclustered data". The colormap shows the seismic velocity anomaly, dvs, near the core-mantle boundary provided by the TX2019slab tomography model (Lu et al., 2019). The LLSVP locations are reported in red, that is, associated with negative seismic velocity anomalies, dvs. The dvs = − 1% isocontour is reported in black. Isobath 0 is reported in blue. The present-day and backtracked locations of kimberlites emplaced over LLSVPs are displayed in green circles and black diamonds, respectively, while the present-day and backtracked locations of kimberlites not emplaced over LLSVP are displayed in blue circles and white diamonds. Panels (a-h) show the reconstruction for different time periods..... 107
Appendix Figure B.3: Quantitative correlation between backtracked kimberlites positions and LLSVPs as a function of the kimberlites' age. The kimberlites clusters emplaced over LLSVPs are reported in panel a, while the ones not emplaced over LLSVPs are displayed in panel b. The correlation is based on three tomography models. The color lines represent the 260, 490, 590, 1110, 1160, 1620, 1680, and 1800 Ma, respectively. 108
Appendix Figure B.4: Correlation between LLSVPs and all backtracked kimberlite positions. The colormap shows the seismic velocity anomaly, *dvs*, near the core-mantle boundary. The data are extracted from the TX2019slab tomography model (Lu et al. 2019). The LLSVP locations are reported in red, that is, associated with negative seismic velocity anomalies, *dvs*. The *dvs* = − 1% isocontour is reported in black. Isobath 0 is reported in blue. The present-day and backtracked locations of kimberlites emplaced over LLSVPs are displayed by green circles and black diamonds, respectively, while the present-day and backtracked locations of kimberlites not emplaced over LLSVP are displayed in blue circles and white diamonds. Panels a and b show the reconstruction for different time periods..... 109
Appendix Figure B.5: Lithosphere-Asthenosphere Boundary (LAB), LAB gradient, and all kimberlite not emplaced over LLSVPs. The color circles display the ages and locations of kimberlites (1800-0 Ma not emplaced over LLSVPs). LAB shown in panel (a) obtained using data from Priestley et al. (2024). Panel (b) shows the corresponding LAB gradient. Country boundaries are shown as white lines in (a) and black lines in (b)..... 110

Appendix Figure B.6: Lithosphere-Asthenosphere Boundary (LAB), LAB gradient, and kimberlite clusters. The color circles display the ages and locations of kimberlites clusters with ages between 590 and 490 Ma. LAB shown in panel (a) obtained using data from Priestley et al. (2024). Panel (b) shows the corresponding LAB gradient. Country boundaries are shown as white lines in (a) and black lines in (b)..... 111
Appendix Figure B.7: Relationship between rift systems and kimberlite locations (590-490 Ma). Precambrian age (~ >541Ma) is reported in green, Paleozoic (~541-252 Ma) is reported in yellow, Mesozoic (~252-66 Ma) is reported in magenta, and Cenozoic (~66 to present) is reported in cyan. The color circles show kimberlite locations from the 490–590 Ma interval. The grey colormap shows the topography; data from Tozer et al. (2019)..... 112

List of Tables

Table 5.1: Summary of the correlation between backtracked kimberlite positions and LLSVPs 49

Appendix Tables A.1: Our kimberlite cluster dataset. The columns display the present-day location of kimberlites (columns 1 and 2), the age of kimberlites (column 3), the corresponding line numbers in Tappe et al. (2018) Supplementary Table A (column 4), the backtracked location of kimberlites (columns 5 and 6), and the associated cluster number (column 7) 100

Appendix Table B.1: Summary of the correlation between all backtracked kimberlite positions and LLSVPs 110

Appendix Table B.2: All our kimberlite dataset. The columns display the present-day location of kimberlites (columns 1 and 2), the age of kimberlites (column 3), the corresponding line numbers in Tappe et al. (2018) Supplementary Table A (column 4), and the backtracked location of kimberlites (columns 5 and 6) 112

Acknowledgements

I would like to thank God for always coming through! For the strength, wisdom, grace, and most importantly, perseverance.

My sincere and deepest appreciation goes to my amazing advisor, Dr. Claudia Adam, for her encouragement, guidance, and unwavering support throughout the research process. Her dedication and insights were invaluable to me.

I am also grateful to my advisory committee members, Dr. Pamela Kempton and Dr. Andrea Moeller, for their time, thoughtful critiques, and invaluable contributions, which helped improve this research.

Special thanks to Dr. Helene Avocat for her assistance with rift digitization, which contributed significantly to this research.

I would also like to acknowledge the Department of Geology at Kansas State University for providing a supportive academic environment.

Finally, to my friends and colleagues, thank you for the good times.

Dedication

I dedicate this thesis to my family for their love and encouragement. Their sacrifices and moral support have been my strength throughout this journey.

Chapter 1 - Introduction

Kimberlites are rare, volatile, and crystal-rich magmas, derived from the mantle (Golovin et al., 2018). They are ultrabasic igneous rocks found on every continent and generally occur where the continent has a thick Archean lithospheric keel (Tappe et al., 2018). They are rich in volatiles, such as CO_2 and H_2O (Foley et al., 2019), but silica and alkaline poor (Francis and Patterson, 2009). Kimberlites normally form in the mantle between depths of 160 km and 300 km (Rohrbach and Schmidt, 2011; Giuliani et al., 2023), therefore, at high temperatures and pressures, but the precise conditions remain a matter of debate. According to Jollands et al. (2018), kimberlites can form at temperatures ranging from 1100-1300°C, whereas Stamm and Schmidt (2017) argue for temperatures of 1400-1650°C. Pressures at which kimberlite melts form range from 2.5 GPa (Russell et al., 2012) to 8-10 GPa (Francis and Patterson, 2009).

The geochemical characteristics of kimberlites have been studied by numerous authors (e.g., le Roex, 2003; Pearson et al., 2019; Giuliani et al., 2021; Dalton et al., 2022; Giuliani et al, 2025). The textural, mineralogical, and geochemical complexity of kimberlites has made classification difficult and several different approaches to classification have been proposed. According to Becker and le Roex (2006), Mitchell (1995), Smith (1983), and others, kimberlites sensu stricto (also known as Group-I or archetypal kimberlites) are a group of silica-undersaturated, ultramafic, volatile-rich ($CO_2 \pm H_2O$), and potassic (i.e., low Na_2O/K_2O ratios) igneous rocks. They are clearly depleted in heavy rare earth elements (HREEs) and enriched in light rare earth elements (LREEs) as compared to other ultramafic rocks (Dawson, 1980; le Roex et al., 2003; Mitchell, 1986). The presence of macrocrystic and occasionally megacrystic minerals arranged in a fine-grained groundmass gives kimberlites their characteristic inequigranular textures. Anhedral forsteritic olivine, enstatite, Cr-poor clinopyroxene, phlogopite, Cr-poor

titanian pyrope, ilmenite, Ti-poor chromite, and zircon are common phases included in the macro/megacryst assemblage (Gurney et al., 1979; Harte and Gurney, 1981; Mitchell, 1986). Olivine is usually the most abundant (~25–60 vol.%) mineral, with both macrocrystic and magmatic origins possible (Arndt et al., 2010; Brett et al., 2009; Kamenetsky et al., 2008; Moore, 1988; Pilbeam et al., 2013). Phlogopite, apatite, carbonate (such as dolomite/calcite), perovskite, and serpentine are typical constituents of the groundmass. Additionally, xenoliths from the mantle (such as peridotite and eclogite) and crust (such as country rock) are frequently found in kimberlites.

The name 'kimberlite' comes from the town Kimberley, South Africa, where the rocks were first mined for diamonds (Smit and Shirey, 2019). Therefore, some kimberlites are economically viable for the diamonds found in them. The presence of diamonds indicates that kimberlite melts form at depth greater than diamond-graphite phase boundary typically corresponding to depths of approximately 150-300 km; as such, they are typically associated with thick cratonic lithosphere and have been interpreted to have formed at the base of the lithosphere within the asthenospheric mantle (Mitchell, 1991).

The deep origin of kimberlites means that they can provide valuable insights into deep Earth processes and information about the Earth's lithospheric and asthenospheric mantle. Kimberlitic magmatism has occurred for the last ~2.85 Gyr, although the frequency of eruptions has apparently increased in the last 1.2 Gyr (Tappe et al., 2018; Heaman et al., 2019; Kjarsgaard et al., 2022). Surprisingly, kimberlitic magmatism does not occur continuously. Instead, we observe periods of enhanced kimberlitic activity and periods where few kimberlites are emplaced (Tappe et al., 2018). Surprisingly, kimberlitic magmatism does not occur continuously. Instead,

we observe periods of enhanced kimberlitic activity, and periods where few kimberlites emplaced (Tappe et al., 2018).

The study of kimberlites is important as they commonly contain abundant mantle and crustal xenoliths and xenocrysts, including diamond, thereby providing unique insights into the nature and processes of the deep crust and lithospheric mantle. This has led kimberlites to attract attention from geoscience and exploration communities, which seek to understand their intermittent relationship with diamond and their ultimate origin.

However, despite more than half a century of research, the origin and emplacement of kimberlites remain a topic of debate. They are commonly associated with thick, stable lithospheric keels beneath Archean cratons, where lithospheric thicknesses may exceed 180–250 km (Kopylova and Caro, 2004; Artemieva, 2009). Yet, kimberlite occurrences are not uniformly restricted to craton interiors, and their emplacement ages are episodic rather than continuous. These observations suggest that lithospheric thickness alone is insufficient to explain kimberlite magmatism.

Recent studies increasingly point to a complex combination of processes that potentially impact kimberlite emplacement that span interactions between lithospheric architecture, plate tectonics, and deep mantle dynamics. In particular, the spatial correlation between reconstructed kimberlite emplacement locations and Large Low Shear Velocity Provinces (LLSVPs) at the core–mantle boundary has renewed interest in the role of deep mantle structure in kimberlite genesis (Burke and Torsvik, 2004; Torsvik et al., 2014; Giuliani et al., 2021; Adam and Kempton, 2025). At the same time, continental rifting and supercontinent breakup have been identified as potential triggers that destabilize cratonic lithosphere and promote kimberlite magmatism (Tappe et al., 2018; Gernon et al., 2023).

Africa provides an exceptional natural laboratory for investigating the relative contributions from these processes. In Africa, kimberlite occurrences span from the Archean to the Mesozoic. They are primarily concentrated within or near stable cratonic regions such as the Kaapvaal, Zimbabwe, Congo, and West African cratons. The African plate has undergone a long tectonic history that includes the formation of Archean cratons, Proterozoic orogenesis, the assembly of Gondwana, and Mesozoic continental breakup. Moreover, beneath Africa lies one of the most prominent LLSVPs in the mantle, which is associated with long-wavelength topography and intraplate magmatism, including the African Superswell (Nyblade and Robinson, 1994; Ritsema et al., 1999; Gurrnis et al., 2000). Understanding how kimberlite emplacement relates to this changing tectonic and mantle framework is critical for developing a comprehensive model of kimberlite genesis.

In this research, we investigate the relationship between kimberlite emplacement in the African continent and the large low shear velocity provinces, LLSVPs, as well as their correlation with rifts and Edge-Driven Convection (EDC). We use kinematic models to backtrack the location of kimberlites at the time of their emplacement. This means we will compute where the African continent was at the time the kimberlites were emplaced. We study the correlation between backtracked kimberlite positions and LLSVPs, derived from seismic tomography models. We undertake a spatiotemporal cluster analysis of the kimberlite fields. Clusters are defined as groups of kimberlites that are close enough in space and time that they could plausibly be attributed to the same initiating event. By using a clustering approach, we mitigate the overrepresentation of similar ages within geographically restricted areas. Additionally, we evaluate the extent to which rifting events influence kimberlite magmatism. This research adopts a predominantly geophysical

approach, integrating plate reconstruction and seismic tomography, aimed at examining the spatial relationship between kimberlites and seismic velocity anomalies in the mantle.

Chapter 2 - Background

2.1 Previous Models Proposed for Kimberlite Emplacement

Several hypotheses have been put forth in the literature to account for kimberlite emplacements Some of these models include mantle plumes (Heaman and Kjarsgaard, 2000; Heaman et al., 2003; Bodur and Flament, 2023), fluids released by low-angle subduction (Currie and Beaumont, 2011), large low shear velocity provinces (LLSVP) (Davies et al., 2015; Giuliani et al., 2021; Adam and Kempton, 2025), and edge-driven convection (EDC) (King and Anderson, 1998; Kjarsgaard et al., 2017; Kempton et al., 2019; Lupini, 2023; Adam and Kempton, 2025). Their spatial and temporal distribution has also been related to tectonic processes involving lithospheric faults formed or reactivated during rifting of continents (Jelsma et al., 2004; Moore et al., 2008; Tappe et al., 2018). In addition, petrological studies provide constraints on the formation of kimberlite melts. In this section, we summarize these models.

2.1.1 Mantle Plumes

Heaman and Kjarsgaard, (2000) hypothesized that kimberlite emplacement may be associated with continental extension triggered by mantle plumes. According to them, there is an age progression in kimberlite magmatism for kimberlites of southeastern Canada, which is consistent with the relative motions of the North America lithospheric plate. This age progression in kimberlite magmatism extends for more than 2000 km from Rankin Inlet through to the Attawapiskat, Kirkland Lake, and Timiskaming fields and is interpreted, in part, to be the continental expression of magmatism linked to the Great Meteor mantle plume hotspot track (Figure 2.1). The authors concluded that most of the kimberlites were generated during enhanced

mantle plume activity associated with the rifting and eventual breakup of the supercontinent Gondwanaland.

Recent geodynamic modelling provides further support for the role of deep mantle upwelling in kimberlite magmatism. Using global mantle convection models driven by a 1-billion-year history of plate motions, Bodur and Flament (2023) demonstrated that broad upwelling above large basal mantle structures (LLSVPs) supplies the thermal energy required for kimberlite melt generation. Their models show that narrow mantle plumes transport chemically distinct material from the core–mantle boundary to shallow depths, consistent with the anomalous geochemical signatures of some kimberlites.

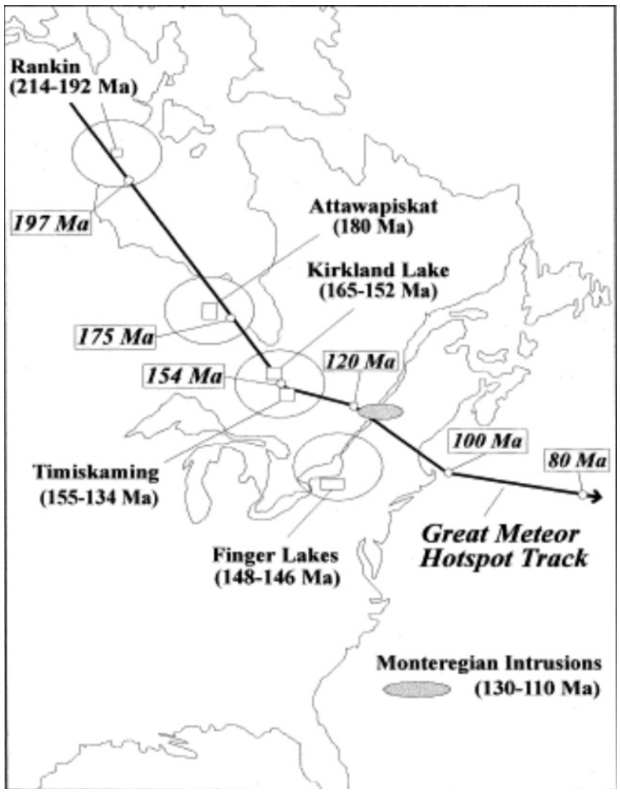


Figure 2.1: Great Meteor hotspot track and the emplacement of Rankin, Attawapiskat, and Kirkland Lake kimberlites; from Heaman and Kjarsgaard (2000).

2.1.2 Subduction Fluids

Currie and Beaumont (2011) proposed that kimberlite emplacement in western North America is a result of low-angle subduction related to dehydration of the subducted slab followed by partial melting of the overlying hydrated mantle. According to the authors, rapid subduction of the oceanic Farallon plate beneath the North American plate allowed some fluids to hydrate the lithosphere, triggering partial melting and kimberlite magmatism. Curie and Beaumont (2011) studied the Cretaceous kimberlite corridor in western North America. Their study supports a causal link between the Farallon plate subduction and Cretaceous kimberlite corridor magmatism within their specified 'corridor.' Figure 2.2 shows the kimberlite corridor and distribution of kimberlites, lamproites, and other volcanics across western North American plate.

McCandless (1999) also stated that kimberlite magmatism is attributed to the subduction of the oceanic Farallon plate beneath the North American plate. There is an indication that the oceanic plate can contain volatiles necessary for triggering deep-mantle magmatism such as kimberlite magmatism (McCandless, 1999).

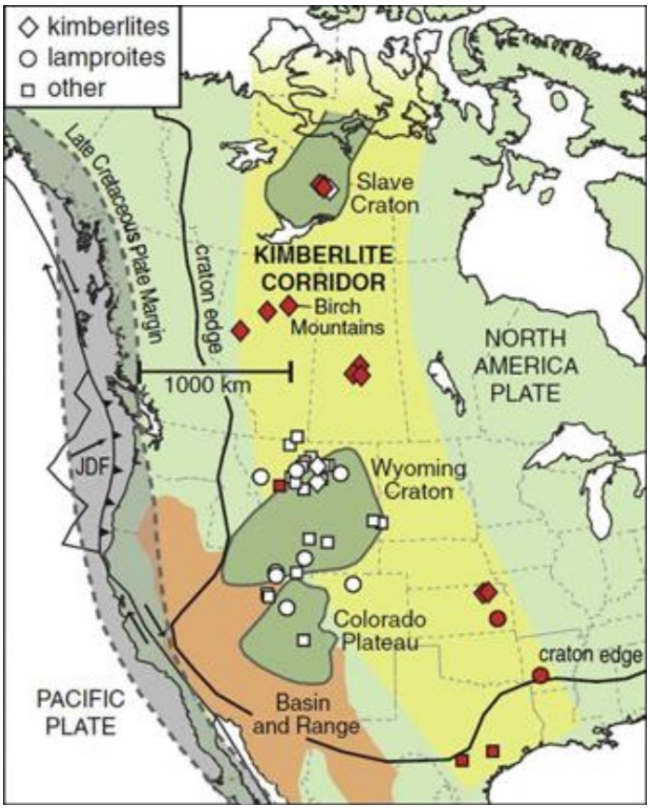


Figure 2.2: Kimberlite corridor and distribution of kimberlites, lamproites, and volcanics on the North American plate with the possible location of the Juan de Fuca (JDF) plate. Red symbols indicate Cretaceous ages; white symbols indicate Cenozoic ages (from Currie and Beaumont, 2011).

2.1.3 Large Low Shear Velocity Province

Another hypothesis is that kimberlites originate along the margins of LLSVPs (Torsvik et al., 2014; Giuliani et al., 2021; Lee, 2022; Adam et al., 2023; Adam and Kempton, 2025). LLSVPs are regions located in the deep mantle, near the core-mantle boundary, that are associated with slow seismic velocities (Davies et al., 2015; McNamara, 2019) (Figure 2.3).

Seismic tomography reveals two prominent mantle heterogeneities, one beneath Africa and the other beneath the Pacific Ocean. They are interpreted as distinct large low shear velocity provinces extending from the core–mantle boundary into the mid-mantle (Ritsema et al., 1999; Davies et al.,

2015). The African LLSVP is associated with elevated mantle temperatures, creating a dynamic uplift. These high topography regions are called the African Superswell (Nyblade and Robinson, 1994; Gurnis et al., 2000).

Some studies suggest that the LLSVPs are long-lived structures that interact dynamically with surface plate motions and subduction histories (Flament et al., 2022; Bodur et al., 2022). Given their deep mantle origin, LLVPs have been proposed as potential source regions influencing kimberlite magmatism. Giuliani et al. (2021) backtracked the locations of kimberlites < 270 Ma and showed that some of them correlate with the location of the African LLSVP (Figure 2.3). They showed that most of the Phanerozoic kimberlites share similar Sr-Nd-Hf isotope signatures with PREMA (prevalent mantle) as well as some OIBs (Ocean-Island Basalt). They interpret this as evidence that these kimberlites are sourced from LLSVPs.

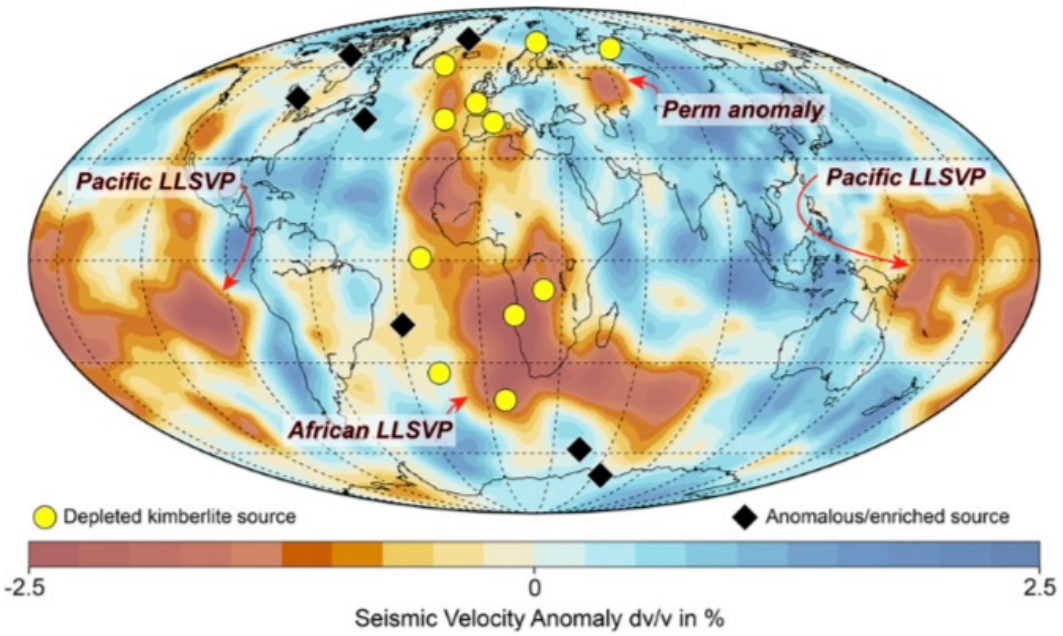


Figure 2.3: Reconstructed kimberlite locations and LLSVPs (from Giuliani et al., 2021). The yellow circles represent kimberlites with a PREMA-like composition and an association with LLSVPs at the time of eruption, whereas the black diamonds represent those lacking a PREMA-composition. The color map shows the seismic velocity anomalies.

The kinematic model used by Guiliani et al. (2021) was designed by Torsvik et al. (2014). In this model, the position of the continent is computed assuming that kimberlite locations correlate with the locations of the LLSVPs, i.e., the Plume Generation Zone (PGZ) method. As pointed out by Adam and Kempton (2025), this assumption makes the logic of the approach for linking kimberlites and LLSVPs circular. It is, therefore, not adequate for studying the hypothesis that kimberlites are correlated with LLSVPs.

Using a more appropriate kinematic model that does not use the PGZ method, i.e., the one developed by Merdith et al. (2021), Adam and Kempton (2025) backtracked kimberlite positions within the North American continent and compared the backtracked kimberlite locations to the location of LLSVPs. They showed that most of the North American kimberlites have been emplaced over LLSVPs and that there is an enhanced kimberlitic activity when the continent migrates over LLSVPs (Figure 2.4). The authors do not rule out that other phenomena may be at play for kimberlite emplacement. In particular, the kimberlites younger than 130 Ma are not emplaced over LLSVPs, but their emplacement can be accounted for by edge-driven convection (Adam and Kempton, 2025).

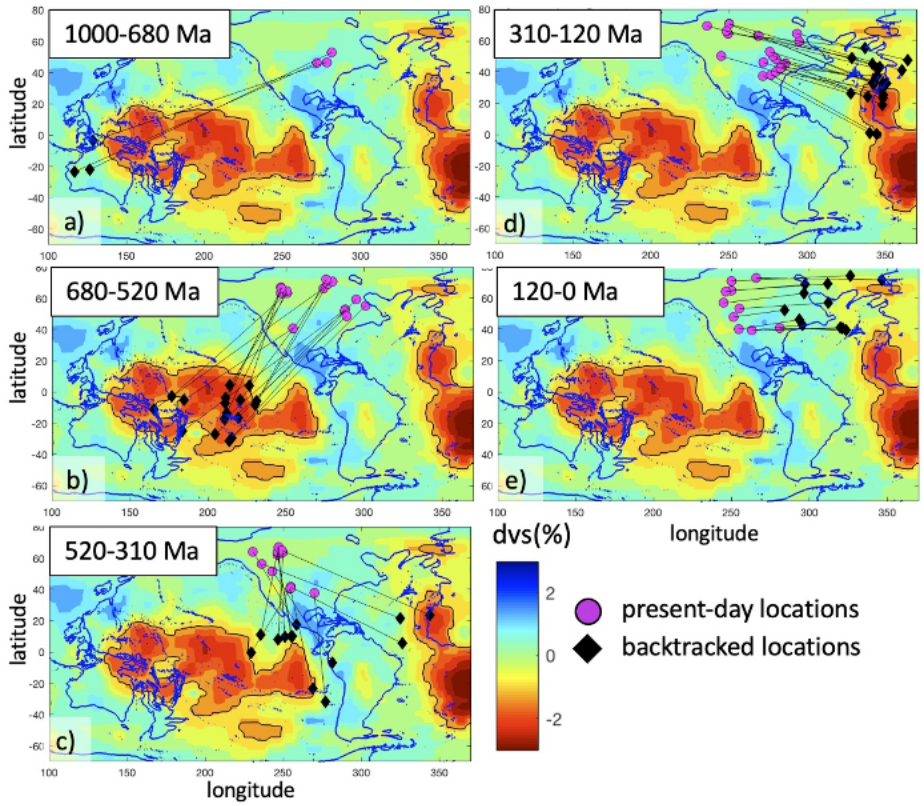


Figure 2.4: Correlation between LLSVPs and backtracked kimberlite positions from Adam and Kempton (2025). The colormap is the seismic velocity anomaly, dvs, near the core-mantle boundary extracted from the TX2019slab tomography model (Lu et al., 2019). The LLSVP locations, associated with negative seismic velocity anomalies, dvs, are reported in red. The present-day and backtracked locations of kimberlites are displayed by purple circles and black diamonds, respectively. Panels a-e show the reconstruction for different time periods.

2.1.4 Edge-driven Convection (EDC)

Edge-driven convection is a convective process that occurs at the boundary between a thick stable lithosphere and a thinner lithosphere and this variation in the lithospheric thickness drives a convection cell that may induce volcanism, as illustrated in Figure 2.5 (King and Anderson, 1998).

King and Anderson (1998) proposed that asthenospheric upwellings, paralleling and controlled by the temperature contrast across the North American continental margin were responsible for formation of the Bermuda and Labrador rises. According to Manjón-Cabeza

Córdoba and Ballmer (2021), EDC may also be at the origin of the Canary Islands volcanism. The emplacement of kimberlites in Kansas has also been explained by EDC (Kempton et al., 2019).

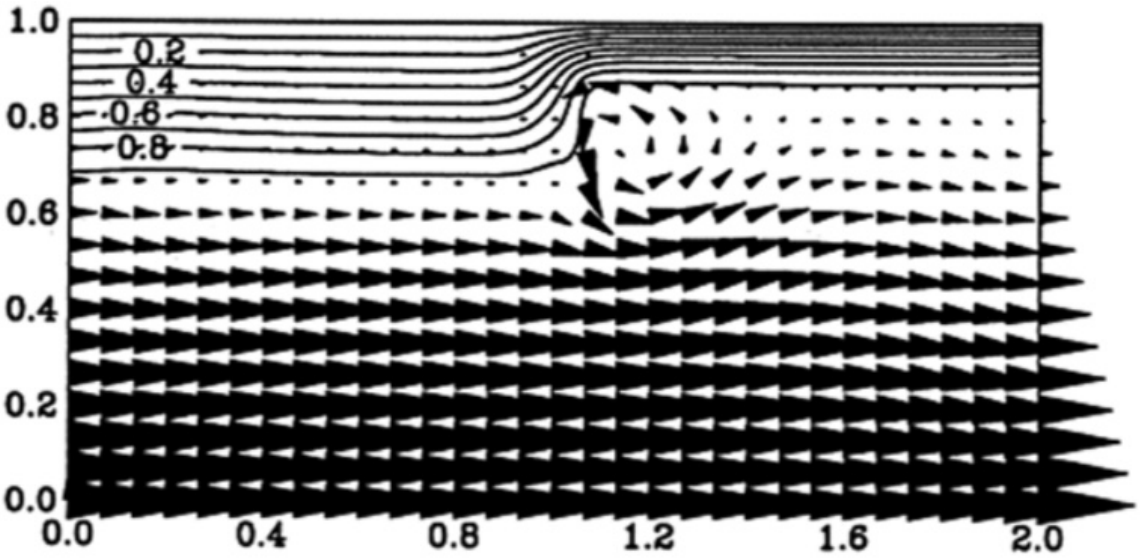


Figure 2.5: Model of the flow field (arrows) for edge-driven convection from King and Anderson (1998). The arrows represent the flow created by variations in the lithosphere thickness**.**

2.1.5 Kimberlites and Continental Rifting

Recent studies have highlighted continental rifting as a critical mechanism linking lithospheric deformation to kimberlite magmatism. Gernon et al. (2023) demonstrated that kimberlite eruptions globally tend to occur approximately 20–40 Myr after the onset of continental breakup. Their geodynamic models show that rifting steepens lithosphere–asthenosphere boundaries, driving convective instabilities that propagate beneath cratonic interiors and destabilize cratonic keels, promoting low-degree, volatile-rich melting consistent with kimberlite compositions.

This rift-induced mantle flow model provides an explanation for kimberlite emplacement without requiring classical mantle plume activity (Gernon et al., 2023). In Africa, major kimberlite emplacement events coincide temporally with Mesozoic rifting associated with the breakup of Gondwana, including the opening of the South Atlantic and Indian oceans (Jourdan et al., 2007; Tappe et al., 2018).

Global reconstructions that integrate plate kinematics with mantle flow modeling further support this interpretation. Bodur et al. (2022) and Grabreck et al. (2022) showed that kimberlite occurrences correlate with regions where reconstructed thick lithosphere overlies zones of enhanced basal mantle flow. These studies suggest that rifting, by reorganizing mantle flow and lithospheric stress fields, plays a fundamental role in controlling kimberlite generation and ascent. Jelsma et al. (2008) argue that kimberlites represent surface expressions of deeper tectonic processes, often coinciding with the assembly or breakup of supercontinents. Using Southern Africa as a type region, they demonstrate that kimberlite magmatism clusters spatially along lithospheric-scale structures such as terrane boundaries, orogenic margins, ancient rifts, and reactivated fracture zones. Flament et al. (2022) further demonstrated that evolving mantle flow driven by subduction and rifting histories can modify basal mantle structures over time, altering mantle upwelling patterns and lithosphere-asthenosphere interactions in ways that control the spatial and temporal distribution of kimberlite potential across supercontinent cycles.

Chapter 3 - Methods

We backtrack the locations of kimberlites across the African continent to better constrain their origin. First, we define kimberlites clusters for kimberlites of similar ages in each region. We then backtrack the positions of these clusters using the open-source GPlates (Gurnis et al., 2012) and GPlately (Mather et al., 2023) softwares, which makes use of the geospatial coordinate locations of the kimberlites, their ages, and two kinematic models designed by Merdith et al. (2021) and Cao et al. (2024). We quantitatively assess the correlation between backtracked kimberlite positions and LLSVP locations using the method designed by Adam and Kempton (2025). Finally, we also investigate the possible correlation between the backtracked kimberlite positions, EDC, and rifts.

3.1 Kimberlite Database and Clusters

For this project, we used the database designed by Tappe et al. (2018). This database is more beneficial than some others available, e.g., Woodhead et al. (2019), Giuliani et al. (2021), or Dalton et al. (2024), as it compiles all the necessary information, including coordinates, ages, and geochronological information. Most kimberlites tend to occur in clusters, with each cluster encompassing several kimberlite samples, sometimes with overlapping ages. Numerous studies show that kimberlitic events last between 13 and 55 Myr. within a single field, and up to 20 Myr. within a single pipe (e.g., Heaman and Kjarsgaard, 2000; Heaman et al., 2015; Kjarsgaard et al., 2017; Ranger et al., 2018; Sarkar et al., 2015; Zurevinski et al., 2008). Therefore, we carry out cluster analysis to mitigate the overrepresentation of similar ages within geographically restricted areas. We note that kimberlite volcanic episodes typically span less than 50 Myr; hence, in our study, we only keep one significant sample per volcanic event and consider that a volcanic event

lasts 50 Myr or less according to the references above and to the method recently developed by Adam and Kempton (2025). The cluster definition is detailed in Appendix A. In this project, we will present and interpret our results for the clusters, but the unclustered data, i.e., all the samples available in Tappe et al. (2018) database, are available in Appendix B and are also analyzed as part of this study.

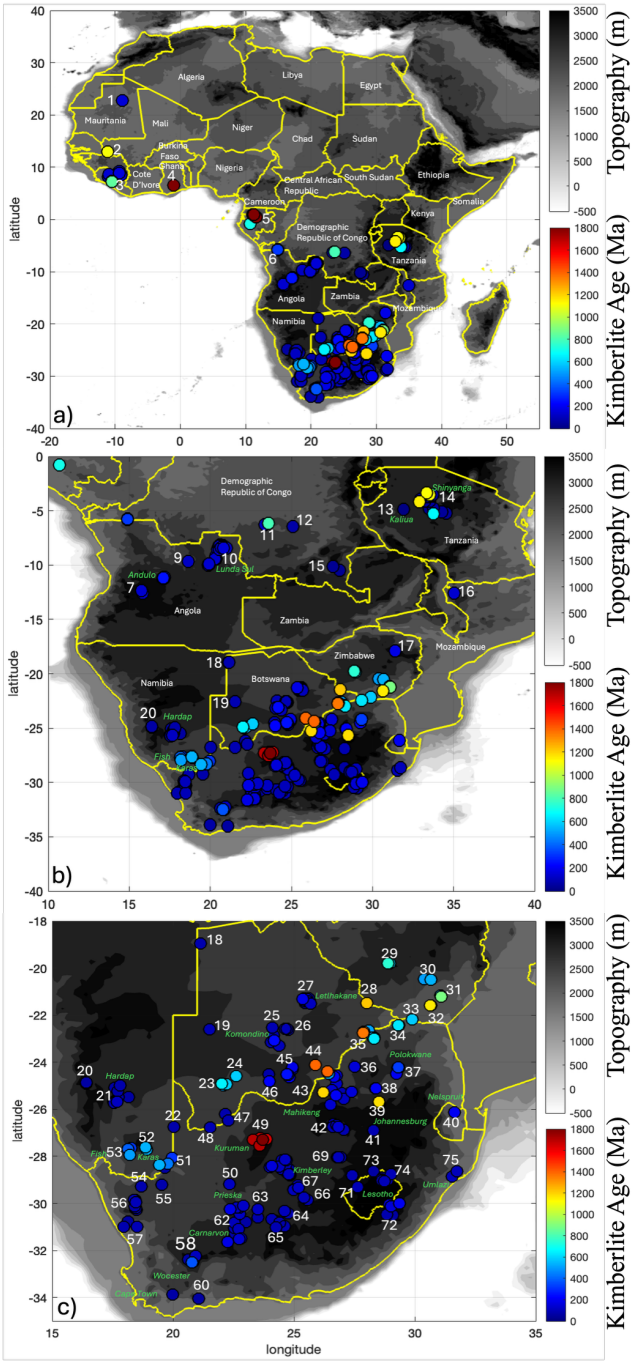


Figure 3.1: Kimberlite database used in this study over the African continent. Data presented are from Tappe et al. (2018). The figure summarizes the defined clusters. The color circles display the ages and locations of kimberlites. The numbers are the number of clusters created in our study. The grey colormap shows the topography; data from Tozer et al. (2019). The yellow lines are the country boundaries; data from ICPAC GEOPORTAL. (a) Global view over the African continent; (b) Enlarged view of central-southern African continent; (c) Enlarged view of southwestern Africa.

3.2 Kinematic Models

We use kinematic models to backtrack the kimberlite locations. Kinematic models are models that describe the present and past motion of the tectonic plates (Cox and Hart, 1986). The design of kinematic models relies on the integration of diverse geological and geophysical datasets, including seafloor spreading rates, and fracture zone azimuths, earthquake slip vectors, estimates of instantaneous tectonic plate velocities from global positioning system (GPS), hotspot tracks, paleomagnetic constraints, and plate boundaries (DeMets et al., 2010; Kreemer et al., 2014; Müller et al., 2019). For example, the Muller et al. (2019) reconstruction integrates geological and geophysical constraints, such as seismic reflection and refraction data, crustal thickness fluctuations, thermochronological data, and paleomagnetic measurements, and model the global plate motions for the last ~240 Myr. They used small, stiff blocks undergoing extension and compression to mimic lithospheric deformation. This method acknowledges the challenge of explicitly modeling ductile flow in plate reconstructions while capturing first-order deformation (Müller et al., 2019).

Young et al. (2019) developed a hybrid reconstruction that uses mantle, hotspot and paleomagnetic reference frames to model plate motions back to 410 Ma. Their model includes reference frames that change over time and considers how plate motion changes with Gondwana assembly and breakup.

Some kinematic models use the Plume Generation Zone (PGZ) method (e.g., Torsvik et al., 2014; Giuliani et al., 2021). The PGZ model posits that kimberlites, mantle plumes, and large igneous provinces (LIPs) tend to originate along the margins of LLSVPs. As a result, continental positions are reconstructed so that the locations of plumes, LIPs and kimberlites align with the margins of LLSVPs. As explained above, using models that assume a causality between LLSVPs,

and kimberlite locations would be circular reasoning for our study. Hence, kinematic models employing the PGZ approach are not adequate for testing the hypothesis that kimberlites originate along the margins of LLSVPs.

In this study, we consider the kinematic model designed by Merdith et al. (2021), which provides a continuous, consistent model extending back to 1 Ga. This model integrates paleomagnetic data with geological constraints such as rift systems, subduction zones, and arc terranes. Paleomagnetic data provide first-order constraints on continental latitudinal positions relative to Earth's spin axis, while geological data refine relative plate motions where available (Merdith et al., 2021). For older plate motions before the Mesozoic, where direct geological constraints are sparse, the reconstruction relies more heavily on paleomagnetic information, whereas, for Mesozoic and Cenozoic intervals, there is improved geological and geophysical coverage. The model is particularly well suited for long-term reconstructions of African plate motion and is, therefore, adopted as the principal framework for this study.

In addition, this study considers the recent global reconstruction model of Cao et al. (2024), which builds upon earlier plate kinematic frameworks while incorporating updated constraints on plate boundary evolution, paleomagnetic data, and absolute reference frames. The Cao et al. (2024) model emphasizes internal consistency between plate motions, plate boundary geometries, and mantle reference frames, and provides revised reconstructions of continental motion through the Neoproterozoic and Phanerozoic. By integrating updated geological interpretations and improved temporal resolution, this model offers an alternative perspective on long-term plate kinematics, particularly for Precambrian reconstructions. The model developed by Cao et al. (2024) provides the most recent and comprehensive reconstruction and permits analysis over an extended timescale of 1.8 Ga. It uses the model developed by Merdith et al. (2021) for the 1000-0 Ma period.

3.3 Plate Reconstructions Using GPlates and the GPlates Web Service (GWS)

At first, we modelled the plate reconstructions by using GPlates, an open-source software developed by the EarthByte Project for visualizing and reconstructing plate tectonic evolution through time (Boyden et al., 2011; Gurnis et al., 2012; Müller et al., 2018). GPlates enables interactive reconstruction of tectonic plates and geological features using predefined kinematic models and rotation hierarchies.

In GPlates, geological entities such as continental outlines, plate boundaries, hotspots, and magmatic occurrences are represented as geometric features including polygons, lines, and points. Each feature is assigned a unique plate identification number (plate ID) linking it to specific tectonic plates (Muller et al., 2018). The plate IDs are numbers that represent plates (Boyden et al., 2011). Plate geometries are stored in GPML or compressed GPMLZ formats, which allow complex spatial datasets to be efficiently managed and visualized.

GPlates incorporates the structure of the rotation hierarchy to link motions of each plate to another (Boyden et al., 2011). A rotation hierarchy is a tree-like structure used to model plate motions. One plate is fixed as a reference plate for other plates and at the top of the hierarchy structure. All other plates that are coded as sublevels to the higher plate have their rotation components altered when the rotation poles of the plates higher in the hierarchy are changed (Boyden et al., 2011). In this sense, the motions of the plates at the lower levels of the hierarchy are rooted in the plates at the higher levels. The larger plates typically occupy higher levels in the hierarchy, while smaller plates move relative to them. Rotation parameters governing plate motion are stored in rotation (ROT) files, which contain coordinates, ages, plate ID, rotation angles, and reference plate IDs (Müller et al., 2018). In GPlates, we use point features to denote locations of kimberlites on the African plate. The points are then digitized using the digitizing tool and assigned

to a plate ID 701, corresponding to the African plate ID. Since GPlates allows an anchored plate to be selected, we typically consider a fixed mantle (absolute) reference frame and select plate ID 0, which represents a mantle or hotspot-based reference frame. In other words, we try to assess the motions of the lithospheric plates in a fixed mantle frame.

The point features are created by setting the camera location on GPlates and inputting the coordinates (longitude and latitude) of the selected kimberlite. The age appearance corresponding to the emplacement age of the kimberlite is then assigned to the point. The reconstruction is done using an increment of 1 Myr by backtracking these point features from their present-day positions to their inferred locations at the time of emplacement using the selected kinematic models. In other words, we compute the location of the continental plate at the time the kimberlite was emplaced. Once the reconstruction positions are calculated, the plotted point feature is saved in a GPML file. GPlates enables the export of reconstructed geometries in standard geographic styles, including GMT-compatible XY files. These exported files contain reconstructed latitude and longitude coordinates of features at specified time intervals and can be used for further analysis outside GPlates. In this study, we integrate the reconstructed kimberlite positions with seismic tomography datasets for analysis using MATLAB (Matlab R2024a, Mathworks®).

In addition to the desktop application, this study makes use of the GPlates Web Service (GWS) to perform plate reconstructions programmatically. We contacted Xiaodong Qin (Michael Chin), a software engineer of the GPlates projects, who provided us with the HTTP for GWS. The GPlates Web Service provides online access to plate rotation models and reconstruction functionality, allowing users to submit reconstruction requests and retrieve reconstructed coordinates (longitude and latitude) without manual interaction with the graphical user interface. GWS applies the same finite rotation algorithms and rotation hierarchies used in the GPlates

desktop software, ensuring methodological consistency. The interaction with Xiaodong Qin allowed us to pinpoint a problem with the GPlates desktop software for ages older than 300 Ma. From that moment on, we have been using the GPlately software (Mather et al., 2023), described below.

3.4 GPlately

GPlately, a Python-based library for plate tectonic reconstructions, which is also part of the GPlates project, is used to complement the reconstructions performed using GPlates and the GPlates Web Service. GPlately applies the same finite rotation principles and rotation files used in GPlates, but enables automated, script-based reconstruction workflows that are reproducible and easily integrated with numerical analysis tools (Müller et al., 2018; Merdith et al., 2021). We use the GPlately filter coastlines command and the Merdith et al. (2021) kinematic model to extract just the blocks that make up the African continent. This is done by assigning individual plate IDs to different polygons of interest. This command automatically saves the extracted polygons in a GPMLZ file, which is used for further analysis in MATLAB. The backtracking results in this study have been obtained with GPlately. This software is based on the theory described above in section 3.3.

3.5 Seismic Tomography Models

Seismic tomography models provide the three-dimensional structures of Earth's interior in terms of seismic velocity variations. These velocity anomalies (*dvs* hereafter), commonly expressed as deviations from a reference Earth model (*dvs*), reflect variations in temperature or composition within the mantle. To investigate whether the kimberlite emplacement may be

correlated with LLSVPs, we compare the backtracked kimberlite positions with the present-day locations of LLSVPs derived from tomography models. In this study, we considered three independent global seismic tomography models: SPiRaL (Simmons et al., 2021), SAVANI (Auer et al., 2014), and TX2019slab (Lu et al., 2019) (Figure 3.2).

SAVANI (Auer et al., 2014) (Figure 3.2a) is a whole-mantle model of anisotropic shear-wave velocity variations constructed from the joint inversion of body wave travel times, surface wave phase anomalies, normal-mode splitting functions, and long-period waveforms. Unlike fixed-resolution global models, SAVANI uses a variable-resolution parameter in which block sizes are adapted to data sampling density, providing enhanced resolution in well-sampled regions while retaining global coverage from the upper mantle to the core–mantle boundary. A P- and S-wave joint tomography inversion was used to create TX2019slab (Figure 3.2b), which includes a three-dimensional thermal model of subducting slabs in the original model (Lu et al., 2019). SPiRaL (Simmons et al., 2021) (Figure 3.2c) is a global shear-wave velocity tomography model that resolves mantle structure from the upper mantle to the core–mantle boundary using a multi-scale inversion approach. The model integrates a range of seismic observations, including body waves and surface waves, to capture both large-scale and smaller-scale heterogeneities in mantle velocity structure. MATLAB (MathWorks®) is used to process and visualize tomography models.

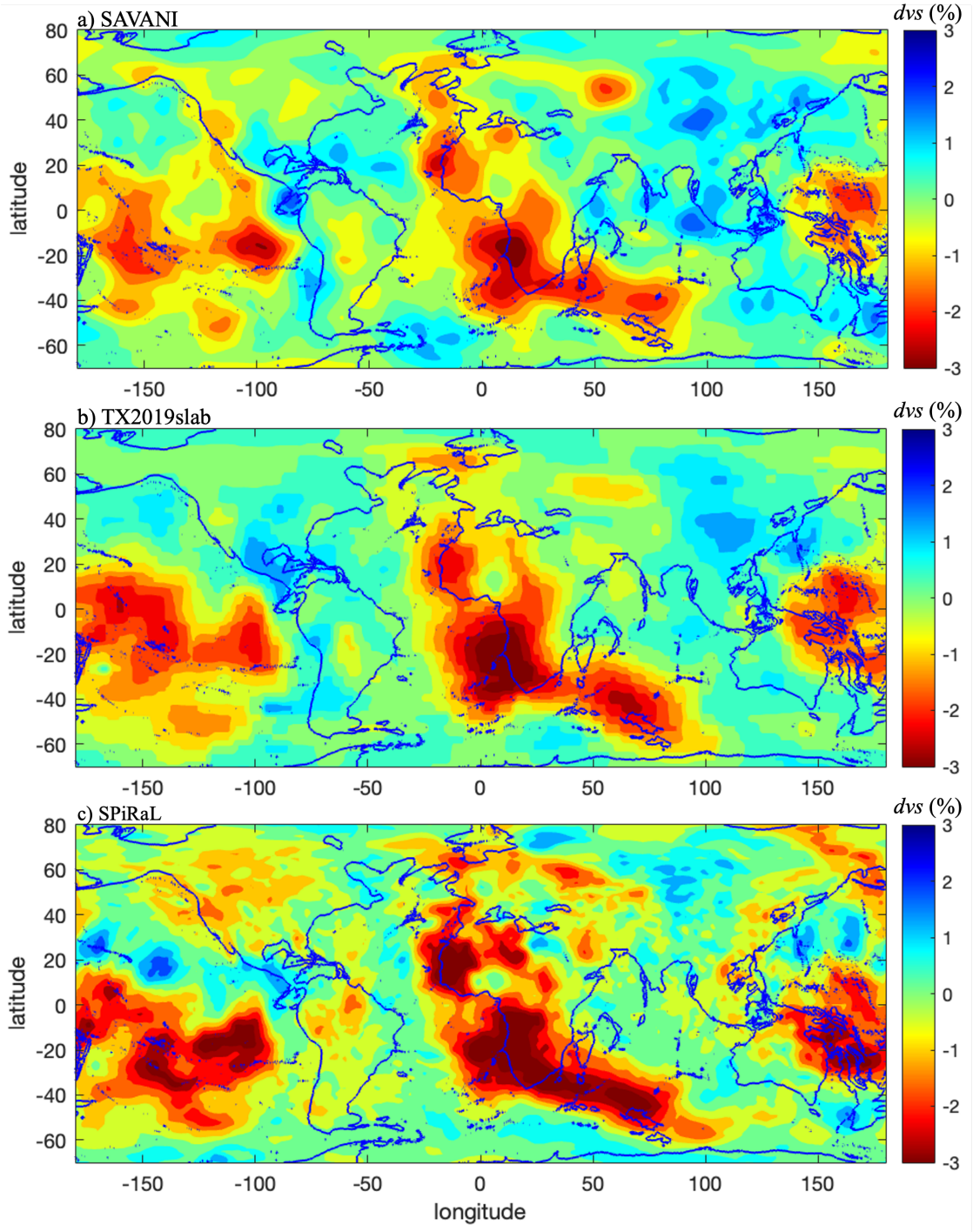


Figure 3.2: Seismic tomography models considered in this study. (a) SAVANI tomography model (Auer et al., 2014), (b) TX2019slab tomography model (Lu et al., 2019), and (c) SPiRaL tomography model (Simmons et al., 2021), at a depth of ~2800 km. The LLSVP locations are reported in red (region associated with negative seismic velocity anomalies, *dvs*). The blue line represents the 0 isobath; data from Tozer et al. (2019).

3.6 Lithosphere-asthenosphere boundary (LAB)

The lithosphere-asthenosphere boundary (LAB) models provide the thickness of the lithosphere, i.e., the depth of the boundary between the lithosphere and the asthenosphere. We use the Priestley et al. (2024) global lithospheric thickness model, CAM2022, for our study. We are also considering the gradient of the LAB, as previous studies pointed out that kimberlites may emplace along the boundary between thick and thin lithosphere or along the thinner plate near this boundary (King and Anderson, 1998; Adam and Kempton, 2025), as discussed in the EDC section (section 2.1.4). We visually compare the LAB and its gradient with the present-day locations of kimberlites. The CAM2022 model (Priestley et al., 2024) (Figure 3.3) is derived from a global inversion of surface wave data, incorporating a very large dataset of seismic observations to constrain shear-wave velocity structure in the upper mantle.

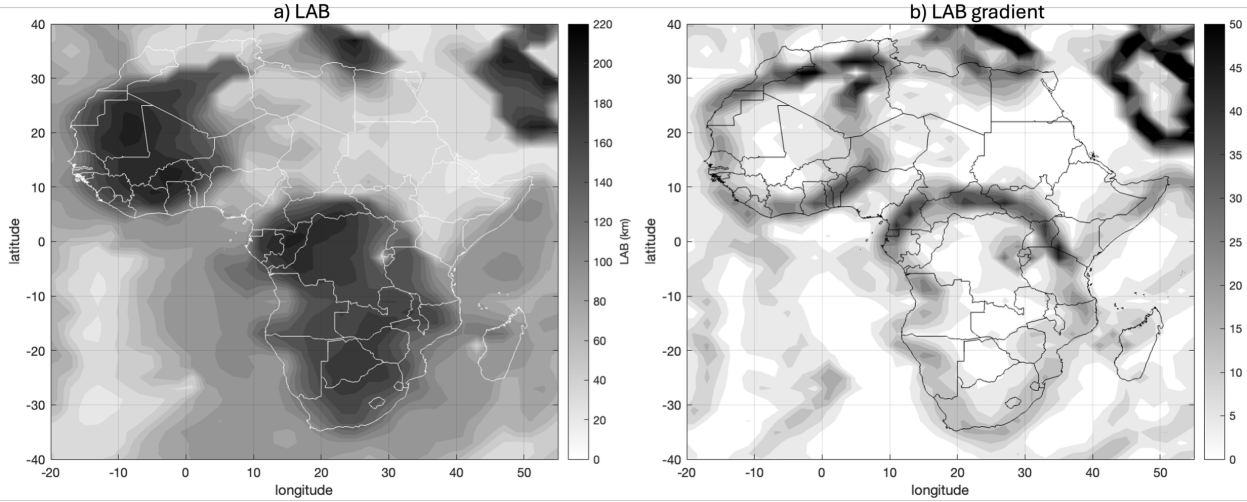


Figure 3.3: Lithosphere-Asthenosphere Boundary (LAB) and LAB gradient. LAB shown in panel (a) obtained using data from Priestley et al. (2024). Panel (b) shows the corresponding LAB gradient shown in panel. Country boundaries are shown as white lines in (a) and black lines in (b).

3.7 Method for Quantitative Assessment of Correlation Between Kimberlites and LLSVPs

To quantitatively assess the correlation between backtracked kimberlites positions and LLSVPs, we use the method developed by Adam and Kempton (2025). For each backtracked kimberlite position, we examine a circular area of radius R and identify the minimum seismic velocity anomaly near the core-mantle boundary from tomography models. If this minimum value of the seismic tomography model encountered within this circular area is below a threshold value dvs_{min} (dvs_{min} = -1%, for example), the backtracked position is located on an LLSVP according to that model. The key parameters of this method are the radius, R, the tomography model used, and the threshold dvs_{min}. Given that the latest tomography models have a default node spacing of approximately 2° in the lower mantle (Simmons et al., 2021), we adopt R = 2°. As LLSVP characteristics differ between tomography models, we use three of the most recent and advanced models; Savani (Auer et al., 2014), TX2019slab (Lu et al., 2019), and SPiRaL (Simmons et al., 2021). If a backtracked position meets the criterion (i.e., $dvs < dvs_{min}$ within the circular area of radius R) for at least two of the three considered tomography models, it is considered to be located on an LLSVP.

3.8 African Rifts Digitization

We also investigate the potential influence of rifts in the kimberlite emplacement by correlating the present-day kimberlite positions with rifts. Existing digital datasets for rift locations were not readily accessible, and efforts to obtain such data from published sources were unsuccessful. We also attempted to directly contact Celal Şengör, lead author of a published paper on rift geometries in Africa (Sengör and Natalin, 2000), but this was also unsuccessful. As a result,

we manually digitized the rift system using ArcGIS Pro (Esri, 2025). Rift geometries were interpreted and digitized from the published paper by Sengör and Natalin (2000) and subsequently stored as a shapefile. The resulting shapefile is then exported and processed in MATLAB for visualization and integration with our kimberlite dataset (Figure 3.4).

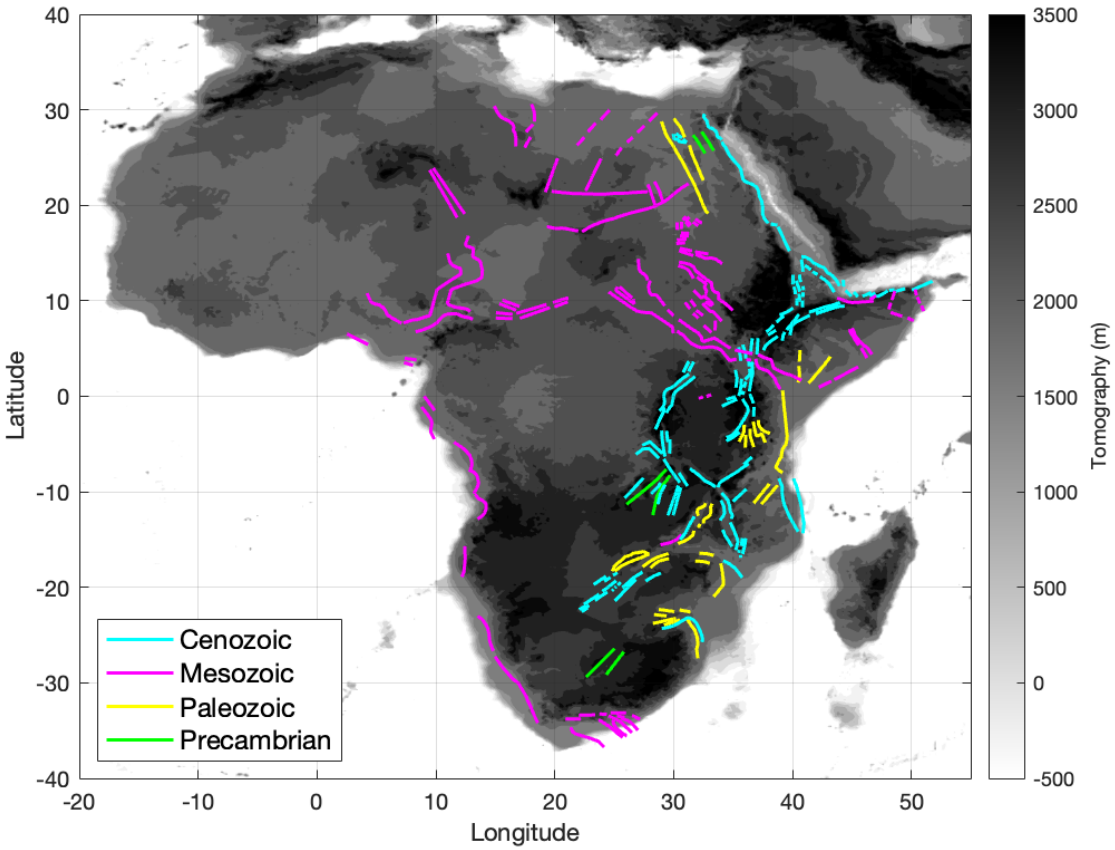


Figure 3.4: The African Rift System; data from Sengör and Natalin. (2000), showing digitized rifts colored by age. Precambrian age is reported in green, Paleozoic is reported in yellow, Mesozoic is reported in magenta, and Cenozoic is reported in cyan. The grey co colormap shows the topography; data from Tozer et al. (2019).

Chapter 4 - Results

In this chapter, we compare the present-day and backtracked locations of kimberlites with other geophysical and geological data, such as tomography models, the lithosphere-asthenosphere boundary, and rift locations. The ages and locations of the kimberlite dataset used in this study are shown in Figure 4.1. As discussed in Chapter 3, we use the database designed by Tappe et al. (2018). However, the data show that kimberlites tend to occur in clusters. Each cluster contains many kimberlite samples, occasionally exhibiting overlapping ages. To avoid redundancy, we define 75 geographical clusters and randomly assigned cluster numbers (Figure 4.1). Cluster design is detailed in Appendix 1. Results for the unclustered dataset are shown in Appendix 2.

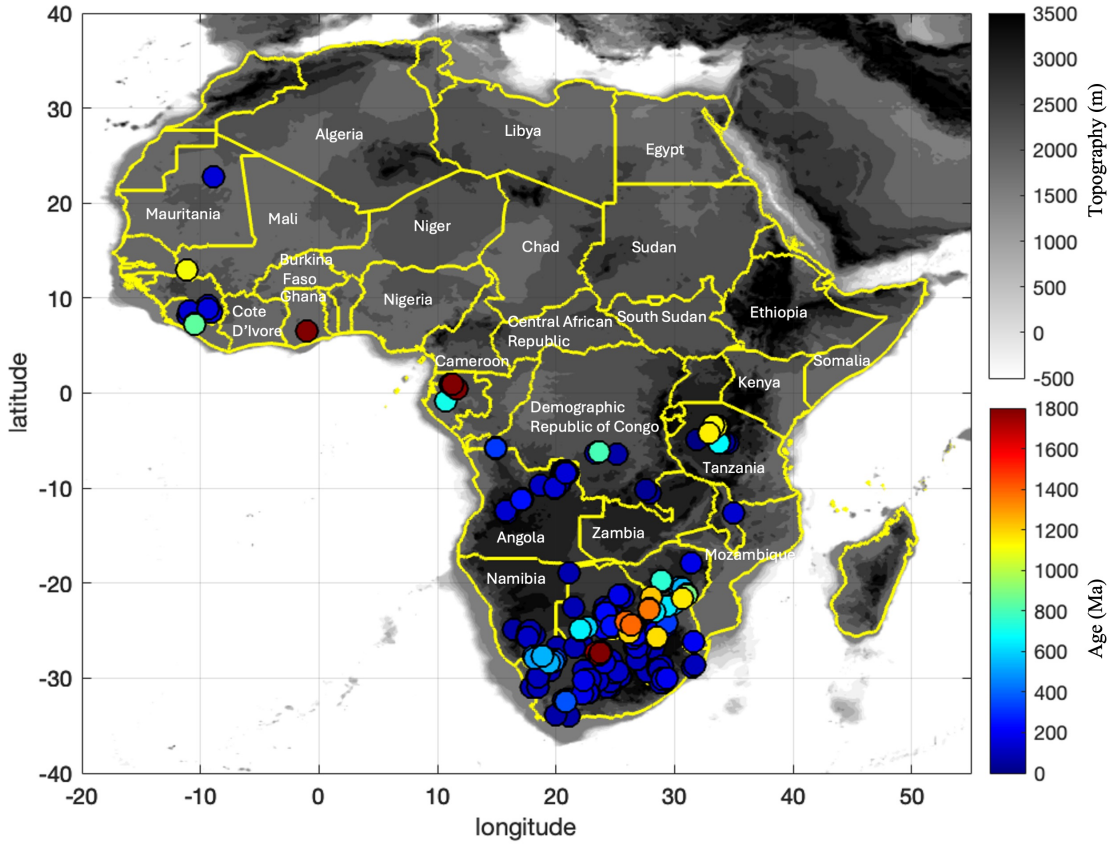


Figure 4.1: Kimberlite database for the African continent used in this study. The figure summarizes the defined clusters (see text). The colored circles display the ages and locations of kimberlites. The numbers are some of the cluster numbers created in our study. The grey colormap shows the topography; data from Tozer et al. (2019). The yellow lines are the country boundaries; data from ICPAC GEOPORTAL.

4.1 Correlation between backtracked kimberlite positions and present-day LLSVPs locations

Large low shear velocity provinces (LLSVPs) are regions associated with low seismic velocity, found at the base of the lower mantle, near the core-mantle boundary (Davies et al., 2015), as discussed in detail in chapter 2 (section 2.1.3). We investigate the relationship between the backtracked kimberlite locations and the locations of LLSVPs. The backtracked kimberlite locations are reconstructed to their paleogeographic position using the global plate motion model

developed by Merdith et al. (2021) and Cao et al. (2024). While several kinematic models are available, these two are among the most recent and widely used. Results presented in this study are primarily based on the Cao et al. (2024) kinematic model. The updated model of Cao et al. (2024) uses Merdith et al. (2021) for the 1,000-0 Ma period but extends further to 1,800 Ma, allowing for a more comprehensive assessment of long-term mantle-surface interaction. We employ three global seismic tomography models for the correlation: SPiRaL (Simmons et al., 2021), SAVANI (Auer et al., 2014), and TX2019slab (Lu et al., 2019) (Figure 4.2). As described in section 3.7, for each backtracked kimberlite location, we define a circular search region of radius R. Within this region, we identify the minimum seismic velocity anomaly from tomography models at a depth of approximately 2,800 km, corresponding to the core–mantle boundary. If this minimum value is lower than a threshold value (dvs_{min}), the backtracked kimberlite is located on an LLSVP according to that model. This procedure is repeated for all three tomography models considered in this study. A backtracked kimberlite location is ultimately said to be located on an LLSVP if this criterion is satisfied for at least two of the three considered models. In this section, we test the influence of the method parameters and display our results.

4.1.1 Influence of the tomography models used to assess the correlation between backtracked kimberlites and LLSVPs

The characteristics of LLSVPs vary based on the considered tomography models. The tomography models shown in Figure 4.2 are some of the newest and most extensively utilized, cutting-edge tomography models: SPiRaL (Simmons et al., 2021), TX2019slab (Lu et al., 2019), and SAVANI (Auer et al., 2014). We can observe that the newer tomography model, the broader the LLSVPs, and the higher the amplitude of the seismic velocity anomaly, dvs, associated with

the LLSVPs. The newer tomography models should, in theory, give a more realistic picture of the structure of the mantle in general, and the structure of the LLSVPs in particular. Consequently, it seems more appropriate to examine the newest tomography models in our study.

Indeed, the characteristics of the LLSVPs change (differ from one tomography model to another); hence, we perform our analysis using three independent tomography models. However, there are also some similarities, and most of our backtracked kimberlites for the 260-0 Ma period seem to be located over LLSVPs or at least on their margins (Figure 4.2).

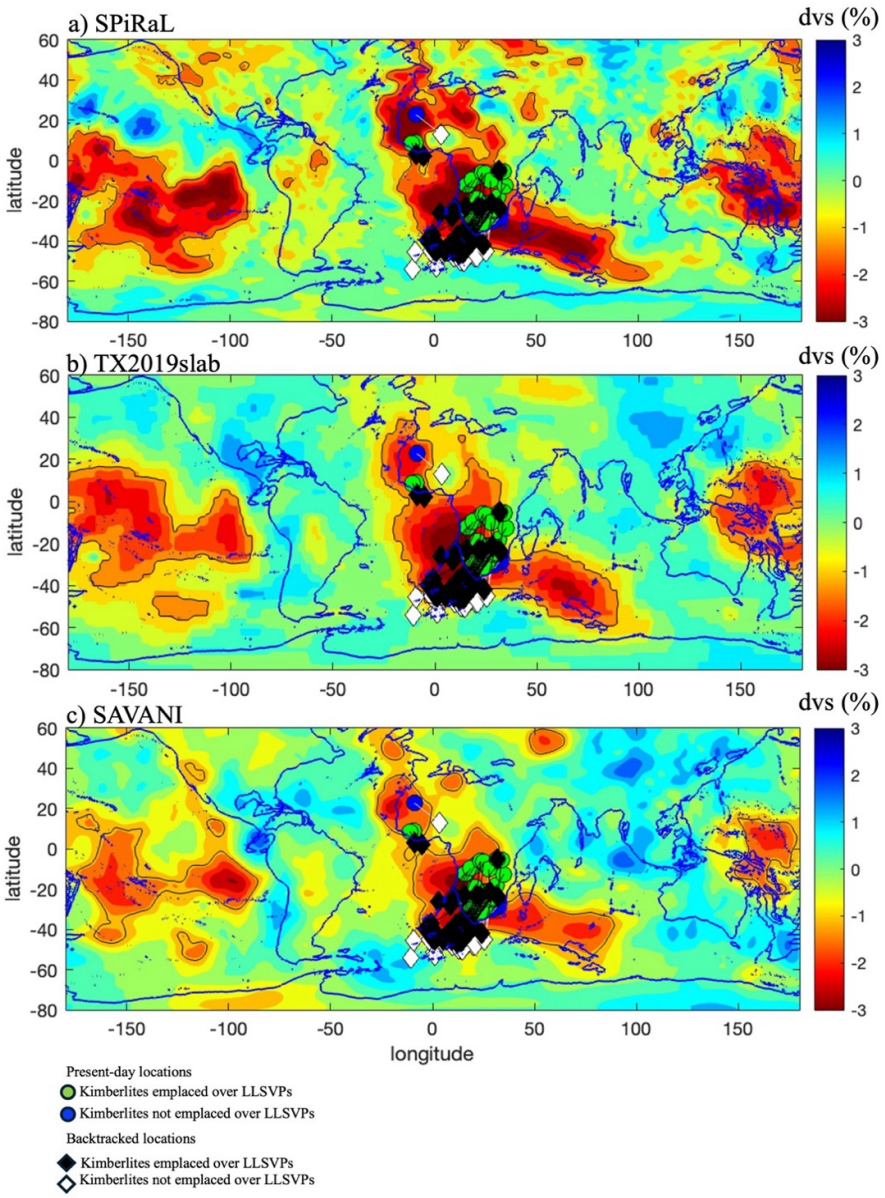


Figure 4.2: Correlation between LLSVPs and backtracked kimberlite positions. The colormap shows the seismic velocity anomaly, *dvs*, near the core-mantle boundary extracted from three different global tomography models: SPiRaL (Simmons et al., 2021), TX2019slab (Lu et al., 2019), and SAVANI (Auer et al., 2014) as shown in panels a-c. The LLSVP locations, that is, regions associated with negative seismic velocity anomalies, *dvs* are shown in red. The *dvs* = −1% isocontour is reported in black. Isobath 0 is reported in blue. The present-day and backtracked locations of kimberlites emplaced over LLSVPs are displayed by green circles and black diamonds, respectively, while the present-day and backtracked locations of kimberlites not emplaced over LLSVP are displayed in blue circles and white diamonds, respectively.

4.1.2 Periods defined by looking at the correlation between backtracked kimberlites positions and LLSVPs

We identified distinct periods for which the backtracked kimberlite locations display different patterns:1800-1680 Ma, 1680-1620 Ma, 1620-1160 Ma, 1160-1110 Ma, 1110-590 Ma, 590-490 Ma, 490-260 Ma, and 260-0 Ma. In Figure 4.3, we show the backtracked and present-day kimberlite positions for the different periods superposed on the TX2019slab tomography model.

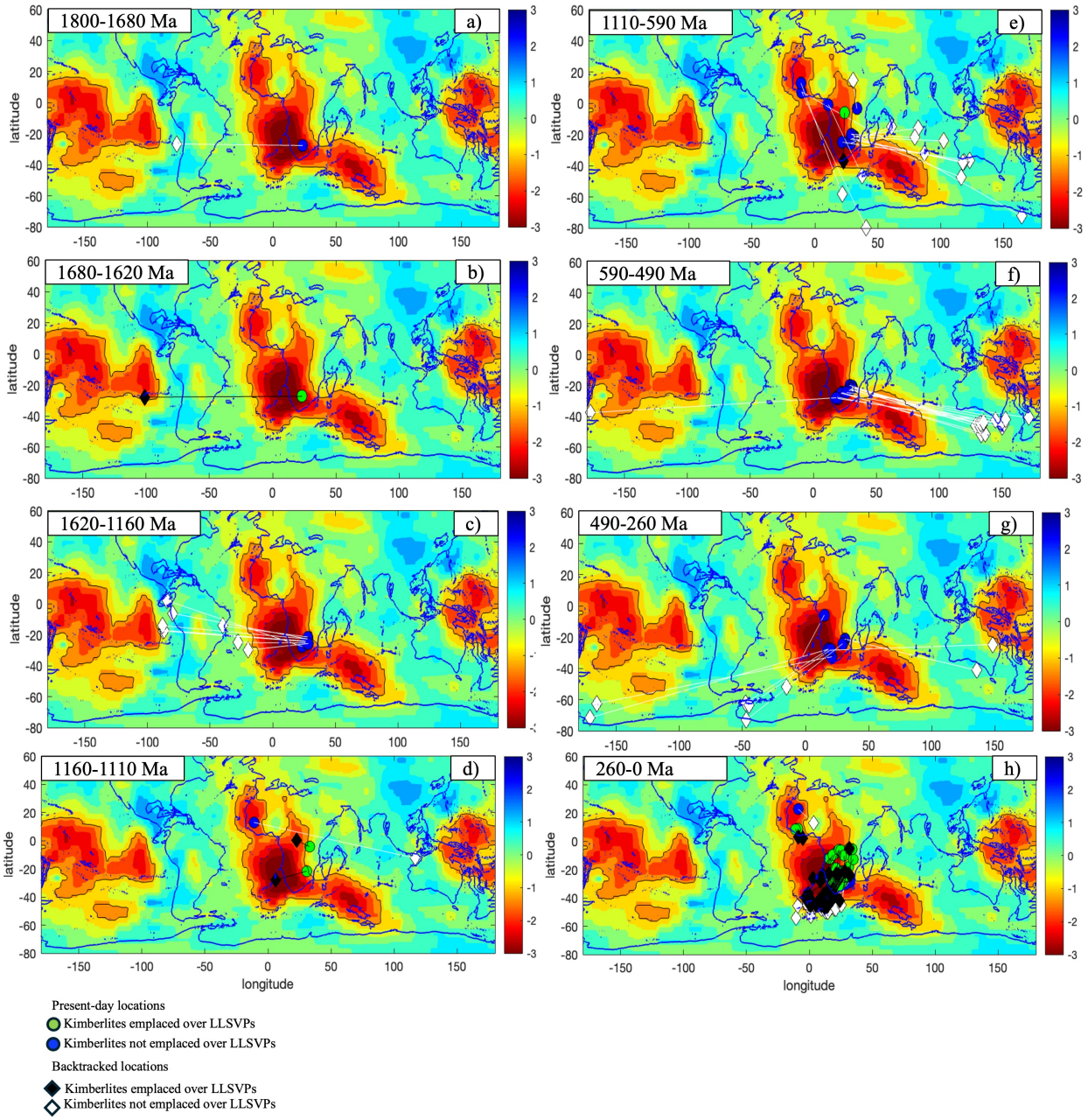


Figure 4.3: Correlation between LLSVPs and backtracked kimberlite positions. The colormap shows the seismic velocity anomaly, dvs, near the core-mantle boundary provided by the TX2019slab tomography model (Lu et al., 2019). The LLSVP locations, that is, regions associated with negative seismic velocity anomalies, *dvs* are shown in red. The dvs = − 1% isocontour is reported in black. Isobath 0 is reported in blue. The present-day and backtracked locations of kimberlites emplaced over LLSVPs are displayed in green circles and black diamonds, respectively, while the present-day and backtracked locations of kimberlites not emplaced over LLSVP are displayed in blue circles and white diamonds, respectively. Panels (a-h) show the reconstruction for different time periods.

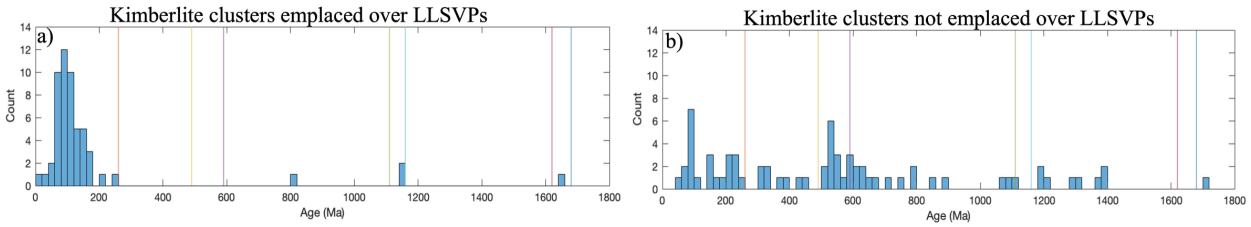


Figure 4.4: Quantitative correlation between backtracked kimberlites positions and LLSVPs as a function of the kimberlites' age. The kimberlites clusters emplaced over LLSVPs are reported in panel a, whereas the ones not emplaced over LLSVPs are displayed in panel b. The correlation is based on three tomography models. The color lines represent 260, 490, 590, 1100, 1160, 1620, 1680, and 1800 Ma ages discussed in the text.

By looking at the distribution of kimberlites emplaced or not emplaced over LLSVPs (Figures 4.3 and 4.4), we define several periods: 1800-1680 Ma, 1680-1620 Ma, 1620-1160 Ma, 1160-1110 Ma, 1110-590 Ma, 590-490 Ma, 490-260 Ma, and 260-0 Ma (vertical colored lines in Figure 4.4). As most of the kimberlites have ages between 0 and 260 Ma (74 out of 125 kimberlites clusters, 59.2%), we can thoroughly only define two periods: 260-0 Ma and 1,800-260 Ma. For the 260-0 Ma period, most of the kimberlites are obviously emplaced over LLSVPs (Figure 4.4a). In the 1,800-260 Ma period, there is a succession of periods of kimberlites mainly emplaced over LLSVPs, followed by periods of kimberlites mainly not emplaced over LLSVPS. However, as there are many fewer kimberlites older than 260 Ma, it is difficult to define statistically significant periods. However, the patterns defined previously (1800-1680 Ma, 1680-1620 Ma, 1620-1160 Ma, 1160-1110 Ma, 1110-590 Ma, 590-490 Ma, 490-260 Ma) are still interesting to discuss.

4.1.3 Influence of the threshold value, *dvs,* used to assess the correlation between backtracked kimberlites and LLSVPs

The precise boundaries and areal extent of an LLSVP is subjective. There is no clearly defined threshold value, $dvs_{min,}$ that definitively delineates the extent of the LLSVP. As a result, the choice of a single threshold value may introduce bias in identifying whether a backtracked kimberlite location is associated with an LLSVP or its margins. To address this uncertainty, we test the influence of varying the model parameter, including the dvs_{min}. We systematically test a range of threshold values, $dvs_{min,}$ and evaluate the resulting correlations between backtracked kimberlite position and LLSVP locations. In Figure 4.5, we display the correlation between backtracked kimberlite positions and LLSVPs for three different threshold values (*dvs* = -1%, *dvs* = -0.5%, and *dvs* =-0.1%). For kimberlites emplaced over LLSVPs (Figures 4a, c, e), varying the threshold value (*dvs*) has no significant influence on the results. The distribution of kimberlites emplaced over LLSVPs is similar for the considered dvs_{min} values. However, if we look at the kimberlites not emplaced over LLSVPs for the 260-0 Ma period, we can see that diminishing the absolute value of dvs_{min} diminishes the number of kimberlites not emplaced over LLSVPs (Figure 4.5b, d, f). This means that some of the kimberlites assessed as "not emplaced over LLSVPs" with dvs_{min} = -1%, are emplaced over LLSVPs as we assume dvs_{min} = -0.1% (Figure 4.5a and e). In other words, these kimberlites could have been formed over the margins of the LLSVPs. In the following discussion, we will assume dvs_{min} = -1%, as this value has been used by Adam and Kempton (2025), but our main conclusion from the analysis above is that most of the African kimberlites younger than 260 Ma were emplaced over LLSVPs or their margins.

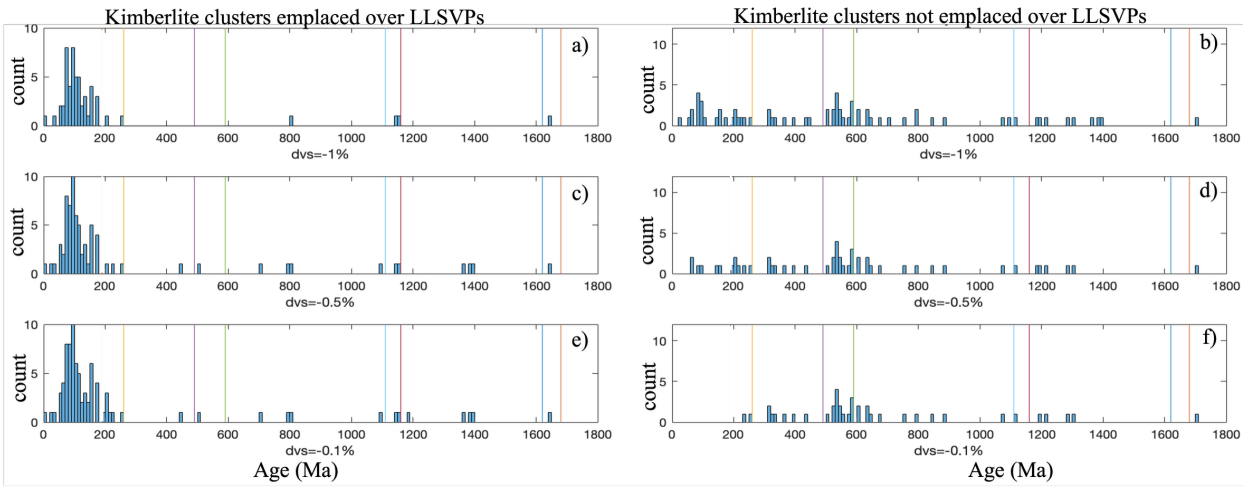


Figure 4.5: Influence of varying threshold value, dvs_{min}, on the correlation between backtracked kimberlites and LLSVPs. The kimberlites clusters emplaced over LLSVPs are reported in panels a, c, and e, while those not emplaced over LLSVPs are displayed in panels b, d, and f. The correlation is based on three tomography models. The color lines represent 260, 490, 590, 1110, 1160, 1620, 1680, and 1800 Ma.

4.2 Correlations between present-day kimberlite locations and the lithosphere-asthenosphere boundary

As discussed in Chapter 2, according to some authors, edge-driven convection (EDC), induced from the transition from thick lithosphere to thin lithosphere (King and Anderson, 1998), may be associated with the emplacement of kimberlites (Kjaarsgard et al., 2017; Kempton et al., 2019). In this study, we investigate the relationship between the lithosphere-asthenosphere boundary (LAB) and the present-day kimberlite locations. We considered the global lithospheric thickness model (CAM2022) by Priestley et al. (2024) for this study. The CAM2022 model is based on a global inversion of surface wave data, incorporating a very large dataset of seismic observations to constrain shear-wave velocity structure in the upper mantle. This model captures the large-scale, long-wavelength structure of lithospheric thickness globally. We examine the correlation between

kimberlites and the LAB horizontal gradient, as some studies report that kimberlites will emplace mainly along the thinner lithosphere adjacent to the transition (King and Anderson, 1998; Tappe et al., 2014; Kempton et al., 2019). In Figure 4.6, we report the present-day lithospheric thickness (or LAB), its horizontal gradient, and the ages and locations of kimberlites, based on the database developed for this study (see text and Appendix 1). There is no clear correlation between the kimberlite locations and the LAB or its gradient.

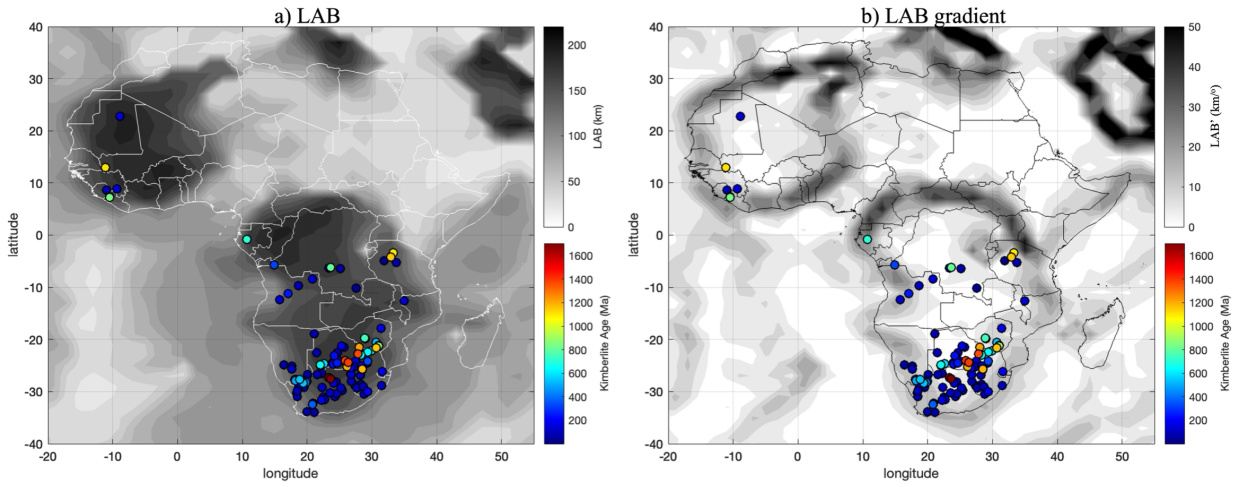


Figure 4.6: Lithosphere-Asthenosphere Boundary (LAB), LAB horizontal gradient, and kimberlite distributions. The colored circles display the ages and locations of kimberlites according to the database developed for this study (see text). The LAB shown in panel (a) is obtained using the data from Priestley et al. (2024). Panel (b) shows the LAB horizontal gradient. Country boundaries are shown as white lines in (a) and black lines in (b).

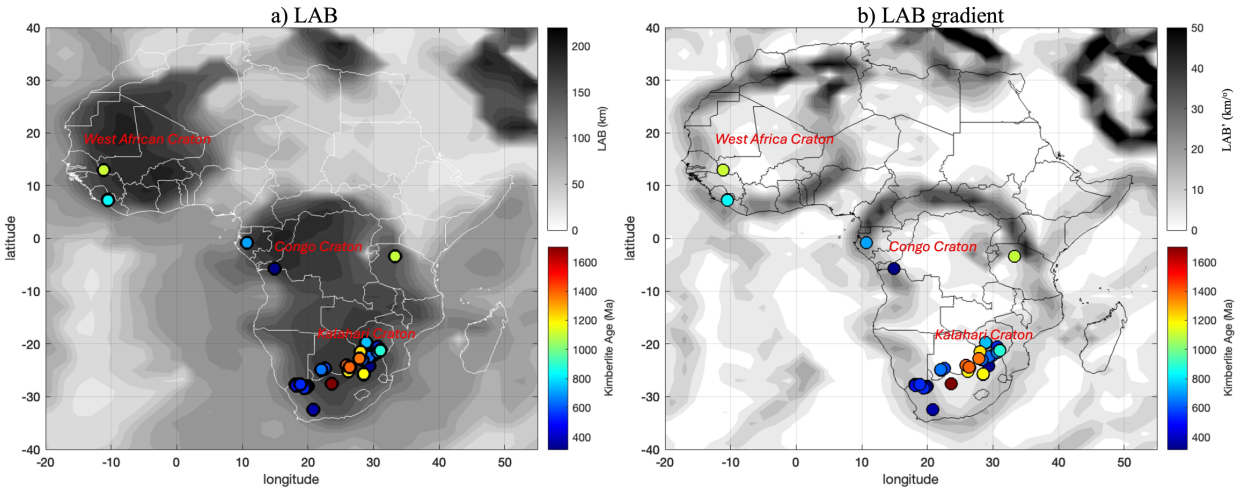


Figure 4.7: Lithosphere-Asthenosphere Boundary (LAB), LAB horizontal gradient, and distribution of kimberlites with ages between 1800 and 260 Ma. Major cratonic regions: West African craton, Congo craton, and Kalahari craton are indicated for reference. The color circles display the ages and locations of kimberlites according to the database developed for this study (see text). The LAB shown in panel (a) is obtained using the data from Priestley et al. (2024). Panel (b) shows the LAB horizontal gradient. Country boundaries are shown as white lines in (a) and black lines in (b).

However, most kimberlites with ages between 1800 and 260 Ma show a consistent spatial pattern (Figure 4.7), with many occurrences located above the regions with high LAB gradients (grey regions Figure 4.7b), particularly near the margins of the West African, Congo, and Kalahari cratons.

4.3 Correlation between present-day kimberlite locations and rifts

Rifting has long been proposed as a structural control on kimberlite emplacement, as rift systems create zones of lithospheric weakness that can facilitate the ascent of volatile-rich melts from depth (e.g., Jelsma et al., 2009; Tappe et al., 2018; Gernon et al., 2023).To investigate the potential relationship between kimberlite emplacement and lithospheric extension, we compare the present-day locations of kimberlite clusters with the distribution of African rift systems. Rift geometries were digitized from a published paper by Sengör and Natalin (2000) (section 3.8) and represent major rifting episodes across the continent. By examining the spatial correspondence

between kimberlites and rifts, we assess whether kimberlite occurrences are preferentially associated with zones of lithospheric weakening and extension.

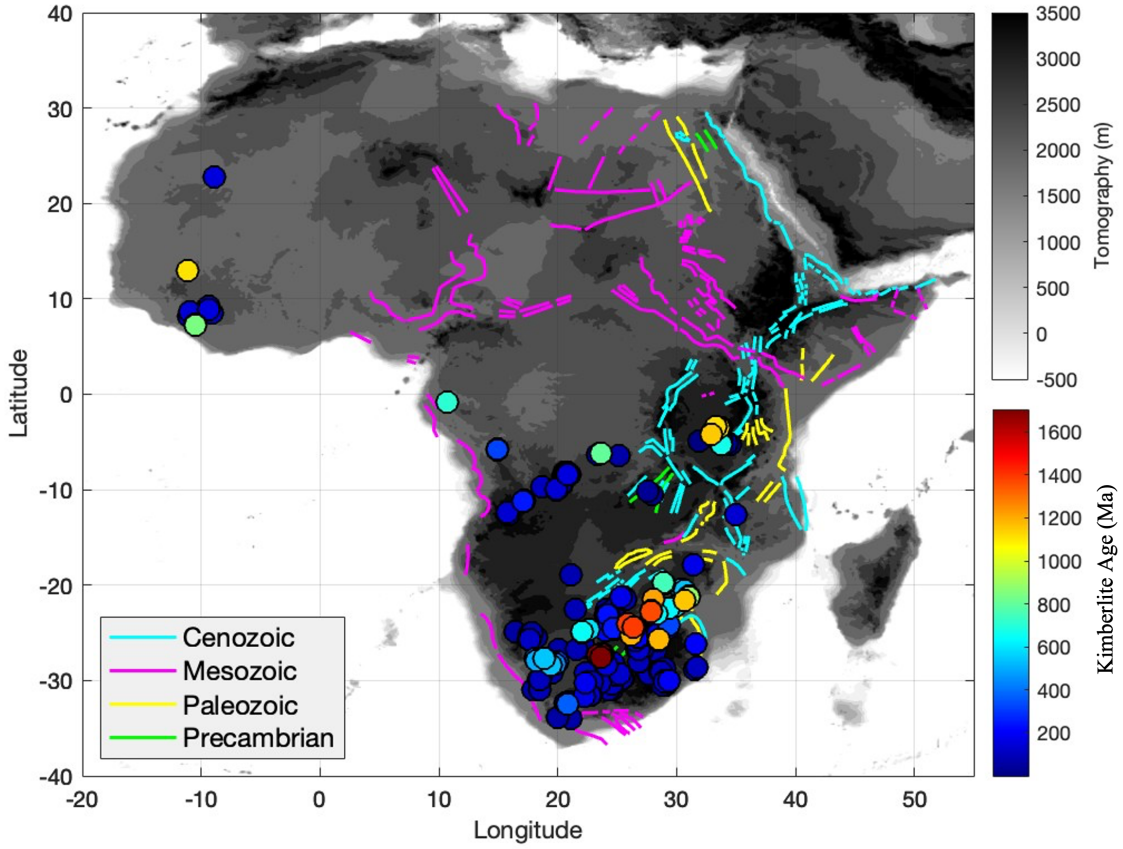


Figure 4.8: The African Rift System; data from Sengör and Natalin (2000), showing digitized rifts colored by age and the ages and locations of kimberlite clusters. Precambrian age is reported in green, Paleozoic is reported in yellow, Mesozoic is reported in magenta, and Cenozoic is reported in cyan. The grey colormap shows the topography; data from Tozer et al. (2019).

Figure 4.8 shows that kimberlites have been emplaced in the northwestern part of Africa (Mauritania, Mali, and Guinea), but there are no rifts in this region. Conversely, in northern and eastern Africa, which hosts the prominent East African Rift System, kimberlite occurrence is sparse. In southern Africa, both kimberlites and rifts are common, which makes it more complex to establish cause-and-effect relationships, but in general, our assessment of the distribution is that

there is no clear spatial correlation between kimberlites and rift systems across the African continent.

Chapter 5 - Discussion

In this study, we try to bring new constraints to bear on the origin and emplacement of kimberlites. In particular, we investigate the relationship between backtracked kimberlite positions and present-day locations of large low shear velocity provinces (LLSVPs), constrained by seismic tomography models. Our aim is to assess whether kimberlites are preferentially emplaced over these LLSVPs or not. In addition, we investigate the influence of lithospheric controls, including edge-driven convection (EDC) linked to variations in lithosphere–asthenosphere boundary (LAB) structure, as well as the role of rifting, in controlling kimberlite emplacement. In this chapter, we discuss and interpret our results in the context of existing hypotheses, assessing the mechanisms of kimberlite emplacement and identifying the limitations that constrain these interpretations.

5.1 The spatio-temporal distribution of backtracked kimberlite locations and LLSVPs

One of the main aims of this study is to investigate the relationship between backtracked kimberlite positions and LLSVP locations. The LLSVPs are regions of the mantle associated with slower seismic velocities (Davies et al., 2015; McNamara, 2019; Davaille and Romanowicz, 2020). The lateral and vertical extent of the LLSVPs is in the order of thousands and hundreds of kilometers, respectively (McNamara, 2019, and references therein). The position and extent of the LLSVPs are generally constrained from tomography models (Torsvik et al., 2014; McNamara, 2019; Giuliani et al., 2020). Seismic tomography models show two broad LLSVPs, the Pacific LLSVP and the African LLSVP. These tomography models may differ from one another, as they are derived from different datasets using different inversion models.

In this study, we consider three most recent and widely used tomography models: the SPiRAL developed by Simmon et al. (2021), the SAVANI model, developed by Auer et al. (2014), and the TX2019slab model developed by Lu et al. (2019). As mentioned in section 4.1, we identified different time periods for which the backtracked kimberlite locations display different patterns: 260-0 Ma, 490-260 Ma, 590-490 Ma, 1110-590 Ma, 1160-1110 Ma, 1620-1160 Ma, 1680-1620 Ma, and 1800-1680 Ma. In Figure 5.1, we display the mantle structure near the CMB according to the TX2019slab tomography model and provide a visual comparison between LLSVPs and backtracked kimberlites locations.

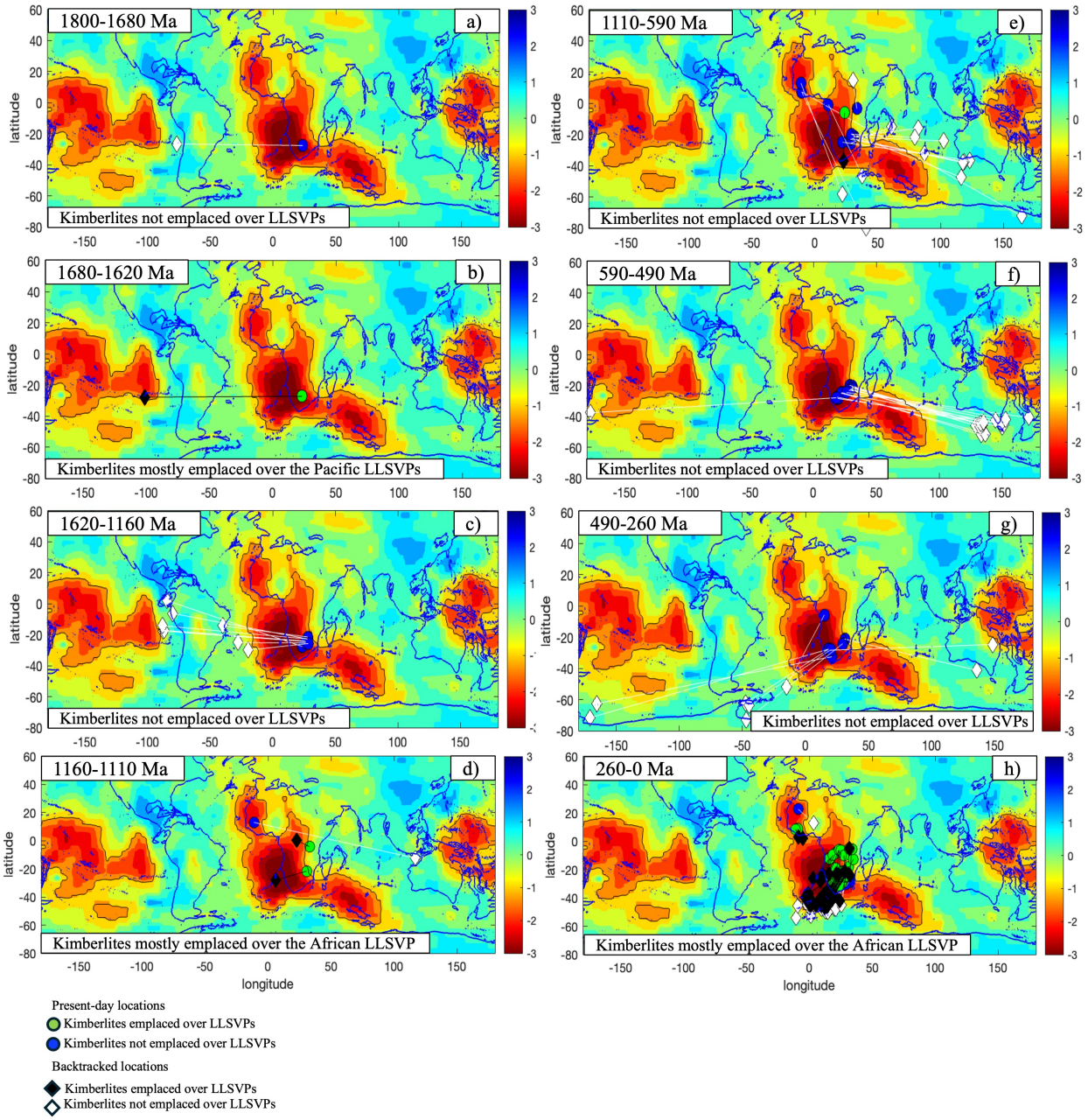


Figure 5.1: Correlation between LLSVPs and backtracked kimberlite positions. The colormap shows the seismic velocity anomaly, *dvs*, near the core-mantle boundary. The data are extracted from the TX2019slab tomography model (Lu et al. 2019). The LLSVP locations, that is, regions associated with negative seismic velocity anomalies, *dvs* are shown in red. The *dvs* = −1% isocontour is reported in black. Isobath 0 is reported in blue. The present-day and backtracked locations of kimberlites emplaced over LLSVPs are displayed by green circles and black diamonds, respectively, while the present-day and backtracked locations of kimberlites not emplaced over LLSVP are displayed in blue circles and white diamonds, respectively. Panels (a-h) show the reconstruction for different periods.

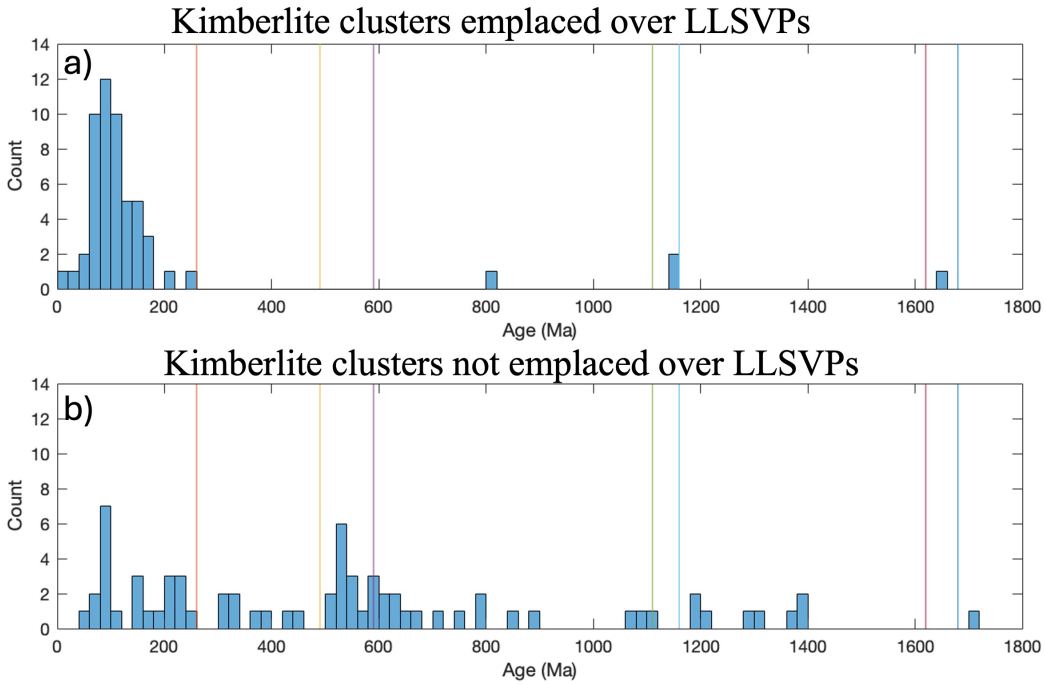


Figure 5.2: Quantitative correlation between backtracked kimberlites positions and LLSVPs as a function of the kimberlites' age. The kimberlites clusters emplaced over LLSVPs are reported in panel a, while the ones not emplaced over LLSVPs are displayed in panel b. The correlation is based on three tomography models. The color lines represent the 260, 490, 590, 1110, 1160, 1620, 1680, and 1800 Ma, respectively.

When we compare the backtracked kimberlite locations to the locations of the LLSVPs (Figures 5.1 and 5.2), we see a striking correlation in most cases. In particular, younger kimberlites show a stronger association with LLSVP regions and their margins, but this relationship is more variable for kimberlites from older intervals.

During the 1800-1680 Ma interval, the single kimberlite cluster backtracked in the southern hemisphere, is near to, but not on the eastern margin of the Pacific LLSVP (Figure 5.1a). The limited number of data points in this window prevents robust statistical inference. Conversely, the kimberlite clusters with ages between 1680 and 1620 Ma were emplaced along the margins of the Pacific LLSVPs (Figure 5.1b). A different pattern is observed for periods 1160-1110 Ma, where most of the kimberlites are emplaced over or along the margins of the African LLSVPs (Figure

5.1d). For 1110-590 Ma, most of the backtracked kimberlites are away from LLSVPs (Figure 5.1e).

Kimberlites with ages between 590 and 490 Ma backtrack to locations that do not overlie an LLSVP (Figure 5.1f). An intriguing pattern for this age group, however, is that their present-day location seems to be along a NE-SW alignment. For kimberlites with ages between 490 and 260 Ma, the backtracked kimberlites are also away from LLSVPs. In the youngest interval (260-0 Ma) (Figure 5.1h), backtracked kimberlites locations exhibit a strong correlation with the African LLSVPs, as discussed in Chapter 4 (section 4.1.2). However, the kimberlite located in Mauritania (Northwest of the African LLSVP) appears to be backtracked to a region that does not coincide with the core of the LLSVP. This observation may suggest that the LLSVP in this location may have been depleted by the extraction of other kimberlites. These younger kimberlites (i.e., younger than 260 Ma) make up ~56.2% of the African kimberlite clusters (Figure 5.2), indicating a strong temporal kimberlitic activity in this period, unlike in older periods, where few kimberlites were emplaced. As shown in Figure 5.2, this observation is consistent with previous studies showing that kimberlites are rare in the first half of Earth history, with ~85% of known kimberlites being Phanerozoic (<542 Ma) and more than 50% of dated kimberlites being Mesozoic in age (250–66 Ma) (Kjarsgaard et al., 2022).

These visually observed spatial patterns (Figure 5.1) are supported by the quantitative results (Figure 5.2 and Table 5.1). Overall, approximately 44% of kimberlite clusters are emplaced over LLVPs, whereas 56% do not show this association. However, this relationship varies significantly through time. The youngest interval (260-0 Ma) shows a relatively strong correlation, which is consistent with what we observed in Figure 5.1. With a dvs_{min} of -1%, 68.9% of kimberlites are emplaced over LLSVPs, while with a dvs_{min} of -0.1%, 100% of kimberlites are

emplaced over LLSVPs. In other words, most of the kimberlites younger than 260 Ma are emplaced over the African LLSVP or its margins.

There are relatively few kimberlites emplaced within the 1,800-260 Myr period, so it is difficult to define statistically significant periods. We can thoroughly only define two periods: 260-0 Ma (kimberlites emplaced mainly over the African LLSVPs) and 1,800-260 Ma (no clear pattern). The present-day and backtracked positions of kimberlites for these two periods are displayed in Figure 5.3, where we visually compare them with a tomography model.

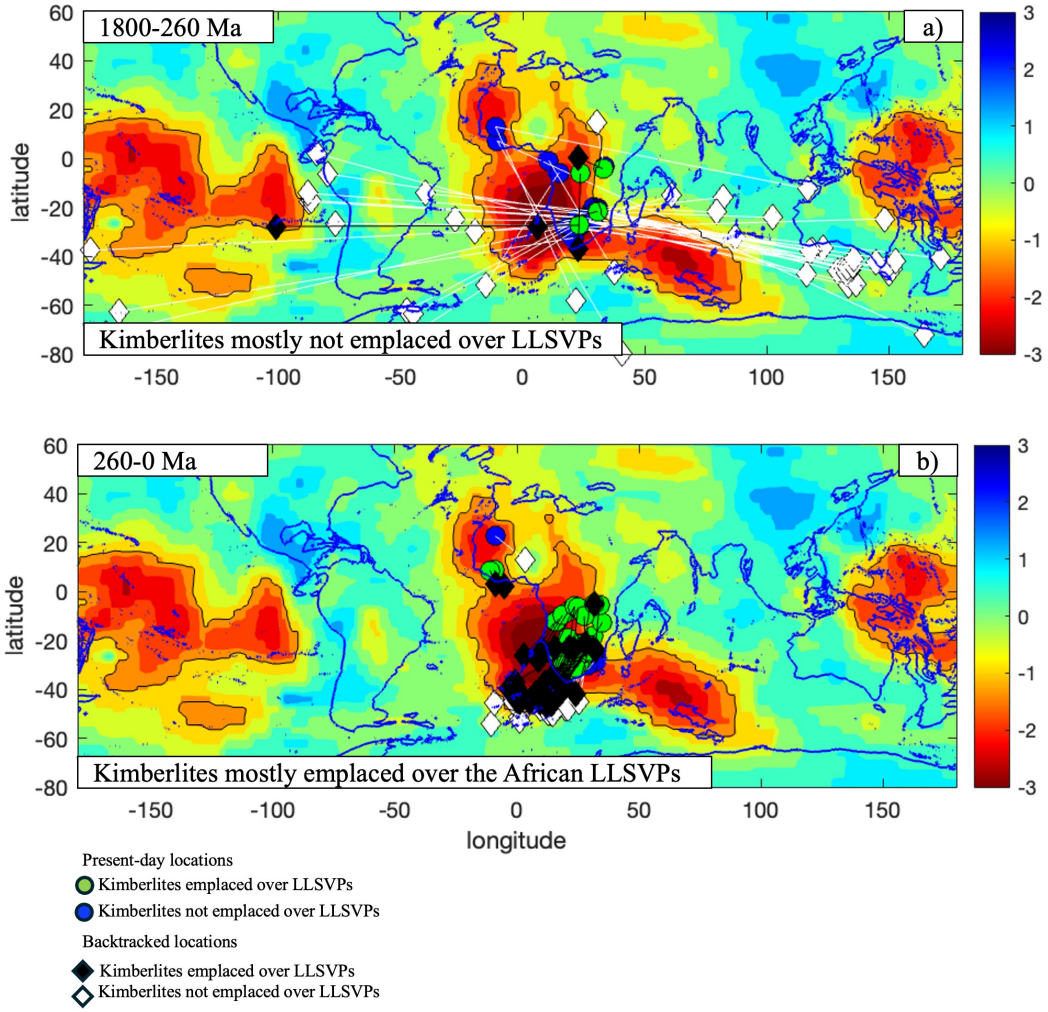


Figure 5.3: Correlation between LLSVPs and backtracked kimberlite positions. The colormap shows the seismic velocity anomaly, dvs, near the core-mantle boundary. The data are extracted from the TX2019slab tomography model (Lu et al. 2019). The LLSVP locations, that is, regions associated with negative seismic velocity anomalies, *dvs* are reported in red. The *dvs* = −1% isocontour is reported in black. Isobath 0 is reported in blue. The present-day and backtracked locations of kimberlites emplaced over LLSVPs are displayed by green circles and black diamonds, respectively, while the present-day and backtracked locations of kimberlites not emplaced over LLSVP are displayed in blue circles and white diamonds, respectively. Panels a and b show the reconstruction for different time periods.

Table 5.1: Summary of the correlation between backtracked kimberlite positions and LLSVPs

Periods (Ma)	Number of kimberlites clusters	Number of kimberlites emplaced over LLSVPs	Percentage of kimberlites emplaced over LLSVPs	Number of kimberlites not emplaced over LLSVPs	Percentage of kimberlites not emplaced over LLSVPs
1800-260	51	4	7.8%	47	92.1%
260-0	74	51	68.9%	23	31.1%

Previous studies have already proposed that kimberlite emplacement is or can be connected to the positions of LLSVPs (e.g., Torsvik et al., 2014; Giuliani et al., 2020; Adam and Kempton, 2025). However, there is no consensus on the origin of LLSVPs. They are often thought to be large-scale heterogeneities at the bottom of the lower mantle, and they are separated from each other by fast velocity regions. For some authors, they are described as large thermochemical structures at the base of the mantle (Davies et al., 2015; Mulyukova et al., 2015; Kreielkamp et al., 2022). LLSVPs are thought to be stable and long-standing structures by some authors (Torsvik et al., 2010; Mulyukova et al., 2015). According to several authors, various scales of mantle plumes may be derived from the LLSVPs (Kellogg et al., 1999; Davaille, 1999; Courtillot et al., 2003; Dziewonski et al., 2010; Torsvik et al., 2014). This hypothesis is supported by the observation that many hotspot tracks are located above LLSVP regions (e.g., Davies et al., 2015; Torsvik et al., 2016). Present-day LLSVPs are primarily located beneath the African and Pacific regions, commonly referred to as the African and Pacific LLSVPs. Although the African LLSVP is centered beneath the African continent, low seismic velocity anomalies extend into the northern Atlantic region (e.g., Torsvik et al., 2014; Giuliani et al., 2020).

LLSVPs may represent long-term accumulation zones for subducted oceanic crust. Subducted oceanic crust, which is depleted in incompatible elements relative to ocean island basalts, may be stored in the deep mantle over geological timescales (e.g., Hofmann 1988; Niu and O'Hara, 2003; Tolstikhin and Hofmann, 2005; Tolstikhin et al., 2006; Li, 2021). Niu (2018) argued that LLSVPs have remained structurally stable over the past ~300 Myr, partly because most subducted oceanic crust predates this interval and has already accumulated in the deep mantle. More recent studies have explored the relationship between kimberlite emplacement and LLSVPs, considering both fixed and mobile LLSVP scenarios (e.g., Flament et al., 2022; Grabreck et al., 2022; Bodur and Flament, 2023). These studies often model LLSVPs as thermochemical structures that are hotter than the surrounding mantle and capable of evolving spatially. Within this framework, reconstructed mantle flow over the past billion years can account for the observed distribution of kimberlite eruptions if LLSVPs are allowed to move (Flament et al., 2022; Grabreck et al., 2022). Geochemical evidence further supports a deep mantle origin for kimberlites. For example, isotopic studies show that kimberlites share similarities with ocean island basalts, including Sr–Nd–Hf compositions within the range of PREMA (Giuliani et al., 2020). Additional isotopic constraints suggest that kimberlite sources may range from the sub-lithospheric mantle to the transition zone or even deeper mantle reservoirs (e.g., Pearson et al., 2019; Woodhead et al., 2019).

Intriguingly, the mantle source of some kimberlites appears to correlate with the locations of LLSVPs (Torsvik et al., 2014; Giuliani et al., 2021; Dalton et al., 2022; Lee, 2022; Adam and Kempton, 2025). The hypothesis that kimberlites may originate from LLSVPs is consistent with the results obtained in our study. Our results indicate that African kimberlites emplaced during the 260-0 Ma interval are predominantly located over LLSVPs or along their margins. This consistent

association suggests that the African LLSVP has remained relatively stable for at least the past ~260 Ma, and we see a progressive depletion of the mantle source, rather than changes in the position of LLSVPs themselves. Flament et al. (2022) proposed that the African LLSVP assembled as recently as ~60 Ma. Our results, however, suggest a more stable and long-lived structure, indicating that the African LLSVP may have persisted for at least the past ~260 Ma.

In contrast, although some African kimberlites older than 260 Ma were emplaced either on the African or Pacific LLSVPs, most were emplaced away from LLSVPs (Figure 5.3a). We noticed a peculiar period, 590-490 Ma, where none of the kimberlites are emplaced over LLSVPs. An intriguing pattern for this age group is that their present-day locations seem to be along a NE-SW alignment. For this age group, and for other kimberlites, in general, upwelling initiating from LLSVPs may not be the only mechanism operating in the emplacement of kimberlites. In the next sections, we investigate whether the emplacement of kimberlites may be accounted for by other phenomena (e.g., edge-driven convection or rifting).

5.2 LAB gradient and temporal distribution of kimberlite locations.

Edge-driven convection (EDC) is a form of small-scale mantle convection that arises due to lateral variations in lithospheric thickness (King and Anderson, 1998) (Figure 2.4). These variations generate convective instabilities at the boundary between thick and thin lithosphere, producing localized upwellings that can facilitate decompression melting. EDC has been invoked to explain a range of intraplate magmatic features, including the Bermuda Rise (King and Anderson, 1998), volcanism in the Canary Islands (Manjón-Cabeza Córdoba, and Ballmer, 2021), and kimberlite emplacement in North America (Kempton et al., 2019; Adam and Kempton, 2025). In this section, we investigate the potential correlation between kimberlites and the

LAB horizontal gradient, as some studies report that kimberlites are emplaced mainly either along the gradient or along the thinner lithosphere adjacent to the gradient (reference).

For this analysis, we consider the CAM2022 model developed by Priestley et al. (2024) and investigate the present-day lithospheric thickness or LAB, its horizontal gradient, and the ages and locations of kimberlites. In Chapter 4, we showed that kimberlite emplacement through time is broadly associated with either LLSVP locations or the lithosphere–asthenosphere boundary (LAB) gradients. Some kimberlite clusters seem to be emplaced at the margins of cratons (West African, Congo, and Kalahari cratons), but not all of them (Figure 5.4). In particular, the kimberlites with ages between 590 and 490 Ma (Figure 5.5) present an interesting pattern as they are emplaced along a NE-SW alignment, and their backtracked positions do not correlate with LLSVPs (Figure 5.1f). In Figure 5.6, we zoom in on this region to see a potential correlation with LAB or its gradient.

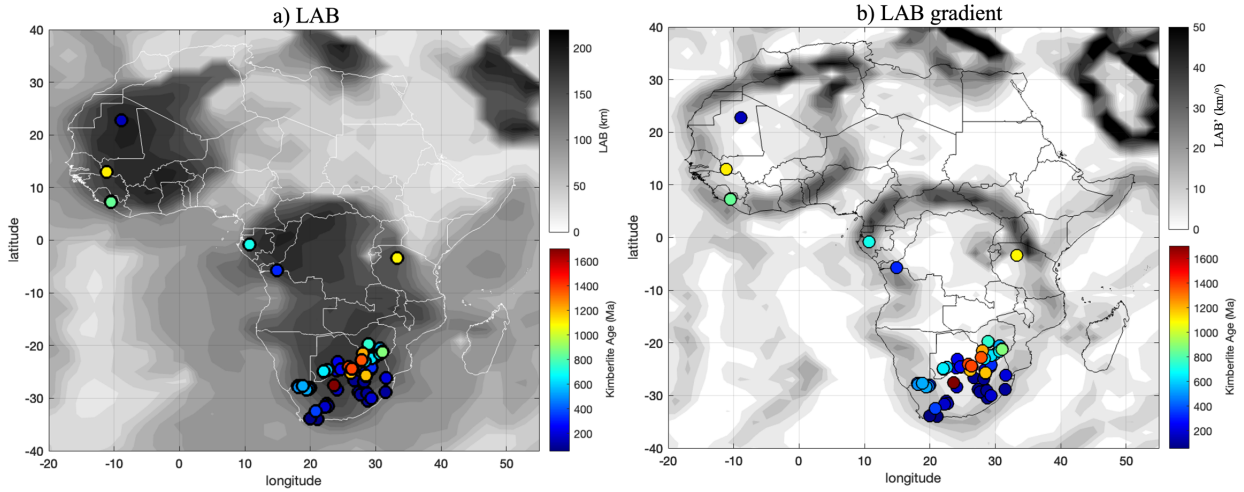


Figure 5.4: Lithosphere-Asthenosphere Boundary (LAB) and LAB gradient for kimberlite clusters not emplaced over LLSVPs. The colored circles display the ages and locations of kimberlites (1800-0 Ma not emplaced over LLSVPs). LAB shown in panel (a) obtained using data from Priestley et al. (2024). Panel (b) shows the corresponding LAB gradient. Country boundaries are shown as white lines in (a) and black lines in (b).

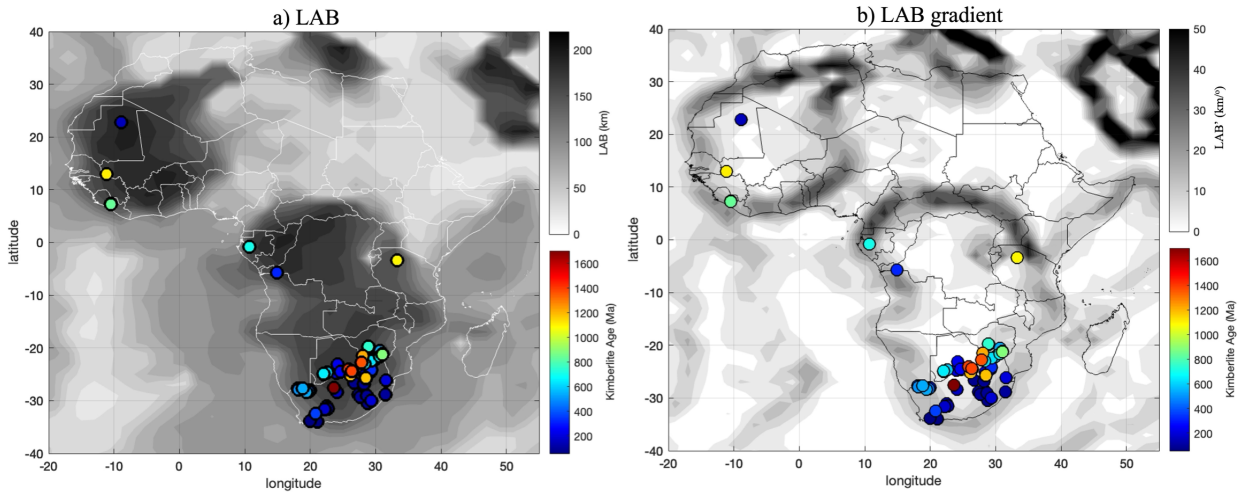


Figure 5.5: Lithosphere-Asthenosphere Boundary (LAB) and LAB gradient for kimberlite clusters. The colored circles display the ages and locations of kimberlites clusters with ages between 590 and 490 Ma. LAB shown in panel (a) obtained using data from Priestley et al. (2024). Panel (b) shows the corresponding LAB gradient. Country boundaries are shown as white lines in (a) and black lines in (b).

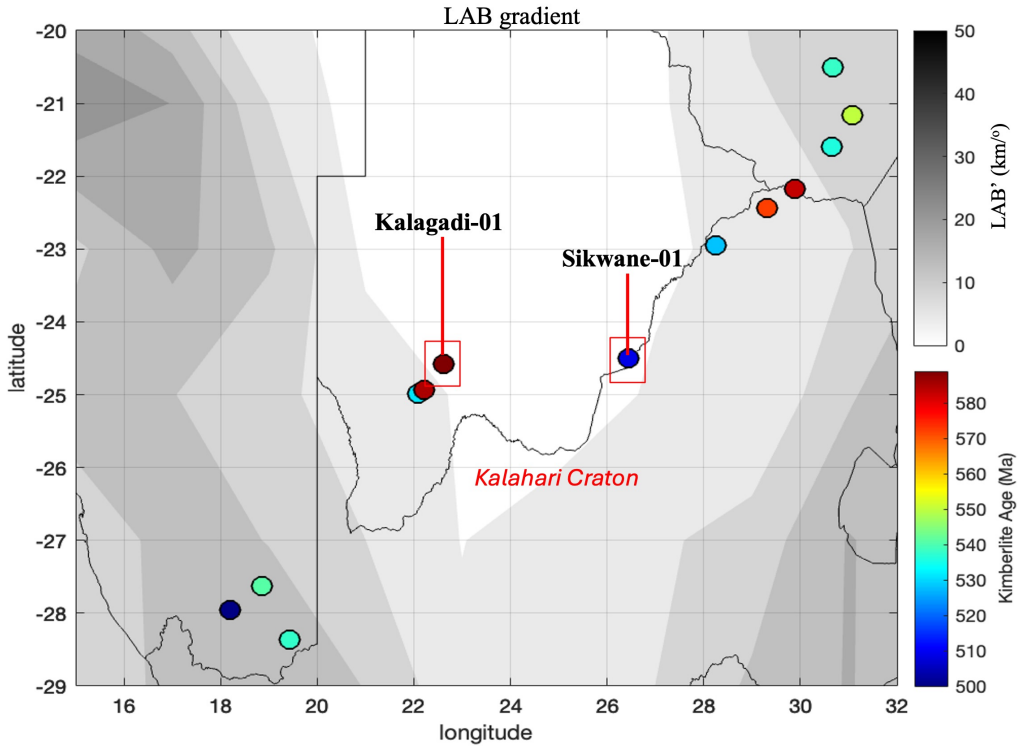


Figure 5.6: Close-up view of the southern part of the Lithosphere-Asthenosphere Boundary (LAB) gradient showing the kimberlite clusters with ages between 590 and 490 Ma. The colored circles display the ages and locations of kimberlites.

Except for the kimberlites in the northeastern part and southwestern part in Figures 5.5 and 5.6, the rest of the kimberlites do not seem to be located on the sharp gradient margin. Kalagadi-04 and Sikwane-01 kimberlites (Figure 5.6), located in Botswana within the Kalahari craton, clearly show no correlation as they lie above regions with a low LAB gradient (white). This suggests that EDC does not seem to be an explanation for the emplacement of kimberlites with ages between 590 and 490 Ma. It could account for the emplacement of other kimberlites (see Figure 5.4).

It is important to note, however, that the LAB used in this study is the present-day configuration, and lithospheric thickness may have differed through time. Some authors argue that the lithosphere thickness has decreased in some areas, especially near regions associated with frequent kimberlite eruptions (e.g., S. Sarkar et al. 2025). In contrast, according to Sudholz and Copley (2025), there have been only minor changes in lithosphere thickness since the Meso-Proterozoic. However, the general architecture of the Kaapvaal Craton as a thick, stable keel surrounded by thinner lithosphere is considered to have been established by the late Archean and preserved through the Phanerozoic (e.g., Begg et al., 2009). Hence, this supports the use of the present-day LAB to constrain EDC contribution.

5.3 Rifting and temporal distribution of kimberlite locations

The role of rifting in kimberlite emplacement has been debated extensively in the literature, with some studies arguing that rift-related lithospheric thinning and faulting provide the structural pathways necessary for rapid melt ascent from the mantle (Jelsma et al., 2009; Tappe et al., 2018). A particularly significant contribution to this debate is that of Gernon et al. (2023), who

demonstrate through a global statistical analysis that kimberlite emplacement is indeed associated with rifting, but with a characteristic temporal lag of approximately 20–30 Ma between the onset of rifting and kimberlite ascent. They propose that rift-induced lithospheric thinning progressively destabilizes the subcontinental lithospheric mantle, generating the volatile-rich partial melts that ultimately ascend as kimberlites after a delay. The present-day kimberlite locations in our study (for example, the 590–490 Ma interval) (Figure 5.5) are examined here in the context of this rift-lag hypothesis. In chapter 4, we showed that there is no obvious correlation between rifts and kimberlites (Figure 4.8); however, the 590-490 Ma interval shows some interesting characteristics.

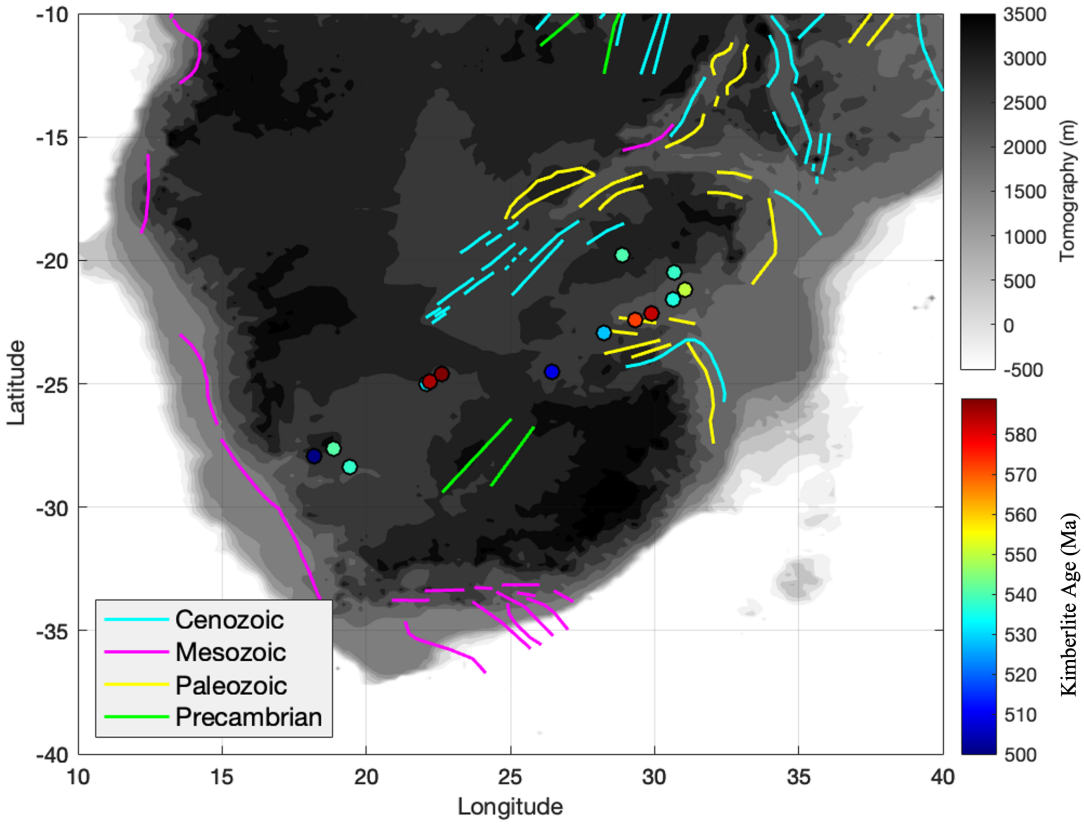


Figure 5.7: Relationship between rift systems and kimberlite locations (590-490 Ma). Precambrian age (~ >541Ma) is reported in green, Paleozoic (~541-252 Ma) is reported in yellow, Mesozoic (~252-66 Ma) is reported in magenta, and Cenozoic (~66 to present) is reported in cyan. Open green circles show kimberlite locations from the 490–590 Ma interval. The grey colormap shows the topography; data from Tozer et al. (2019).

For the 590 to 490 Ma interval, the present-day kimberlite locations show an intriguing spatial relationship with mapped rift systems. Some kimberlites are close to rift traces, especially those that are part of Paleozoic rift systems (white) in the area. Nonetheless, a considerable fraction of the backtracked kimberlites within this interval does not exhibit a distinct spatial correlation with any delineated rift trace, irrespective of rift age. This partial connection may seem to contradict a rift-controlled model at first glance. However, considering the ~30 Ma lag identified by Gernon et al. (2023), a definitive spatial and temporal overlap between kimberlites and active rift traces would not necessarily be expected. The relevant rifting event would have occurred several tens of millions of years before the formation of the kimberlites, and the rift itself may have been in a post-rift or quiescent state during the ascent of the kimberlites.

According to Gernon et al. (2023) rifting episode that caused these kimberlites (490–590 Ma interval) would have started around 620–520 Ma, which is about the same time as the late Pan-African orogenic cycle and the extensional collapse and rifting that affected most of Gondwana during the Neoproterozoic–early Paleozoic transition (e.g., Torsvik et al., 2012).

Despite the conceptual alignment with Gernon et al. (2023), several limitations make it impossible to draw a clear conclusion for this correlation. For example, the rift database used in this study represents manually digitized rift extents that may not fully capture the geometry of all the rift systems or may have been overprinted. To thoroughly test this hypothesis would require a more comprehensive rift dataset and extended analysis, which are currently beyond the scope of the current study but represent a clear direction for research.

In general, our results are consistent with the rift-lag model of Gernon et al. (2023), suggesting that kimberlite emplacement may be associated with lithospheric changes induced by rifting rather than with the rift traces themselves. This suggests that rifts may have facilitated

kimberlite emplacements with ages between 590 and 490 Ma. However, further studies are required to assess this with certainty.

Chapter 6 - Conclusion

Our study aims to provide new constraints on the origin and emplacement of kimberlites by investigating the relative roles of deep mantle structures and lithospheric processes. In particular, we investigate the relationship between backtracked African kimberlite locations and present-day large low shear velocity provinces (LLSVPs), as constrained by multiple seismic tomography models, and assess the potential influence of lithospheric thickness variations and rifting on kimberlite emplacement.

We use the rotation pole developed by Cao et. al. (2024) to backtrack the locations of the kimberlites using the GPlately software (Mather et al., 2023). We use a newly developed method to quantitatively assess the correlation between backtracked African kimberlite positions and LLSVPs based on three recent global seismic tomography models: the SPiRaL developed by Simmon et al. (2021), the TX2019slab model developed by Lu et al. (2019), and the SAVANI model, developed by Auer et al. (2014). We find that younger African kimberlites emplaced between 260 and 0 Ma show a strong, consistent spatial correlation with the African LLSVPs or their margins according to the three considered seismic tomography models. This consistent pattern is in agreement with the hypothesis that at least some kimberlites are related to deep mantle sources. The lack of correlation between some of the kimberlites younger than 260 Ma and LLSVPs may come from the depletion of the kimberlites' source. Our results suggest that the African LLSVP has remained stable, i.e., roughly rooted below the African superswell during the last 260 Myr. This is in contradiction to the hypothesis proposed by Flament et al. (2022) that LLSVPs move over time, and in particular, that the African LLSVP was only assembled during the last 60 Myr.

In contrast, kimberlites older than 260 Ma exhibit a more variable spatial relationship with LLSVPs, making their interpretation less straightforward. We observed a succession of intervals with kimberlites emplaced over LLSVPs, alternating with intervals showing no clear spatial association. With only 51 kimberlite clusters spanning the 1800-260 Ma interval compared to 74 kimberlite clusters in the 260-0 Ma period, we are careful not to overinterpret these older kimberlites. However, our current results suggest that most of the kimberlites older than 260 Ma were not emplaced over LLSVPs. Their weaker or less systematic correlation with LLSVP regions, suggests that other processes may have influenced their emplacement. Although we can only robustly define two statistically meaningful periods: 260-0 Ma (kimberlites emplaced predominantly over the African LLSVP) and 1800-260 Ma (kimberlites mostly not emplaced over LLSVPs), we note an interval (590-490 Ma) during which the backtracked kimberlites show no spatial correlation with LLSVPs, while their present-day locations define an intriguing NE-SW alignment (Figure 5.7)

The comparison with the kimberlites with the LAB and LAB gradients shows that EDC may have helped the emplacement of some kimberlites clusters, but there is no clear indication that EDC has played any role in the emplacement of kimberlites with ages between 590 and 490.

Additionally, the comparison between the present-day location of kimberlites and the rifts ages and locations derived from previous studies (Sengör and Natalin 2000) does allow a clear conclusion about rifting facilitating the emplacement of kimberlites, as recently proposed in the literature (Gernon et al. 2023). Most of the kimberlites are actually located far from rifts. Rifts may have facilitated the emplacement of kimberlites with ages between 590 and 490, but further bibliographic studies are required to assess this with certainty.

Overall, our study supports the hypothesis that emplacement of kimberlites has been influenced by long-lived deep mantle structures, i.e., LLSVPs, for at least the last 260 Myr. We also point out that the source of kimberlites may be depleted over time by kimberlite extraction. Our results suggest that the African LLSVPs have remained stable, i.e., roughly rooted below the African superswell during the last 260 Myr, in contradiction with other recent studies (e.g., Flament et al., 2022) who suggested a much later assembly of the African LLSVPs (~60 Myr). In the future, it would be interesting to incorporate geochemical constraints to better characterize the mantle source regions. In other words, study the geochemical signatures of the kimberlites to determine whether there are differences in the geochemical signatures of kimberlites emplaced over LLSVPs and those that are not.

References

Adam, C., & Kempton, P. D. (2025). Secular variation in the North American kimberlite formation: The variable connection to LLSVPs. *Geochemistry, Geophysics, Geosystems*, 26, e2025GC012528. https://doi.org/10.1029/2025GC012528

Arndt, N.T., Guitreau, M., Boullier, A.M., le Roex, A., Tommasi, A., Cordier, P., Sobolev, A., 2010. Olivine, and the origin of kimberlite. *Journal of Petrology* 51, 573–602. doi: 10.1093/petrology/egp095

Artemieva, I. M. (2009). The continental lithosphere: Reconciling thermal, seismic, and petrologic data. *Lithos*, *109*(1-2), 23–46. doi: 10.1016/j.lithos.2008.09.015

Auer, L., Boschi, L., Becker, T. W., Nissen-Meyer, T., & Giardini, D. (2014). Savani: A variable resolution whole-mantle model of anisotropic shear velocity variations based on multiple data sets. *Journal of Geophysical Research: Solid Earth, 119*(4), 3006–3034. https://doi.org/10. 1002/2013JB010773

Ballmer, M. D., Conrad, C. P., Smith, E. I., & Johnsen, R. (2015). Intraplate volcanism at the edges of the Colorado Plateau sustained by a combination of triggered edge-driven convection and shear-driven upwelling. *Geochemistry, Geophysics, Geosystems*, 16(2), 366–379. https:// doi.org/10.1002/2014GC005641

Becker, M., & Le Roex, A.P., 2006. Geochemistry of South African On- and Off-craton, Group I and Group II Kimberlites: Petrogenesis and Source Region Evolution. *Journal of Petrology* 47, 673-703. doi: 10.1093/petrology/egi089

Begg, G. C., Griffin, W. L., Natapov, L. M., et al. (2009). The lithospheric architecture of Africa: Seismic tomography, mantle petrology, and tectonic evolution. *Geosphere*, 5(1), 23–50. doi: 10.1130/GES00179.1

Brett, R.C., Russell, J.K., Andrews, G.D.M., Jones, T.J., 2015. The ascent of kimberlite: insights from olivine. *Earth and Planetary Science Letters 424*, 119–131. doi: 10.1016/j.epsl.2015.05.024

Bodur, Ö. F., & Flament, N. (2023). Kimberlite magmatism fed by upwelling above mobile basal mantle structures. *Nature Geoscience*, 16(6), 534–540. https://doi.org/10.1038/s41561-023-01181-8

Boyden, J., Müller, R. D., Gurnis, M., Torsvik, T. H., Clark, J. A., Turner, M., Ivey-Law, H., Watson, R. J., & Cannon, J. S. (2011). Next-generation plate-tectonic reconstructions using GPlates. In G.R. Keller, & C. Baru (Eds.), In *Geoinformatics: Cyberinfrastructure for the Solid Earth Sciences*(pp.95-114). Cambridge: Cambridge University Press.

Burke, K. (2011). Plate Tectonics, the Wilson Cycle, and Mantle Plumes: Geodynamics from the Top. *Annual Review of Earth and Planetary Sciences*, *39*(1), 1–29. doi: 10.1146/annurev-earth-040809-152521

Burke, K., & Torsvik, T. H. (2004). Derivation of Large Igneous Provinces of the past 200 million years from long-term heterogeneities in the deep mantle. *Earth and Planetary Science Letters,* 227(3–4), 531–538. https://doi.org/10.1016/j.epsl.2004.09.015

Cao, X., Collins, A. S., Pisarevsky, S., Flament, N., Li, S., Hasterok, D., & Müller, R. D. (2024). Earth's tectonic and plate boundary evolution over 1.8 billion years. *Geoscience Frontiers*, 15(6), 101922. doi: https://doi.org/10.1016/j.gsf.2024.101922

Cox, A., & Hart, R. B. (1986). *Plate tectonics: How it works*. Blackwell Scientific Publications, Inc.

Courtillot, V., Davaille, A., Besse, J., & Stock, J. (2003). Three distinct types of hotspots in the Earth's mantle. *Earth and Planetary Science Letters*, *205*(3), 295–308. doi: 10.1016/S0012-821X(02)01048-8

Currie, C. A., & Beaumont, C. (2011). Are diamond-bearing Cretaceous kimberlites related to Low-angle subduction beneath western North America? *Earth and Planetary Science Letters*, *303*(1), 59–70. doi: 10.1016/j.epsl.2010.12.036

Dalton, H., Giuliani, A., Hergt, J., Phillips, D., O'Brien, H., Ballmer, M. D., et al. (2022). Geodynamic and isotopic constraints on the genesis of kimberlites, lamproites and related magmas from the Finnish segment of the Karelian craton. *Geochemistry, Geophysics, Geosystems*, 23(8), e2021GC010324. https://doi.org/10.1029/2021GC010324

Dalton, H., Giuliani, A., & Pearson, D. G. (2024). A new global kimberlite geochemistry dataset: The benefits of open and complete data sharing. *In Paper Presented at 12th International Kimberlite Conference, Extended Abstract No. 12th International Kimberlite Conference*, 8-12 July 2024. Yellowknife. Canada.

Davies, D. R., Goes, S., & Lau, H. C. P. (2015). Thermally dominated deep mantle LLSVPs: A Review. In A. Khan & F. Deschamps (Eds.), *The Earth's Heterogeneous Mantle: A Geophysical, Geodynamical, and Geochemical Perspective* (pp. 441–477). Springer International Publishing. doi: 10.1007/978-3-319-15627-9_14

Davaille, A. (1999). Simultaneous generation of hotspots and superswells by convection in a heterogeneous planetary mantle. *Nature*, *402*(6763), 756-760. doi: 10.1038/45461

Davaille, A., & Romanowicz, B. (2020). Deflating the LLSVPs: Bundles of mantle thermochemical plumes rather than thick stagnant "piles." *Tectonics*, *39*(10), e2020TC006265. doi: 10.1029/2020TC006265

Dawson, J.B., 1980. Kimberlites and their xenoliths. *Springer-Verlag*, New York, 252 pp.

DeMets, C., Gordon, R. G., & Argus, D. F. (2010). Geologically current plate motions. *Geophysical Journal* International*, 181*, 1–80. https://doi. org/10.1111/j.1365-246X.2009.04491.x

Dziewonski, A. M., Lekic, V., & Romanowicz, B. A. (2010). Mantle anchor structure: An argument for bottom up tectonics. *Earth and Planetary Science Letters*, *299*(1), 69–79. doi: 10.1016/j.epsl.2010.08.013

Flament, N., Bodur, Ö. F., Williams, S. E., & Merdith, A. S. (2022). Assembly of the basal mantle structure beneath Africa. *Nature*, 603(7903), 846–851. https://doi.org/10.1038/s41586-022-04538-y

Faure, S. (2010). *World kimberlites CONSOREM database.* Université du Québec à Montréal.

http://www.consorem.ca.

Foley, S. F. (2011). A reappraisal of redox melting in the Earth's mantle as a function of tectonic setting and time. *Journal of Petrology*, *52*(7–8), 1363–1391. doi: 10.1093/petrology/egq061

Francis, D., & Patterson, M. (2009). Kimberlites and aillikites as probes of the continental Lithospheric mantle. *Lithos*, *109*(1), 72–80. doi: 10.1016/j.lithos.2008.05.007

Garnero, E. J., McNamara, A. K., & Shim, S. H. (2016). Continent-sized anomalous zones with low seismic velocity at the base of Earth's mantle. *Nature Geoscience*, 9(7), 481-489. https://doi.org/10.1038/ngeo2733

Gernon, T. M., Jones, S. M., Brune, S., Hincks, T. K., Palme, M. R., Schumacker, J. C., et al. (2023). Rift-induced disruption of cratonic keels drives kimberlite volcanism. *Nature*, 620(7973), 344–350. https://doi.org/10.1038/s41586-023-06193-3

Giuliani, A., Dalton, H., & Pearson, D. G. (2025). Kimberlites: The deepest geochemical probes of Earth. In A. Anbar & D. Weis (Eds.), *Treatise on geochemistry* (3rd ed., pp. 159–230). Elsevier. Oxford. https://doi.org/10.1016/B978-0-323-99762-1.00064-4

Giuliani, A., Schmidt, M.W., Torsvik, T.H., Fedortchouk, Y. (2023). Genesis and Evolution of Kimberlite. *Nature Reviews Earth and Environment,* 4, 738-753. doi: 10.1038/s43017-023-00481-2

Giuliani, A., Jackson, M. G., Fitzpayne, A., & Dalton, H. (2021). Remnants of early Earth differentiation in the deepest mantle-derived lavas. *Proceedings of the National Academy of Sciences*, *118*(1). doi: 10.1073/pnas.2015211118

Golovin, A. V., Sharygin, I. S., Kamenetsky, V. S., Korsakov, A. V., & Yaxley, G. M. (2018). Alkali-carbonate melts from the base of cratonic lithospheric mantle: Links to kimberlites. *Chemical Geology*, *483*, 261–274. doi: 10.1016/j.chemgeo.2018.02.016

Grabreck, A., Flament, N., & Bodur, Ö. F. (2022). Mapping global kimberlite potential from reconstructions of mantle flow over the past billion years. *PLoS One,* 17(6), e0268066. https://doi.org/10.1371/journal.pone.0268066

Gurnis, M., Turner, M., Zahirovic, S., DiCaprio, L., Spasojevic, S., Müller, R. D., et al. (2012). Plate tectonic reconstructions with continuously closing plates. *Computers & Geosciences*, 38(1), 35–42. https://doi.org/10.1016/j.cageo.2011.04.014

Gurnis, M. (2000). Mantle convection and the structure of the mantle. *Proceedings of the National Academy of Sciences*, 9(7), 4-5. doi: 10.1073/pnas.97.1.4

Gurney, J.J., Jakob, W.R.O., Dawson, J.B., 1979. Megacrysts from the Monastery kimberlite pipe, South Africa. In: Boyd, F.R., Meyer, H.O.A. (Eds.), The Mantle Sample: Inclusions in Kimberlites and Other Volcanics. *American Geophysical Union*, Washington, D. C., 227-243.

Heaman, L., Kjarsgaard, B., & Creaser, R. (2003). The timing of kimberlite magmatism in North America: Implications for global kimberlite genesis and diamond exploration. *Lithos*, *71*(2), 153–184. doi: 10.1016/j.lithos.2003.07.005

Heaman, L. M., & Kjarsgaard, B. A. (2000). Timing of eastern North American kimberlite magmatism: Continental extension of the Great Meteor hotspot track? *Earth and Planetary Science Letters*, *178*(3), 253–268. doi: 10.1016/S0012-821X(00)00079-0

Heaman, L. M., Pell, J., Grütter, H. S., & Creaser, R. A. (2015). U–Pb geochronology and Sr/Nd isotope compositions of groundmass perovskite from the newly discovered Jurassic Chidliak kimberlite field, Baffin Island, Canada. *Earth and Planetary Science Letters*, *415*, 183–199. doi: 10.1016/j.epsl.2014.12.056

Hofmann, A. W. (1988). Chemical differentiation of the Earth: The relationship between mantle, continental crust, and oceanic crust. *Earth and Planetary Science Letters*, *90*(3), 297–314. doi: 10.1016/0012-821X(88)90132-X

ICPAC (Intergovernmental Authority on Development Climate Prediction and Applications Centre). *Country administrative boundaries* Geospatial dataset. ICPAC Geoportal. Retrieved (June 24, 2025), https://geoportal.icpac.net/layers/geonode%3Aafr g2014 2013 0

Jelsma, H., Barnett, W., Richards, S., & Lister, G. (2008). Tectonic setting of kimberlites. *Lithos*, 112, 155–165. https://doi.org/10.1016/j.lithos. 2009.06.030

Jollands, M. C., Hanger, B. J., Yaxley, G. M., Hermann, J., & Kilburn, M. R. (2018). Timescales between mantle metasomatism and kimberlite ascent indicated by diffusion profiles in garnet crystals from peridotite xenoliths. *Earth and Planetary Science Letters*, *481*, 143–153. doi: 10.1016/j.epsl.2017.10.021

Jourdan, F., Féraud, G., Bertrand, H., & Kampunzu, A. B. (2007). The Karoo large igneous province: Brevity, origin, and relation to kimberlites. *Journal of Petrology*, 48(3), 581–605. doi: 10.1093/petrology/egl069

Kellogg, L. H., Hager, B. H., & Hilst, R. D. van der. (1999). Compositional Stratification in the Deep Mantle. *Science*, *283*(5409), 1881-1884. doi: 10.1126/science.283.5409.1881

Kamenetsky, V. S., Kamenetsky, M. B., Sobolev, A.V., Golovin, A. V., Demouchy, S., Faure, K., Sharygin, V. V., Kuzmin, D. V. (2008). Olivine in the Udachanya-East Kimberlite (Yakutia, Russia): Types, compositions, and origins. *Journal of Petrology*, 49, 823-839. doi: 10.1093/petrology/dgn007

Kempton, P. D., Rogers, K., & Brueseke, M. E. (2019). Windows into the Cretaceous mantle of the North American midcontinent—Kimberlites of Riley County, Kansas. In M. K. Schulmeister & J. S. Aber (Eds.), *Exploring Extreme and Unusual Geology in the Stable Midcontinent: Field Excursions for the 2019 GSA South-Central, North-Central, and Rocky Mountain Sections Joint Meeting* (Vol. 52, p. 0). Geological Society of America. doi: 10.1130/2019.0052(03)

King, S. D., & Adam, C. (2014). Hotspot swells revisited. *Physics of the Earth and Planetary Interiors*, *235*, 66–83. doi: 10.1016/j.pepi.2014.07.006

King, S. D., & Anderson, D. L. (1998). Edge-driven convection. *Earth and Planetary Science Letters*, *160*(3), 289–296. doi: 10.1016/S0012-821X(98)00089-2

King, S. D., & Ritsema, J. (2000). African Hot Spot Volcanism: Small-Scale Convection in the Upper Mantle Beneath Cratons. *Science*, 290(5949), 1137-1140. doi: 10.1126/science.290.5494.1137

Kopylova, M. G., & Caro, G. (2004). Mantle xenoliths from the southeastern Slave Craton: Evidence for chemical zonation in a thick, cold lithosphere. *Journal of Petrology*, *45*(5), 1045–1067. doi: 10.1093/petrology/egh003

Kjarsgaard, B. A., de Wit, M., Heaman, L. M., Pearson, D. G., Stiefenhofer, J., Janusczcak, N., & Shirey, S. B. (2022). A review of the geology of global diamond mines and deposits. *Reviews in Mineralogy and Geochemistry*, 88(1), 1–117. https://doi.org/10.2138/rmg.2022.88.01

Kjarsgaard, B. A., Heaman, L. M., Sarkar, C., & Pearson, D. G. (2017). The North America Mid-Cretaceous kimberlite corridor: Wet, edge-driven decompression melting of an OIB-type deep mantle source. *Geochemistry, Geophysics, Geosystems*, *18*(7), 2727–2747. doi: 10.1002/2016GC006761

Lu, C., Grand, S. P., Lai, H., & Garnero, E. J. (2019). TX2019slab: A new P and S tomography model incorporating subducting slabs. *Journal of Geophysical Research: Solid Earth*, 124(11), 11549–11567. https://doi.org/10.1029/2019JB017448

Kreemer, C., Blewitt, G., & Klein, E. C. (2014). A geodetic plate motion and Global Strain Rate Model. *Geochemistry, Geophysics, Geosystems*, *15*(10), 3849–3889. doi: 10.1002/2014GC005407

Kreielkamp, P., Stein, C., & Hansen, U. (2022). LLSVPs of primordial origin: Implications for the evolution of plate tectonics. *Earth and Planetary Science Letters*, *579*. doi: 10.1016/j.epsl.2021.117357

le Roex, A. P. (1986). Geochemical correlation between southern African kimberlites and South Atlantic hotspots. *Nature*, 324(6094), 243–245. https://doi.org/10.1038/324243a0

Lee, E. (2022). Backtracking potential mantle sources of North American kimberlites through kinematic models to constrain their origin, *Master's thesis. Kansas State University.* Retrieved from https://hdl.handle.net/2097/42890

Li, M. (2021). The cycling of subducted oceanic crust in the Earth's deep mantle. In H. Marquardt, M. Ballmer, S. Cottaar, & J. Konter (Eds.), *Mantle convection and surface expressions, Geophysical Monograph series* (pp. 303-328). https://doi.org/10.1002/9781119528609.ch12

Lu, C., Grand, S. P., Lai, H., & Garnero, E. J. (2019). TX2019slab: A new P and S tomography model incorporating subducting slabs. *Journal of Geophysical Research: Solid Earth, 124*(11), 11549–11567. https://doi.org/10.1029/2019JB017448

Lupini, I., Kempton, P., Möller, A., & Adam, C. (2023). U-Pb emplacement ages of Kansas lamproites and kimberlites. *In Paper Presented at GSA Rocky Mountain Section—73rd Annual Meeting, Fort Collins, CO* (Vol. 55). https://doi.org/10.1130/abs/2023RM-387750

Manjón-Cabeza Córdoba, A., & Ballmer, M. D. (2021). The role of edge-driven convection in the generation of volcanism – Part 1: A 2D systematic study. *Solid Earth*, *12*(3), 613–632. doi: 10.5194/se-12-613-2021

Mather, B.R., Müller, R.D., Zahirovic, S., Cannon, J., Chin, M., Ilano, L., Wright, N.M., Alfonso, C., Williams, S., Tetley, M., Merdith, A. (2023) Deep time spatio-temporal data analysis using pyGPlates with PlateTectonicTools and GPlately. *Geoscience Data Journal*, 1–8. Available from: https://doi.org/10.1002/gdj3.185

McCandless, T.E. (1999). Kimberlites: Mantle Expressions of Deep-Seated Subduction. *International Kimberlite Conference: Extended Abstract*, 7(1), 558-560. doi.org/10.29173/ikc2803

McNamara, A. K. (2019). A review of large low shear velocity provinces and ultra-low velocity zones. *Tectonophysics*, *760*, 199–220. doi: 10.1016/j.tecto.2018.04.015

Moore, A.E., 1988, Olivine: a monitor of magma evolutionary paths in kimberlites and olivine melilitites: *Contributions to Mineralogy and Petrology* 99, 238 – 248. doi: 10.1007/BF00375363

Mitchell, R.H., 1995. Kimberlites, Orangeites and Related Rocks. Plenum Press, New York, 410 pp.

Mitchell, R. H. (1991). Kimberlites and lamproites: Primary sources of diamond. *Geoscience Canada*, *18*.

Mitchell, R.H., 1986. Kimberlites: Mineralogy, Geochemistry and Petrology. Plenum Publishing Company, New York, 442 pp.

Merdith, A. S., Williams, S. E., Collins, A. S., Tetley, M. G., Mulder, J. A., Blades, M. L., Young, A., Armistead, S. E., Cannon, J., Zahirovic, S., & Müller, R. D. (2021). Extending full-plate tectonic models into deep time: Linking the Neoproterozoic and the Phanerozoic. *Earth-Science Reviews*, *214*(103477). doi: 10.1016/j.earscirev.2020.103477

Moore, A. E., Blenkinsop, T., & Cotterill, F. P. D. (2008). Controls on post-Gondwana alkaline volcanism in southern Africa. *Earth and Planetary Science Letters*, 268(1–2), 151–164. doi: 10.1016/j.epsl.2008.01.007

Müller, R. D., Cannon, J., Qin, X., Watson, R. J., Gurnis, M., Williams, S., et al. (2018). GPlates: Building a virtual Earth through deep time. *Geochemistry, Geophysics, Geosystems*, 19(7), 2243–2261. https://doi.org/10.1029/2018GC007584

Müller, R. D., Zahirovic, S., Williams, S. E., Cannon, J., Seton, M., Bower, D. J., et al. (2019). A global plate model including lithospheric deformation along major rifts and orogens since the Triassic. *Tectonics, 38*(6), 1884–1907. https://doi.org/10.1029/2018TC005462

Mulyukova, E., Steinberger, B., Dabrowski, M., & Sobolev, S. V. (2015). Survival of LLSVPs for billions of years in a vigorously convecting mantle: Replenishment and destruction of chemical anomaly. *Journal of Geophysical Research: Solid Earth*, *120*(5), 3824–3847. doi: 10.1002/2014JB011688

Niu, Y. (2018). Origin of the LLSVPs at the base of the mantle is a consequence of plate tectonics – A petrological and geochemical perspective. *Geoscience Frontiers*, *9*(5), 1265–1278. doi: 10.1016/j.gsf.2018.03.005

Niu, Y., & O'Hara, M. J. (2003). Origin of ocean island basalts: A new perspective from petrology, geochemistry, and mineral physics considerations. *Journal of Geophysical Research: Solid Earth*, *108*(B4). doi: 10.1029/2002JB002048

Nyblade, A. A., & Robinson, S. W. (1994). The African superswell. *Geophysical Research Letters*, 21(9), 765–768. doi: 10.1029/94GL00631

Pearson, D. G., Woodhead, J., & Janney, P. E. (2019). Kimberlites as geochemical probes of Earth's mantle. *Elements*, 15(6), 382–392. https://doi. org/10.2138/gselements.15.6.387

Pilbeam, L.H., Nielsen, T.F.D., Waight, T.E., 2013. Digestion fractional crystallization (DFC): an important process in the genesis of kimberlites. Evidence from olivine in the Majuagaa

kimberlite, southern West Greenland. *Journal of Petrology* 54, 1399–1425. doi: 10.1093/petrology/egt012

Priestley, K., Ho, T., Takei, Y., & McKenzie, D. (2024). The thermal and anisotropic structure of the top 300 Km of the mantle. *Earth and Planetary Science Letters, 626*, 118525. https://doi.org/10.1016/j.epsl.2023.118525

Ranger, I. M., Heaman, L. M., Pearson, D. G., Muntener, C., & Zhuk, V. (2018). Punctuated, long-lived emplacement history of the Renard 2 kimberlite, Canada, revealed by new high precision U-Pb groundmass perovskite dating. *Mineralogy and Petrology*, 112(S2), 639–651. https:// doi.org/10.1007/s00710-018-0629-0

Ritsema, J., van Heijst, H. J., & Woodhouse, J. H. (1999). Complex shear wave velocity structure beneath Africa and Iceland. *Science*, 286(5446), 1925-1928. doi: 10.1126/science.286.5446.1925

Rohrbach, A., & Schmidt, M. W. (2011). Redox freezing and melting in the Earth's deep mantle resulting from carbon–iron redox coupling. *Nature*, 472(7342), 209–212. https://doi.org/10.1038/nature09899

Sarkar, C., Heaman, L. M., & Pearson, D. G. (2015). Duration and periodicity of kimberlite volcanic activity in the Lac de Gras kimberlite field, Canada and some recommendations for kimberlite geochronology. *Lithos, 218–219*, 155-166.https://doi.org/10.1016/j.lithos.2015.01.017

Sarkar, S., Giuliani, A., Dalton, H., Munch, F., Phillips, D., & Ghosh, S. (2025). Testing the hypothesis of secular thinning and compositional evolution of the lithospheric mantle beneath cratons: Implications for kimberlite magmatism. *Mineralogy and Petrology*, 1–15. https://doi.org/10.1007/s00710-025-00924-2

Sengör, A. M. C., & Natalin, B. A. (2001). Rifts of the world. In R. E. Ernst & K. L. Buchan (Eds.), Mantle Plumes: Their Identification Through Time. *Geological Society of America Special Paper* 352, pp. 389–482. doi: https://doi.org/10.1130/0-8137-2352-3.389

Simmons, N. A., Myers, S. C., Morency, C., Chiang, A., & Knapp, D. R. (2021). SPiRaL: A multi-resolution global tomography model of seismic wave speeds and radial anisotropy variations in the crust and mantle. *Geophysical Journal International, 227*(2), 1366–1391. https://doi.org/10. 1093/gji /ggab277

Smit, K., & Shirey, S. (2019). Kimberlites: Earth's diamond delivery system. *Gems and Gemology*, *55*, 270–276.

Smith, C.B., 1983. Pb, Sr, and Nd isotopic evidence for sources of African kimberlite. *Nature* 304, 51 –54. doi: 10.1038/304051a0

Stamm, N., & Schmidt, M. W. (2017). Asthenospheric kimberlites: Volatile contents and bulk compositions at 7 GPa. *Earth and Planetary Science Letters*, *474*, 309–321. doi: 10.1016/j.epsl.2017.06.037

Sudholz, Z. J., & Copley, A. (2025). Xenolith constraints on the mantle potential temperature and thickness of cratonic roots through time. *Geophysical Research Letters, 52*(2), e2024GL112851. https://doi.org/10.1029/2024GL112851

Tappe, S., Smart, K., Torsvik, T., Massuyeau, M., & de Wit, M. (2018). Geodynamics of kimberlites on a cooling Earth: Clues to plate tectonic evolution and deep volatile cycles. *Earth and Planetary Science Letters*, *484*, 1–14. doi: 10.1016/j.epsl.2017.12.013

Tappe, S., Kjarsgaard, B. A., Kurszlaukis, S., Nowell, G. M., & Phillips, D. (2014). Petrology and Nd–Hf isotope geochemistry of the Neoproterozoic Amon kimberlite sills, Baffin Island (Canada): Evidence for deep mantle magmatic activity linked to supercontinent cycles. *Journal of Petrology*, *55*(10), 2003–2042. doi: 10.1093/petrology/egu048

Tolstikhin, I., & Hofmann, A. W. (2005). Early crust on top of the Earth's core. *Physics of the Earth and Planetary Interiors, 148*(2–4), 109–130. https://doi.org/10.1016/j.pepi.2004.05.011

Tolstikhin, I. N., Kramers, J. D., & Hofmann, A. W. (2006). A chemical Earth model with whole mantle convection: The importance of a core- mantle boundary layer (D″) and its early formation. *Chemical Geology, 226*(3–4), 79–99. https://doi.org/10.1016/j.chemgeo.2005.09.015

Torsvik, T. H., Steinberger, B., Ashwal, L. D., Doubrovine, P. V., & Trønnes, R. G. (2016). Earth evolution and dynamics—a tribute to Kevin Burke. *Canadian Journal of Earth Sciences*, *53*(11), 1073–1087. doi: 10.1139/cjes-2015-0228

Torsvik, T. H., van der Voo, R., Doubrovine, P. V., Burke, K., Steinberger, B., Ashwal, L. D., Trønnes, R. G., Webb, S. J., & Bull, A. L. (2014). Deep mantle structure as a reference frame for movements in and on the Earth. *Proceedings of the National Academy of Sciences*, *111*(24), 8735–8740. doi: 10.1073/pnas.1318135111

Torsvik, T. H., Van der Voo, R., Preeden, U., Mac Niocaill, C., Steinberger, B., Doubrovine, P. V., van Hinsbergen, D. J. J., Domeier, M., Gaina, C., Tohver, E., Meert, J. G., McCausland, P. J. A., & Cocks, L. R. M. (2012). Phanerozoic polar wander,81 palaeogeography and dynamics. *Earth-Science Reviews*, *114*(3), 325–368. doi: 10.1016/j.earscirev.2012.06.007

Tozer, B., Sandwell, D. T., Smith, W. H. F., Olson, C., Beale, J. R., & Wessel, P. (2019). Global bathymetry and topography at 15 arc sec: SRTM15+. *Earth and Space Science*, 6(10), 1847–1864. https://doi.org/10.1029/2019ea000658

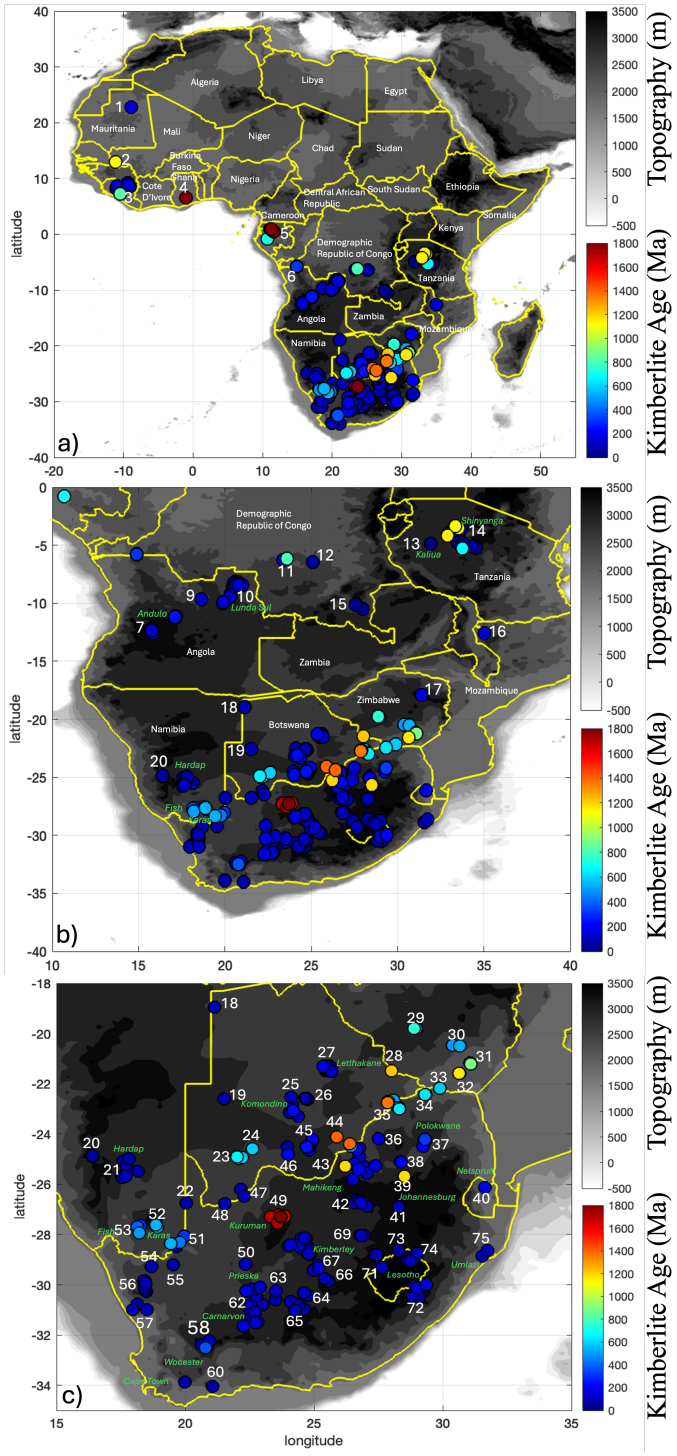
Woodhead, J., Hergt, J., Giuliani, A., Maas, R., Phillips, D., Pearson, D. G., & Nowell, G. (2019). Kimberlites reveal 2.5-billion-year evolution of a deep, isolated mantle reservoir. *Nature*, *573*, 578-581. doi: 10.1038/s41586-019-1574-8

Young, A., Flament, N., Maloney, K., Williams, S., Matthews, K., Zahirovic, S., & Müller, R. D. (2019). Global kinematics of tectonic plates and subduction zones since the late Paleozoic Era. *Geoscience Frontiers*, *10*(3), 989–1013. doi: 10.1016/j.gsf.2018.05.011

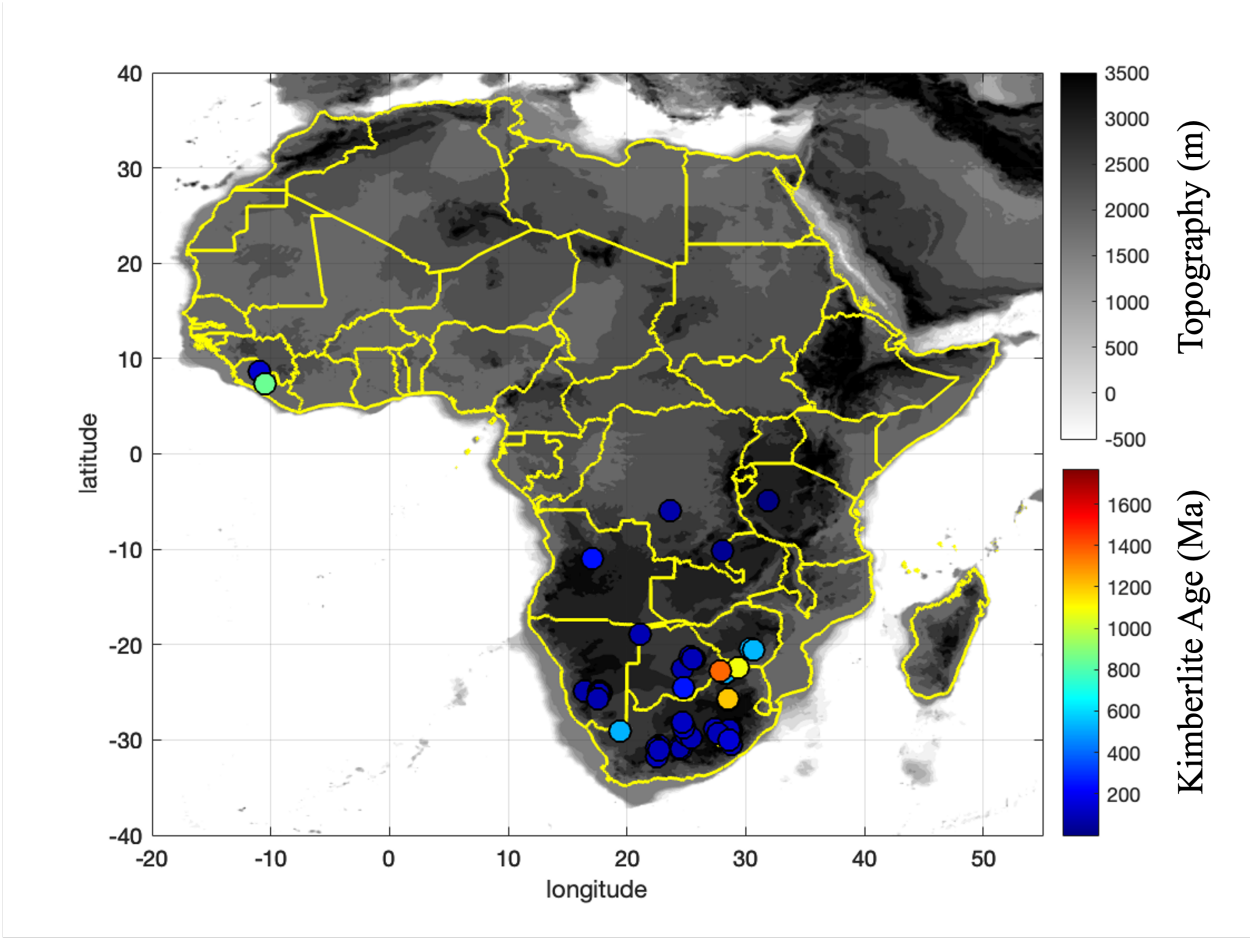
Zurevinski, S. E., Heaman, L. M., Ceaser, R. A., & Strand, P. (2008). The Churchill kimberlite field, NU, Canada: Petrography, mineral chemistry and geochronology. *Canadian Journal of Earth Sciences, 45*(9), 1039–1059. https://doi.org/10.1139/E08-052

Appendix A - Cluster Description

This appendix provides detailed information for each cluster based mainly on the database of Tappe et al. (2018). For each cluster, we report the coordinates, locality, and corresponding line number as listed in the Supplementary Table A of Tappe et al. (2019). For example, in Cluster 1, further information on the kimberlite with the age of 154 Ma can be found in line 567; information on the kimberlite with the age of 600 Ma can be found in line 192, etc. A total of 75 regional clusters is defined based on these data (Figure A.1). The cluster numbers are assigned randomly. The kimberlite ages we keep for our cluster analysis are underlined. We have also investigated whether any supplementary data were available from the Dalton et al. (2024) database (Figure A.2).



Appendix Figure A.1: Kimberlite database designed in this study over the African continent based on data from Tappe et al. (2018). The color circles display the ages and locations of kimberlites. The numbers are the number of clusters created in our study. The grey colormap shows the topography: data from Tozer et al. (2019). The yellow lines are the country boundaries (data from ICPAC GEOPORTAL). (a) Global view over the African continent; (b) Enlarged view of central-southern African continent; (c) Enlarged view of southwestern Africa.



Appendix Figure A.2: Database designed by Dalton et al. (2024) over the African continent. The color circles display the ages and locations of kimberlites. The grey colormap shows the topography: data from Tozer et al. (2019). The yellow lines are the country boundaries (data from ICPAC GEOPORTAL).

Cluster 1: Africa, Mauritania

There is only one age provided by Tappe et al. (2018) for this cluster: 154 Ma, and we retain this age in our study.

Corresponding line number from Supplementary Table A from Tappe et al. (2018) is 567.

Dalton et al. (2024) have no data for this cluster.

Cluster 2: Africa, Mali

The ages provided by Tappe et al. (2018) for this cluster are reported below in Ma. The ages we keep for our study are underlined.

<u>600</u> <u>1110</u>

Corresponding line numbers from Supplementary Table A from Tappe et al. (2018) are as follows: 192 94

Dalton et al. (2024) have no data for this cluster.

Cluster 3: Africa, Guinea, South Africa, Liberia

The ages provided by Tappe et al. (2018) for this cluster are reported below in Ma. The ages we keep for our study are underlined.

<u>95</u> 127 139 140 143 146 155 <u>156</u> <u>791</u> <u>841</u>

Corresponding line numbers from Supplementary Table A from Tappe et al. (2018) are as follows: 816 695 641 634 626 608 564 557 169 161.

Dalton et al. (2024) report 65 samples with an age of 95 Ma, 20 samples with an age of 143 Ma, and one sample with an age of 846 Ma; these eruptive episodes are already included in Tappe et al. (2018).

Cluster 4: Africa, Ghana

There is only one age provided by Tappe et al. (2018) for this cluster: 2029 Ma.

Corresponding line number from Supplementary Table A from Tappe et al. (2018) is 8.

Dalton et al. (2024) have no data for this cluster.

Cluster 5: Africa, Gabon

The ages provided by Tappe et al. (2018) for this cluster are reported below in Ma. The ages we keep for our study are underlined.

708 1850 2000 2000 2029 2235 2500 2848

Corresponding line numbers from Supplementary Table A from Tappe et al. (2018) are as follows:

176 17 11 10 7 3 2 1

Dalton et al. (2024) have no data for this cluster.

Cluster 6: Africa, Congo

The ages provided by Tappe et al. (2018) for this cluster are reported below in Ma. The ages we keep for our study are underlined.

322 322

Corresponding line numbers from Supplementary Table A from Tappe et al. (2018) are as follows:

387 386

Dalton et al. (2024) have no data for this cluster.

Cluster 7: Africa, Angola, South-west of Bie

The ages provided by Tappe et al. (2018) for this cluster are reported below in Ma. The ages we keep for our study are underlined.

133 134 134 136

Corresponding line numbers from Supplementary Table A from Tappe et al. (2018) are as follows:

674 664 663 653

Dalton et al. (2024) have no data for this cluster.

Cluster 8: Africa, Angola, North-east of Andulo

The ages provided by Tappe et al. (2018) for this cluster are reported below in Ma. The ages we keep for our study are underlined.

216 221 221 222 229 233 235 236 236 236 238 239 245 250 252

Corresponding line numbers from Supplementary Table A from Tappe et al. (2018) are as follows:

455 452 449 441 439 436 432 431 430 425 422 412 406 402

Dalton et al. (2024) report one sample with an age of 245 Ma, and 4 samples with 252 Ma; these eruptive episodes are already included in Tappe et al. (2018).

Cluster 9: Africa, Angola

There is only one age provided by Tappe et al. (2018) for this cluster: 113 Ma, and we retain this age in our study.

Corresponding line number from Supplementary Table A from Tappe et al. (2018) is 740.

Dalton et al. (2024) have no data for this cluster.

Cluster 10: Africa, Angola, Lunda Sul

The ages provided by Tappe et al. (2018) for this cluster are reported below in Ma. The ages we keep for our study are underlined.

108 110 113 113 116 117 117.9 119 120 120 120 120.1 121.2 122 124 124 124.2 125.8 126 126 126 126.4 127 127.6 129 129 129 129 129 130 130 131 131 131.2 131.4 132 132 132.1 133 133 133 133 133 133.2 133.5 133.6 134 134 134 134.9 135 135 135 135 136 136 136 137 138 138 138.5 139 141 144 144 145 154

Corresponding line numbers from Supplementary Table A from Tappe et al. (2018) are as follows:

753 748 742 741 733 728 727 721 716 715 714 713 709 708 707 706 702 700 699 698 697 694 693 689 688 687 686 685 683 682 681 680 679 678 677 676 675 673 672 671 670 669 668 667 666 662 661 660 659 658 657 656 655 652 651 650 649 647 646 644 639 630 621 620 617 566

Dalton et al. (2024) report 3 samples with an age of 117 Ma; this eruptive episode is already included in Tappe et al. (2018).

Cluster 11: Africa, Congo

The ages provided by Tappe et al. (2018) for this cluster are reported below in Ma. The ages we keep for our study are underlined.

70 70 70 70 71 97 120 801

Corresponding line numbers from Supplementary Table A from Tappe et al. (2018) are as follows:

1035 1034 1033 1032 1030 799 718 163

Dalton et al. (2024) report 9 samples with an age of 71 Ma, and 13 samples with an age of 97 Ma; these eruptive episodes are already included in Tappe et al. (2018).

Cluster 12: Africa, Congo

There is only one age provided by Tappe et al. (2018) for this cluster: 68 Ma, and we retain this age in our study.

The corresponding line number from Tappe et al. (2018) is 1041.

Dalton et al. (2024) have no data for this cluster.

Cluster 13: Africa, Tanzania, Kaliua

There is only one age provided by Tappe et al. (2018) for this cluster: 0.012 Ma, and we retain this age in our study.

Corresponding line number from Supplementary Table A from Tappe et al. (2018) is 1133.

Dalton et al. (2024) report 44 samples with an age of 0.012 Ma; this eruptive episode is already included in Tappe et al. (2018).

Cluster 14: Africa, Tanzania, Shinyanga

The ages provided by Tappe et al. (2018) for this cluster are reported below in Ma. The ages we keep for our study are underlined.

<u>27</u> 43.9 46 47.3 51 51 52 54 54 57 60 60 60 66.7 67.7 <u>79.6</u> <u>1097</u> 1105 1115 <u>1149</u>.

Corresponding line numbers from Supplementary Table A from Tappe et al. (2018) are as follows:

1131 1127 1125 1124 1114 1113 1107 1098 1097 1082 1072 1071 1070 1044 979 182 117 98 90

Dalton et al. (2024) have no data for this cluster.

Cluster 15: Africa, Congo

The ages provided by Tappe et al. (2018) for this cluster are reported below in Ma. The ages we keep for our study are underlined.

25 29 33 <u>35</u>

Corresponding line numbers from Supplementary Table A from Tappe et al. (2018) are as follows:

1132 1130 1129 1128

Dalton et al. (2024) report 7 samples with an age of 32 Ma; this eruptive episode is already included in Tappe et al. (2018).

Cluster 16: Africa, Mozambique

The ages provided by Tappe et al. (2018) for this cluster are reported below in Ma. The ages we keep for our study are underlined.

139.2 <u>139.7</u>

Corresponding line numbers from Supplementary Table A from Tappe et al. (2018) as follows:

637 636

Dalton et al. (2024) have no data for this cluster.

Cluster 17: Africa, Zimbabwe

There is only one age provided by Tappe et al. (2018) for this cluster: 179 Ma, and we retain this age in our study.

Corresponding line number from Supplementary Table A from Tappe et al. (2018) is 497.

Dalton et al. (2024) have no data for this cluster.

Cluster 18: Africa, Botswana

The ages provided by Tappe et al. (2018) for this cluster are reported below in Ma. The ages we keep for our study are underlined.

81.4 <u>83.8</u>

Corresponding line numbers from Supplementary Table A from Tappe et al. (2018) as follows:

963 952

Dalton et al. (2024) have no data for this cluster.

Cluster 19: Africa, Botswana

There is only one age provided by Tappe et al. (2018) for this cluster: 87 Ma, and we retain this age in our study.

Corresponding line number from Supplementary Table A from Tappe et al. (2018) is 909.

Dalton et al. (2024) report 50 samples with an age of 87 Ma; this eruptive episode is already included in Tappe et al. (2018).

Cluster 20: Africa, Namibia

The ages provided by Tappe et al. (2018) for this cluster are reported below in Ma. The ages we keep for our study are underlined.

55 <u>59</u>

Corresponding line numbers from Supplementary Table A from Tappe et al. (2018) as follows:

1092 1077

Dalton et al. (2024) have no data for this cluster.

Cluster 21: Africa, Namibia, North of Hardap

The ages provided by Tappe et al. (2018) for this cluster are reported below in Ma. The ages we keep for our study are underlined.

61 <u>64</u> 67 72 72 72 73 76 78 <u>116</u>

Corresponding line numbers from Supplementary Table A from Tappe et al. (2018) are as follows:

1065 1055 1047 1027 1026 1025 1020 999 991 734

Dalton et al. (2024) report 2 samples with an age of 72 Ma, 5 samples with an age of 73 Ma, one sample with an age of 75.9 Ma, 8 samples with an age of 76 Ma, and 4 samples with an age of 77.9 Ma; these eruptive episodes are already included in Tappe et al. (2018).

Cluster 22: Africa, South Africa

There is only one age provided by Tappe et al. (2018) for this cluster: 72 Ma, and we retain this age in our study.

Corresponding line number from Supplementary Table A from Tappe et al. (2018) is 1028.

Dalton et al. (2024) report 2 samples with an age of 72 Ma; this eruptive episode is already included in Tappe et al. (2018).

Cluster 23: Africa, Botswana

The ages provided by Tappe et al. (2018) for this cluster are reported below in Ma. The ages we keep for our study are underlined.

<u>531</u> <u>583</u> <u>647</u>

Corresponding line numbers from Supplementary Table A from Tappe et al. (2018) are as follows:

247 201 185

Dalton et al. (2024) report one sample with an age of 531 Ma; this eruptive episode is already included in Tappe et al. (2018).

Cluster 24: Africa, Botswana

The ages provided by Tappe et al. (2018) for this cluster are reported below in Ma. The ages we keep for our study are underlined.

568 589

Corresponding line numbers from Supplementary Table A from Tappe et al. (2018) are as follows:

216 197

Dalton et al. (2024) have no data for this cluster.

Cluster 25: Africa, Botswana, East of Komondino

The ages provided by Tappe et al. (2018) for this cluster are reported below in Ma. The ages we keep for our study are underlined.

80.3 85 85.2 87.5 101.2 235

Corresponding line numbers from Supplementary Table A from Tappe et al. (2018) are as follows:

970 934 933 898 767 437

Dalton et al. (2024) have no data for this cluster.

Cluster 26: Africa, Botswana

The ages provided by Tappe et al. (2018) for this cluster are reported below in Ma. The ages we keep for our study are underlined.

82 86 87 87.4 91 94 94.3

Corresponding line numbers from Supplementary Table A from Tappe et al. (2018) are as follows:

956 921 907 900 854 823 821

Dalton et al. (2024) report one sample with an age of 82 Ma, one sample with an age of 86 Ma, 50 samples with an age of 87 Ma, and one sample with an age of 91 Ma; these eruptive episodes are already included in Tappe et al. (2018).

Cluster 27: Africa, Botswana, Lethakane

The ages provided by Tappe et al. (2018) for this cluster are reported below in Ma. The ages we keep for our study are underlined.

84 86.4 87 88 90.3 92 92 92 92.1 93 93 93 93 93 93.8 94 94.4 95 96 96.5 96.8 97.3 98 99 100 102.6 106 108.5 111 176

Corresponding line numbers from Supplementary Table A from Tappe et al. (2018) are as follows:

946 920 910 884 865 845 844 843 842 840 839 838 837 836 830 824 820 809 804 803 802 797 793 783 777 764 754 752 746 503

Dalton et al. (2024) report 50 samples with an age of 87 Ma, 16 samples with an age of 88 Ma, 4 samples with an age of 92 Ma, 4 samples with an age of 93 Ma, 65 samples with an age of 95 Ma, and 2 samples with an age of 100 Ma; these eruptive episodes are already included in Tappe et al. (2018).

Cluster 28: Africa, at the boundary between Botswana and Zimbabwe

There is only one age provided by Tappe et al. (2018) for this cluster: 1217 Ma, and we retain this age in our study.

Corresponding line number from Supplementary Table A from Tappe et al. (2018) is 43.

Dalton et al. (2024) have no data for this cluster.

Cluster 29: Africa, Zimbabwe

The ages provided by Tappe et al. (2018) for this cluster are reported below in Ma. The ages we keep for our study are underlined.

502 502 529 540 600 750

Corresponding line numbers from Supplementary Table A from Tappe et al. (2018) are as follows:

273 272 251 235 193 173

Dalton et al. (2024) have no data for this cluster.

Cluster 30: Africa, Zimbabwe

The ages provided by Tappe et al. (2018) for this cluster are reported below in Ma. The ages we keep for our study are underlined.

500 <u>538</u>

Corresponding line numbers from Supplementary Table A from Tappe et al. (2018) are as follows:

278 238

Dalton et al. (2024) report 4 samples with an age of 526 Ma and one sample with 539 Ma; these eruptive episodes are already included in Tappe et al. (2018).

Cluster 31: Africa, Zimbabwe

The ages provided by Tappe et al. (2018) for this cluster are reported below in Ma. The ages we keep for our study are underlined.

<u>431</u> 542 <u>550</u> <u>886</u>

Corresponding line numbers from Supplementary Table A from Tappe et al. (2018) are as follows:

309 232 226 159

Dalton et al. (2024) have no data for this cluster.

Cluster 32: Africa, Zimbabwe

The ages provided by Tappe et al. (2018) for this cluster are reported below in Ma. The ages we keep for our study are underlined.

536 670 1112 1115 1129 1156

Corresponding line numbers from Supplementary Table A from Tappe et al. (2018) are as follows:

241 180 92 89 74 55

Dalton et al. (2024) have no data for this cluster.

Cluster 33: Africa, at the boundary between South Africa and Zimbabwe

The ages provided by Tappe et al. (2018) for this cluster are reported below in Ma. The ages we keep for our study are underlined.

535 535 583

Corresponding line numbers from Supplementary Table A from Tappe et al. (2018) are as follows:

245 244 205

Dalton et al. (2024) have no data for this cluster.

Cluster 34: Africa, South Africa, near the boundary with Zimbabwe

The ages provided by Tappe et al. (2018) for this cluster are reported below in Ma. The ages we keep for our study are underlined.

511 519 522 525 533 540 549 572 631

Corresponding line numbers from Supplementary Table A from Tappe et al. (2018) are as follows:

266 262 259 254 246 236 229 213 189

Dalton et al. (2024) report 20 samples with an age of 519 Ma; this eruptive episode is already included in Tappe et al. (2018).

Cluster 35: Africa, Botswana and South Africa

The ages provided by Tappe et al. (2018) for this cluster are reported below in Ma. The ages we keep for our study are underlined.

493 500 500 507 508 509 512 513 520 521 522 528 634 1287 1333 1333 1333 1352 1352 1364

Corresponding line numbers from Supplementary Table A from Tappe et al. (2018) are as follows:

280 277 274 271 269 268 265 264 261 260 258 252 187 42 40 39 38 36 35 33

Dalton et al. (2024) report one sample with an age of 505 Ma, one sample with an age of 520 Ma, and one sample with an age of 1364 Ma; these eruptive episodes are already included in Tappe et al. (2018).

Cluster 36: Africa, South Africa

There is only one age provided by Tappe et al. (2018) for this cluster: 149 Ma, and we retain this age in our study.

Corresponding line number from Supplementary Table A from Tappe et al. (2018) is 595.

Dalton et al. (2024) have no data for this cluster.

Cluster 37: Africa, South Africa, South of Polokwane

The ages provided by Tappe et al. (2018) for this cluster are reported below in Ma. The ages we keep for our study are underlined.

75 155.1 160 200 330

Corresponding line numbers from Supplementary Table A from Tappe et al. (2018) are as follows:

1006 562 534 469 381

Dalton et al. (2024) have no data for this cluster.

Cluster 38: Africa, South Africa

The ages provided by Tappe et al. (2018) for this cluster are reported below in Ma. The ages we keep for our study are underlined.

99 157 158 165 210

Corresponding line numbers from Supplementary Table A from Tappe et al. (2018) are as follows:

791 545 543 528 459

Dalton et al. (2024) have no data for this cluster.

Cluster 39: Africa, South Africa

The ages provided by Tappe et al. (2018) for this cluster are reported below in Ma. The ages we keep for our study are underlined.

799 1078 1148.5 1150 1151 1154 1155 1180

The corresponding line numbers from Tappe et al. (2018) are as follows:

167 150 63 61 60 57 56 49

Dalton et al. (2024) report one sample with an age of 1147 Ma, and 28 samples with an age of 1198 Ma; these eruptive episodes are already included in Tappe et al. (2018).

Cluster 40: Africa, Eswatini

There is only one age provided by Tappe et al. (2018) for this cluster: 203 Ma, and we retain this age in our study.

The corresponding line number from Tappe et al. (2018) is 467.

Dalton et al. (2024) have no data for this cluster.

Cluster 41: Africa, South Africa, South of Johannesburg

The ages provided by Tappe et al. (2018) for this cluster are reported below in Ma. The ages we keep for our study are underlined.

85 89

Corresponding line numbers from Supplementary Table A from Tappe et al. (2018) are as follows:

940 874

Dalton et al. (2024) report 2 samples with an age of 89 Ma; this eruptive episode is already included in Tappe et al. (2018).

Cluster 42: Africa, South Africa

The ages provided by Tappe et al. (2018) for this cluster are reported below in Ma. The ages we keep for our study are underlined.

75.4 85 91 91 95 95.5 135.3

Corresponding line numbers from Supplementary Table A from Tappe et al. (2018) are as follows:

1003 938 859 856 815 808 654

Dalton et al. (2024) report one sample with an age of 91 Ma, and 65 samples with an age of 95 Ma; these eruptive episodes are already included in Tappe et al. (2018).

Cluster 43: Africa, South Africa and Botswana

The ages provided by Tappe et al. (2018) for this cluster are reported below in Ma. The ages we keep for our study are underlined.

92 117 129 138 139 153 157 200 204 509 1190 1390

Corresponding line numbers from Supplementary Table A from Tappe et al. (2018) are as follows:

849 731 690 648 642 572 546 470 466 267 46

Dalton et al. (2024) report 2 samples with an age of 92 Ma, and 3 samples with an age of 117 Ma; these eruptive episodes are already included in Tappe et al. (2018).

Cluster 44: Africa, Botswana

There is only one age provided by Tappe et al. (2018) for this cluster: 1386 Ma, and we retain this age in our study.

Corresponding line number from Supplementary Table A from Tappe et al. (2018) is 46.

Dalton et al. (2024) have no data for this cluster.

Cluster 45: Africa, Botswana

The ages provided by Tappe et al. (2018) for this cluster are reported below in Ma. The ages we keep for our study are underlined.

168 170 170 175 <u>177</u> 205 206 206 233 235 239 241 242 243 244 245 249 250 250 250 <u>252</u>

Corresponding line numbers from Supplementary Table A from Tappe et al. (2018) are as follows:

527 522 521 507 501 464 463 462 440 438 423 419 418 417 416 413 410 409 408 407 402

Dalton et al. (2024) report one sample with an age of 245 Ma, and 4 samples with an age of 252 Ma; these eruptive episodes are already included in Tappe et al. (2018).

Cluster 46: Africa, Botswana

The ages provided by Tappe et al. (2018) for this cluster are reported below in Ma. The ages we keep for our study are underlined.

<u>73.1</u> <u>220</u>

Corresponding line numbers from Supplementary Table A from Tappe et al. (2018) are as follows:

1018 453

Dalton et al. (2024) have no data for this cluster.

Cluster 47: Africa, Botswana and South Africa

The ages provided by Tappe et al. (2018) for this cluster are reported below in Ma. The ages we keep for our study are underlined.

78 <u>80</u>

Corresponding line numbers from Supplementary Table A from Tappe et al. (2018) are as follows:

989 975

Dalton et al. (2024) have no data for this cluster.

Cluster 48: Africa, at the boundary between Botswana and South Africa

There is only one age provided by Tappe et al. (2018) for this cluster: 87 Ma, and we retain this age in our study.

Corresponding line number from Supplementary Table A from Tappe et al. (2018) is 908.

Dalton et al. (2024) report 50 samples with an age of 87 Ma; this eruptive episode is already included in Tappe et al. (2018).

Cluster 49: Africa, South Africa

The ages provided by Tappe et al. (2018) for this cluster are reported below in Ma. The ages we keep for our study are underlined.

<u>1303</u> 1626 1643 <u>1647</u> 1674 1674 1695 <u>1705</u> <u>1835</u>

Corresponding line numbers from Supplementary Table A from Tappe et al. (2018) are as follows:

41 29 27 24 23 21 19

Dalton et al. (2024) have no data for this cluster.

Cluster 50: Africa, South Africa

There is only one age provided by Tappe et al. (2018) for this cluster: 114 Ma, and we retain this age in our study.

Corresponding line number from Supplementary Table A from Tappe et al. (2018) is 739.

Dalton et al. (2024) have no data for this cluster.

Cluster 51: Africa, Namibia,

The ages provided by Tappe et al. (2018) for this cluster are reported below in Ma. The ages we keep for our study are underlined.

60.7 <u>76</u> <u>314</u> <u>440</u> 507 525 <u>537.6</u>

Corresponding line numbers from Supplementary Table A from Tappe et al. (2018) are as follows:

1066 1000 389 304 270 253 239

Dalton et al. (2024) report 8 samples with an age of 76 Ma; this eruptive episode is already included in Tappe et al. (2018).

Cluster 52: Africa, Namibia, North of Karas

The ages provided by Tappe et al. (2018) for this cluster are reported below in Ma. The ages we keep for our study are underlined.

514 524 <u>541</u>

Corresponding line numbers from Supplementary Table A from Tappe et al. (2018) are as follows:

263 255 234

Dalton et al. (2024) have no data for this cluster.

Cluster 53: Africa, Namibia, West of Kara

The ages provided by Tappe et al. (2018) for this cluster are reported below in Ma. The ages we keep for our study are underlined.

317 392 500

Corresponding line numbers from Supplementary Table A from Tappe et al. (2018) are as follows:

388 322 276

Dalton et al. (2024) have no data for this cluster.

Cluster 54: Africa, South Africa, near boundary with Namibia

There is only one age provided by Tappe et al. (2018) for this cluster: 78.8 Ma, and we retain this age in our study.

Corresponding line number from Supplementary Table A from Tappe et al. (2018) is 986.

Dalton et al. (2024) have no data for this cluster.

Cluster 55: Africa, South Africa, near boundary with Namibia

There is only one age provided by Tappe et al. (2018) for this cluster: 74.1 Ma, and we retain this age in our study.

Corresponding line number from Supplementary Table A from Tappe et al. (2018) is 1009.

Dalton et al. (2024) have no data for this cluster.

Cluster 56: Africa, South Africa

The ages provided by Tappe et al. (2018) for this cluster are reported below in Ma. The ages we keep for our study are underlined.

54 62 68 69 77 81 86 105

Corresponding line numbers from Supplementary Table A from Tappe et al. (2018) are as follows:

1096 1062 1042 1038 994 968 927 757

Dalton et al. (2024) report one sample with an age of 86 Ma; this eruptive episode is already included in Tappe et al. (2018).

Cluster 57: Africa, South Africa

The ages provided by Tappe et al. (2018) for this cluster are reported below in Ma. The ages we keep for our study are underlined.

51.9 54.7 56 60.1 78.4 92

Corresponding line numbers from Supplementary Table A from Tappe et al. (2018) are as follows:

1109 1095 1086 1067 988 850

Dalton et al. (2024) report 4 samples with an age of 92 Ma; this eruptive episode is already included in Tappe et al. (2018).

Cluster 58: Africa, South Africa, South of Carnarvon and North of Worcester

The ages provided by Tappe et al. (2018) for this cluster are reported below in Ma. The ages we keep for our study are underlined.

66 66.2 68.2 75 76 109 367

Corresponding line numbers from Supplementary Table A from Tappe et al. (2018) are as follows:

1049 1048 1040 1007 1001 750 354

Dalton et al. (2024) report 8 samples with an age of 76 Ma; this eruptive episode is already included in Tappe et al. (2018).

Cluster 59: Africa, South Africa, South-east of Worcester

There is only one age provided by Tappe et al. (2018) for this cluster: 64 Ma, and we retain this age in our study.

Corresponding line number from Supplementary Table A from Tappe et al. (2018) is 1056.

Dalton et al. (2024) have no data for this cluster.

Cluster 60: Africa, South Africa, South-east of Worcester

There is only one age provided by Tappe et al. (2018) for this cluster: 63 Ma, and we retain this age in our study.

Corresponding line number from Supplementary Table A from Tappe et al. (2018) is 1060.

Dalton et al. (2024) have no data for this cluster.

Cluster 61: Africa, South Africa, South of Carnarvon

There is only one age provided by Tappe et al. (2018) for this cluster: 178 Ma, and we retain this age in our study.

Corresponding line number from Supplementary Table A from Tappe et al. (2018) is 498.

Dalton et al. (2024) have no data for this cluster.

Cluster 62: Africa, South Africa, North of Carnarvon

The ages provided by Tappe et al. (2018) for this cluster are reported below in Ma. The ages we keep for our study are underlined.

74 76.4 <u>82</u> 96.9 101 102 103 117 118 118 119 122 140 <u>143</u>

Corresponding line numbers from Supplementary Table A from Tappe et al. (2018) are as follows:

1016 998 959 801 774 765 763 729 726 725 722 711 633 627

Dalton et al. (2024) report 5 samples with an age of 76.4 Ma, one sample with an age of 82 Ma, 2 samples with an age of 103 Ma, 3 samples with an age of 117 Ma, and 28 samples with an age of 143 Ma; these eruptive episodes are already included in Tappe et al. (2018).

Cluster 63: Africa, South Africa, North of Prieska

The ages provided by Tappe et al. (2018) for this cluster are reported below in Ma. The ages we keep for our study are underlined.

74 <u>116</u>

Corresponding line numbers from Supplementary Table A from Tappe et al. (2018) are as follows:

1015 735

Dalton et al. (2024) have no data for this cluster.

Cluster 64: Africa, South Africa

The ages provided by Tappe et al. (2018) for this cluster are reported below in Ma. The ages we keep for our study are underlined.

73 81 89.6 <u>101</u>

Corresponding line numbers from Supplementary Table A from Tappe et al. (2018) are as follows:

1021 967 869 773

Dalton et al. (2024) have no data for this cluster.

Cluster 65: Africa, South Africa, South-East of De Aar

The ages provided by Tappe et al. (2018) for this cluster are reported below in Ma. The ages we keep for our study are underlined.

78 81.5 81.5 <u>91</u>

Corresponding line numbers from Supplementary Table A from Tappe et al. (2018) are as follows:

992 962 961 857

Dalton et al. (2024) report 4 samples with an age of 81.5 Ma; this eruptive episode is already included in Tappe et al. (2018).

Cluster 66: Africa, South Africa, South of Kimberley

The ages provided by Tappe et al. (2018) for this cluster are reported below in Ma. The ages we keep for our study are underlined.

86 91 <u>94.8</u>

Corresponding line numbers from Supplementary Table A from Tappe et al. (2018) are as follows:

929 858 818

Dalton et al. (2024) report one sample with an age of 86 Ma and one sample with an age of 91 Ma; these eruptive episodes are already included in Tappe et al. (2018).

Cluster 67: Africa, South Africa, South of Kimberley

The ages provided by Tappe et al. (2018) for this cluster are reported below in Ma. The ages we keep for our study are underlined.

79 86 90.4 97 100.5 105 111 <u>120</u>

Corresponding line numbers from Supplementary Table A from Tappe et al. (2018) are as follows:

983 928 864 800 775 756 747 719

Dalton et al. (2024) report one sample with an age of 86 Ma, 5 samples with an age of 90.4 Ma, and 13 samples with an age of 97 Ma; these eruptive episodes are already included in Tappe et al. (2018).

Cluster 68: Africa, South Africa, North of Kimberley

The ages provided by Tappe et al. (2018) for this cluster are reported below in Ma. The ages we keep for our study are underlined.

81 83 84 84 84 84.5 84.8 86 87 87 87 87.3 88 88 88.5 89 89 89.1 90 90 90.5 91 91 91.5 93.2 94 100 102 <u>108.7</u> 112 112 115 117 <u>159</u>

Corresponding line numbers from Supplementary Table A from Tappe et al. (2018) are as follows:

969 954 950 949 944 943 941 930 917 916 915 903 895 894 880 876 875 871 868 867 863 861 850 851 834 829 781 766 751 744 743 736 730 539

Dalton et al. (2024) report one sample with an age of 84 Ma, one sample with an age of 86 Ma, 16 samples with an age of 88 Ma, 2 samples with an age of 89 Ma, 74 samples with an age of 90 Ma, one sample with an age of 91 Ma, 2 samples with an age of 100 Ma, one sample with an age of 112 Ma, and 3 samples with an age of 117 Ma; these eruptive episodes are already included in Tappe et al. (2018).

Cluster 69: Africa, South Africa

The ages provided by Tappe et al. (2018) for this cluster are reported below in Ma. The ages we keep for our study are underlined.

82.1 85 86.5 88 92 92 94.3 <u>99.7</u>

Corresponding line numbers from Supplementary Table A from Tappe et al. (2018) are as follows:

955 939 919 896 848 847 822 782

Dalton et al. (2024) report 16 samples with an age of 88 Ma, one sample with an age of 86.5 Ma, and 3 samples with an age of 92 Ma; these eruptive episodes are already included in Tappe et al. (2018).

Cluster 70: Africa, South Africa

The ages provided by Tappe et al. (2018) for this cluster are reported below in Ma. The ages we keep for our study are underlined.

88.1 88.43 88.6 <u>90</u>

Corresponding line numbers from Supplementary Table A from Tappe et al. (2018) are as follows:

883 881 879 866

Dalton et al. (2024) report 74 samples with an age of 90 Ma; this eruptive episode is already included in Tappe et al. (2018).

Cluster 71: Africa, Lesotho

There is only one age provided by Tappe et al. (2018) for this cluster: 92.2 Ma, and we retain this age in our study.

Corresponding line number from Supplementary Table A from Tappe et al. (2018) is 841.

Dalton et al. (2024) have no data for this cluster.

Cluster 72: Africa, South Africa, near the boundary between Lesotho and South Africa

The ages provided by Tappe et al. (2018) for this cluster are reported below in Ma. The ages we keep for our study are underlined.

63 <u>82</u> 150 152 <u>194</u>

Corresponding line numbers from Supplementary Table A from Tappe et al. (2018) are as follows:

1059 958 588 579 477

Dalton et al. (2024) report one sample with an age of 82 Ma; this eruptive episode is already included in Tappe et al. (2018).

Cluster 73: Africa, boundary between Lesotho and South Africa

There is only one age provided by Tappe et al. (2018) for this cluster: 59.3 Ma, and we retain this age in our study.

Corresponding line number from Supplementary Table A from Tappe et al. (2018) is 1076.

Dalton et al. (2024) have no data for this cluster.

Cluster 74: Africa, Lesotho

The ages provided by Tappe et al. (2018) for this cluster are reported below in Ma. The ages we keep for our study are underlined.

88.8 89 91 92 94 <u>94.7</u>

Corresponding line numbers from Supplementary Table A from Tappe et al. (2018) are as follows:

878 872 855 846 828 819

Dalton et al. (2024) report 8 samples with an age of 85.7 Ma, 2 samples with an age of 89 Ma, one sample with an age of 91 Ma, and 4 samples with an age of 92 Ma; these eruptive episodes are already included in Tappe et al. (2018).

Cluster 75: Africa, South Africa, North of Umlazi

The ages provided by Tappe et al. (2018) for this cluster are reported below in Ma. The ages we keep for our study are underlined.

81 <u>103</u>

Corresponding line numbers from Supplementary Table A from Tappe et al. (2018) are as follows:

966 762

Dalton et al. (2024) report 2 samples with an age of 103 Ma; this eruptive episode is already included in Tappe et al. (2018).

Appendix Tables A.1: Our kimberlite cluster dataset. The columns display the present-day location of kimberlites (columns 1 and 2), the age of kimberlites (column 3), the corresponding line numbers in Tappe et al. (2018) Supplementary Table A (column 4), the backtracked location of kimberlites (columns 5 and 6), and the associated cluster number (column 7)

Present-day longitude	Present-day latitude	Age (Ma)	Line number	Backtracked longitude	Backtracked latitude	Cluster number
-8.8834	22.7668	154	567	3.3447	13.1106	1
-11.1417	12.9875	600	192	21.7479	-58.2023	2
-11.175	13.0083	1110	94	116.6278	-12.3846	2
-10.9833	8.6333	95	816	-8.7497	3.0383	3
-9.3127	8.8208	156	557	-5.3566	2.0774	3
-10.478579	7.312889	791	169	164.3901	-72.307	3
-10.478253	7.296504	841	161	40.7165	-79.6681	3

-1	6.5	2029	8	0	0	4
10.6878	-0.77614	708	176	37.6112	-46.2762	5
11.12496	0.89521	1850	17	0	0	5
11.65412	0.47105	2029	7	0	0	5
11.47773	0.58045	2235	3	0	0	5
11.61195	0.45386	2500	2	0	0	5
11.2756	0.89414	2848	1	0	0	5
14.8917	-5.8208	322	386	-15.3411	-51.6531	6
15.7728	-12.3431	136	653	2.8285	-26.3806	7
17.08915	-11.18863	252	402	-3.2295	-39.7794	8
18.63098	-9.64596	113	740	10.4646	-23.9117	9
20.8134	-8.4204	154	566	8.9175	-28.1096	10
23.6076	-6.1671	70	1032	21.4127	-23.1888	11
23.3635	-6.2869	120	718	15.736	-23.1423	11
23.6076	-6.1671	801	163	22.8055	-37.1556	11
25.100396	-6.438724	68	1041	23.1699	-23.4801	12
31.9167	-4.8667	0.012	1133	31.9168	-4.8725	13
33.4775	-4.8175	27	1131	33.9635	-12.087	14
33.7666	-5.2833	79.6	979	32.0663	-23.953	14
33.3429	-3.3759	1097	117	30.171	14.9634	14
32.9037	-4.1837	1149	62	22.6841	0.337	14
27.5667	-10.1167	35	1128	27.9034	-21.0943	15
35.020581	-12.558349	139.7	636	20.0043	-38.1647	16
31.39	-17.9013	179	497	19.5366	-38.6691	17
21.14181	-18.94705	83.8	952	14.8342	-34.9166	18
21.5333	-26.7833	87	908	12.0996	-42.1156	19
16.4111	-24.8694	59	1077	11.8849	-39.9935	20
17.5997	-25.0817	64	1055	12.0571	-40.5748	21
17.6778	-25.6792	116	734	-0.5742	-37.0466	21
20.0383	-26.7456	72	1028	12.7663	-42.8379	22

22.092199	-24.9867	531	247	149.288	-44.5321	23
29.8808	-22.17	583	205	129.0938	-45.9929	23
22.0205	-24.8995	647	185	122.9932	-36.7741	23
22.615	-24.5842	589	197	133.2631	-51.967	24
24.3908	-23.3042	101.2	767	12.62	-38.6017	25
24.194024	-23.084963	235	437	0.7728	-51.5307	25
24.718	-22.586	94.3	821	15.4144	-38.2974	26
25.6897	-21.5194	111	746	11.4378	-37.6232	27
25.37	-21.3078	176	503	10.0461	-39.405	27
28.0116	-21.4831	1217	43	-39.8981	-14.2188	28
28.876239	-19.791167	540	235	132.4885	-47.0077	29
28.967308	-19.811397	600	193	116.4056	-47.4234	29
28.891683	-19.789783	750	173	79.2797	-21.8979	29
30.6705	-20.5006	538	238	132.8358	-44.8375	30
31.0695	-21.1683	431	309	135.6207	-41.2113	31
31.0695	-21.1683	550	226	131.6466	-45.1327	31
31.08847	-21.204943	886	159	82.3293	-15.9004	31
30.6425	-21.5942	536	241	135.126	-43.649	32
30.6475	-21.5793	670	180	102.3424	-24.1462	32
30.6425	-21.5942	1156	55	5.8909	-28.0455	32
29.8808	-22.17	583	205	129.0938	-45.9929	33
29.317032	-22.435607	522	259	151.4755	-41.6751	34
29.3214	-22.434	572	213	134.4047	-45.3545	34
29.316432	-22.432107	631	189	117.8887	-38.0647	34
28.258	-22.946569	528	252	144.6469	-42.4792	35
28.319102	-22.999366	634	187	118.721	-37.6664	35
27.8627	-22.743	1287	42	-79.8085	-6.2341	35
27.8627	-22.743	1364	33	-88.1057	-14.1672	35
27.5024	-24.186	149	595	0.7956	-44.5991	36
29.319029	-24.222083	75	1006	24.2188	-41.9767	37

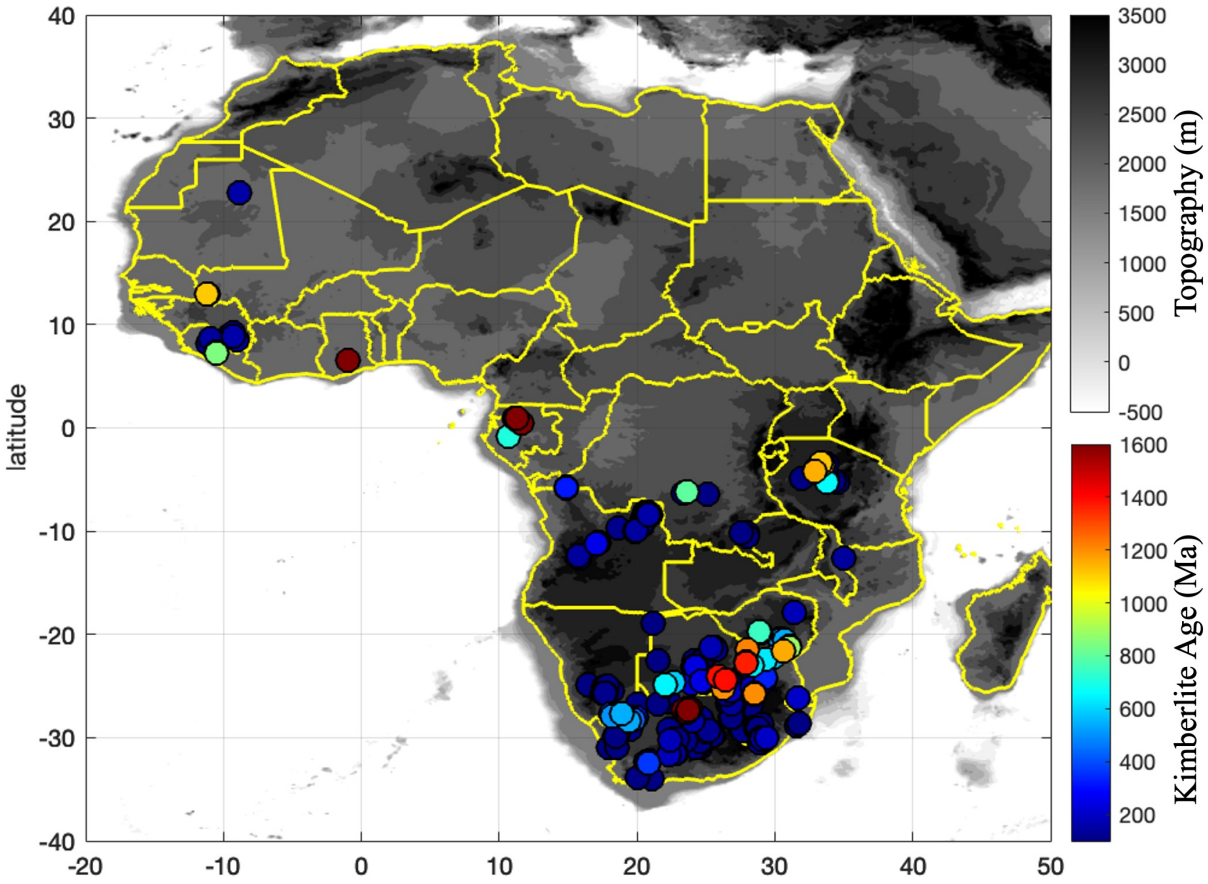
29.2388	-24.5006	200	469	17.5391	-44.9635	37
29.3193	-24.2214	330	381	-46.9489	-73.0346	37
28.3769	-25.1053	99	791	16.9787	-41.6049	38
28.367198	-25.106723	158	543	5.1604	-45.1776	38
28.3769	-25.1053	210	459	16.9826	-47.4241	38
28.530302	-25.760881	799	167	87.0393	-32.1183	39
28.5153	-25.6736	1078	150	60.9137	-14.9508	39
28.5153	-25.6736	1180	49	-19.5494	-29.9337	39
31.6381	-26.1353	203	467	19.974	-47.863	40
28.2781	-26.8914	89	874	19.5169	-43.5862	41
26.7556	-26.6736	85	938	18.7223	-43.498	42
26.8361	-26.7417	135.3	654	1.6519	-44.0219	42
26.9558	-25.3058	92	849	17.6236	-41.5833	43
27.391569	-25.252811	153	572	1.1372	-45.224	43
26.7417	-25.41	204	466	14.3493	-45.8979	43
26.4436	-24.501	509	267	171.262	-40.7867	43
26.2	-25.2833	1190	46	-27.8324	-25.0607	43
26.398	-24.3882	1390	31	-87.3305	-17.6636	43
25.8778	-24.1071	1386	32	-86.7336	-17.1347	44
24.930499	-24.218162	177	501	8.0339	-41.6872	45
24.7014	-24.5233	252	403	-10.5237	-54.1242	45
23.95	-24.5042	73.1	1018	17.9136	-41.3649	46
23.9968	-24.8115	220	453	9.754	-47.9069	46
22.2806	-26.4683	80	975	14.5904	-43.0002	47
21.5333	-26.7833	87	908	12.0996	-42.1156	48
23.597349	-27.551555	1303	41	-84.2196	2.0046	49
23.317042	-27.29467	1647	26	-100.9029	-27.8126	49
23.597349	-27.551555	1705	21	-76.8056	-26.55	49
23.721454	-27.282172	1835	19	0	0	49
22.3454	-29.1852	114	739	1.9399	-42.4774	50

19.7819	-28.3153	76	1000	11.4899	-44.2896	51
19.95	-28.0667	314	389	-44.5789	-63.5916	51
19.7819	-28.3153	440	304	148.4496	-24.6776	51
19.4375	-28.3625	537.6	239	151.3039	-45.1067	51
18.8597	-27.6233	541	234	150.1522	-46.7814	52
18.2653	-27.6492	317	388	-47.3335	-62.1884	53
18.1481	-27.7017	392	322	-170.7696	-71.5763	53
18.2	-27.95	500	276	-176.9684	-37.5923	53
18.693296	-29.287533	78.8	986	9.5028	-44.9656	54
19.526421	-29.211341	74.1	1009	11.1199	-45.1218	55
18.4269	-30.2192	54	1096	14.1301	-45.1247	56
18.460185	-29.947795	105	757	1.015	-42.1612	56
18.50408	-30.999637	92	850	5.4443	-44.5663	57
20.9364	-32.2447	109	750	0.0978	-44.849	58
20.7889	-32.5128	367	354	-165.2409	-62.5447	58
19.9931	-33.8783	64	1056	12.7636	-49.6076	59
21.0647	-34.0378	63	1060	14.4307	-49.8825	60
22.26919	-31.64742	178	498	0.1543	-46.7338	61
22.5394	-31.0342	82	959	12.8278	-47.195	62
22.7397	-31.5019	143	627	-9.1648	-45.6356	62
23.5042	-30.2506	116	735	1.541	-43.7421	63
24.6186	-30.3317	101	773	9.1757	-45.1235	64
24.2594	-31.0047	91	857	12.4445	-46.3407	65
25.419	-29.7623	94.8	818	12.884	-45.2571	66
25.19679	-29.320056	120	719	2.5074	-43.5006	67
24.5136	-28.1681	108.7	751	6.8405	-42.9811	68
24.0972	-28.4041	159	539	-1.3999	-45.1748	68
26.82881	-28.03544	99.7	782	13.5274	-43.8006	69
27.4222	-28.8111	90	866	17.5319	-45.1143	70
27.6359	-29.2955	92.2	841	16.7203	-45.568	71

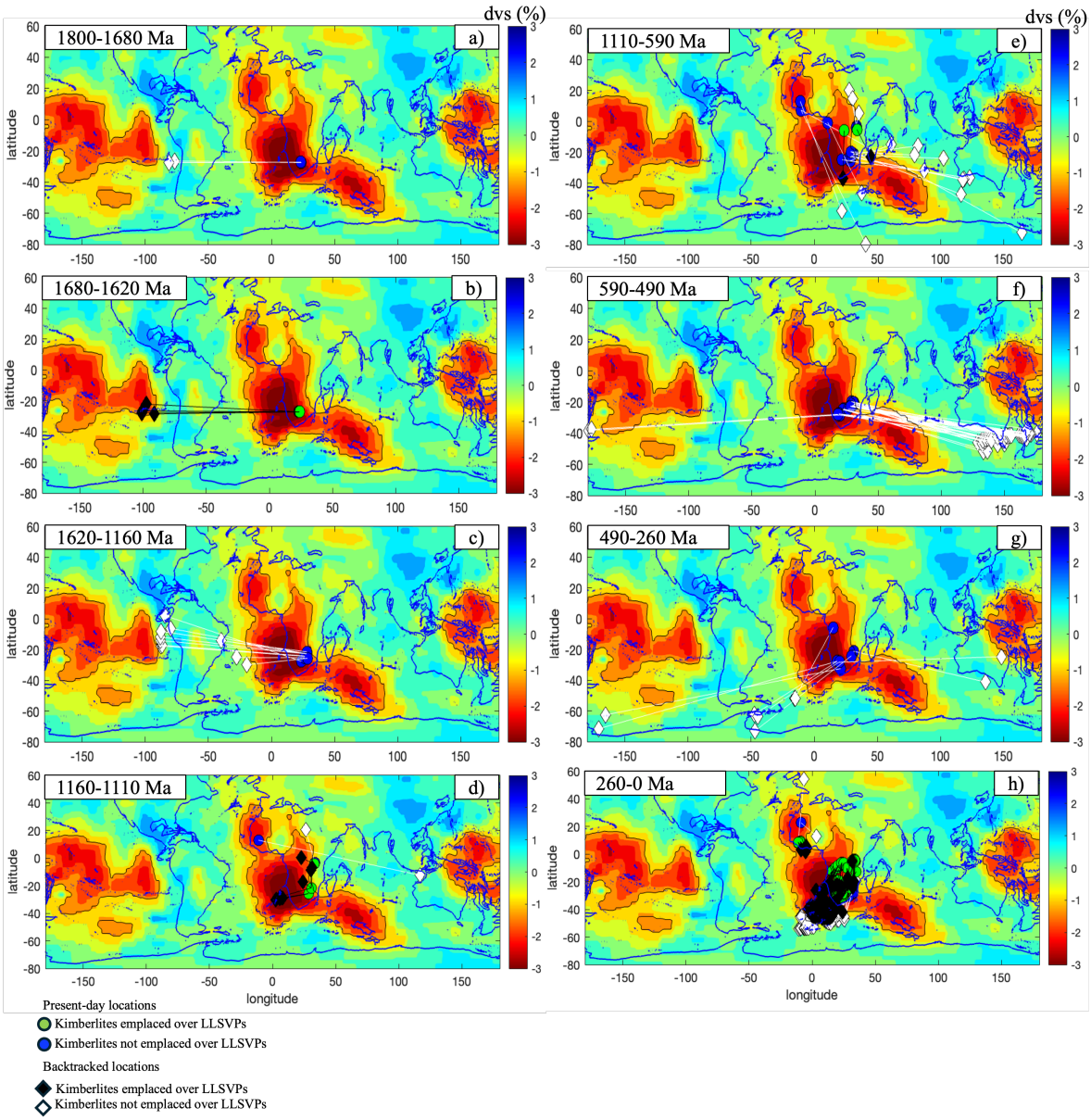
28.832998	-30.467002	82	958	20.815	-47.9411	72
29.3578	-30.0061	194	477	13.9189	-49.4204	72
28.2878	-28.6397	59.3	1076	25.5674	-44.972	73
28.738	-29.067	94.7	819	17.1362	-45.5746	74
31.5417	-28.85	103	762	16.9125	-46.2881	75

Appendix B - Results for "unclustered" kimberlites

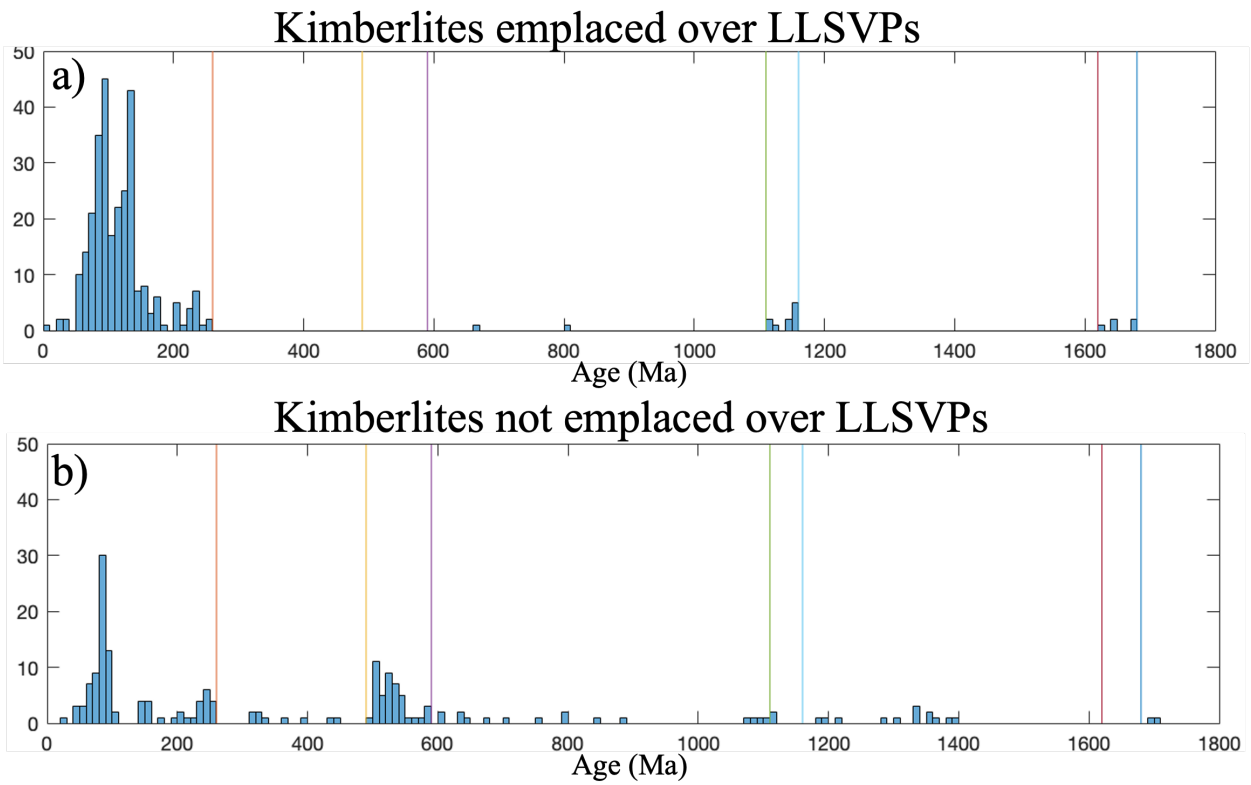
In this appendix, we present the results obtained using all "unclustered" kimberlite occurrences (i.e., without clustering) for the same analyses described in Chapters 4 and 5. This database encompasses all the data provided by the Tappe et al. (2018) database. The objective is to assess whether the spatial relationships identified using kimberlite clusters remain consistent when considering the full dataset. The same backtracking procedure, tomography models, and LAB datasets described in Chapter 3 were applied to the full kimberlite dataset. The interpretations of the figures are the same as the ones discussed in the main chapters.



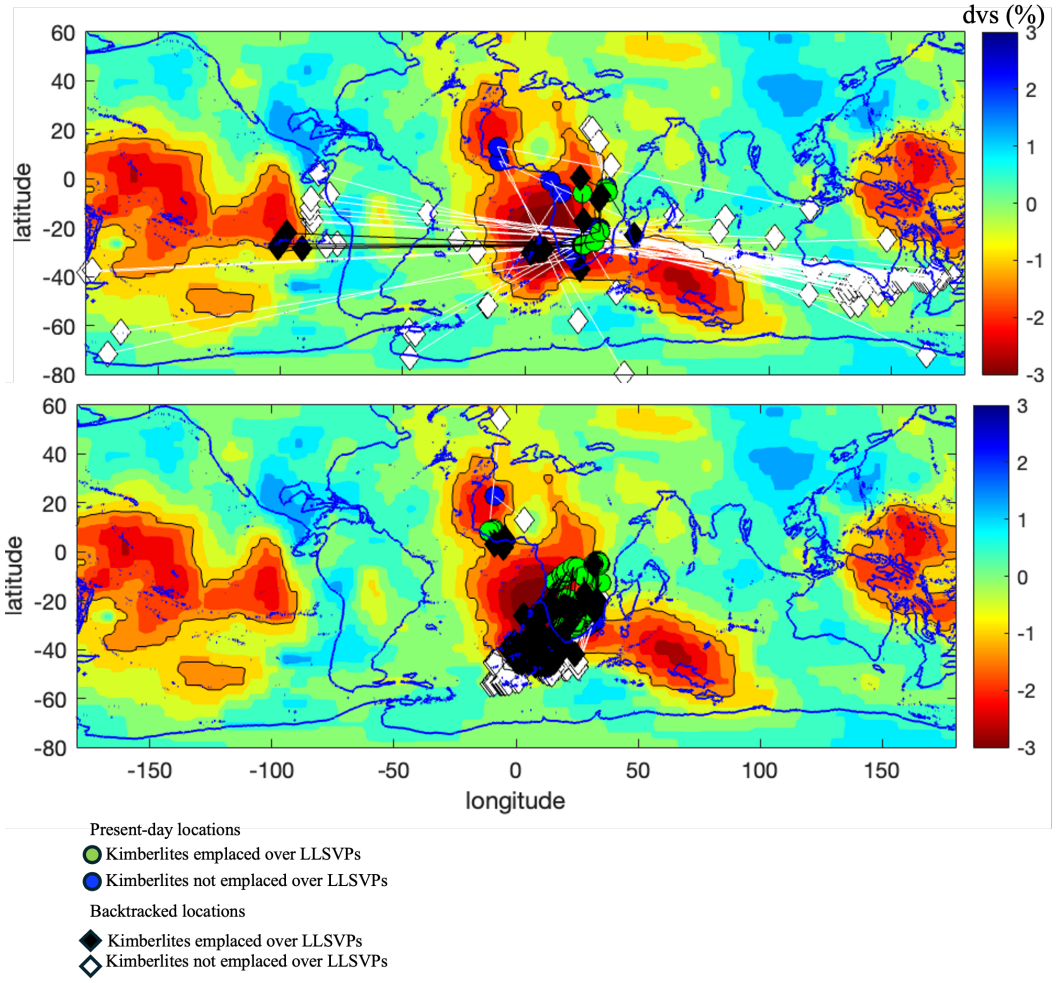
Appendix Figure B.1: The kimberlite database over the African continent. The color circles display the ages and locations of kimberlites. The grey colormap shows the topography; data from Tozer et al. (2019). The yellow lines are the country boundaries; data from ICPAC GEOPORTAL.



Appendix Figure B.2: Correlation between LLSVPs and backtracked kimberlite positions for the "unclustered data". The colormap shows the seismic velocity anomaly, dvs, near the core-mantle boundary provided by the TX2019slab tomography model (Lu et al., 2019). The LLSVP locations, that is, regions associated with negative seismic velocity anomalies, *dvs* are reported in red. The dvs = − 1% isocontour is reported in black. Isobath 0 is reported in blue. The present-day and backtracked locations of kimberlites emplaced over LLSVPs are displayed in green circles and black diamonds, respectively, whereas the present-day and backtracked locations of kimberlites not emplaced over LLSVP are displayed in blue circles and white diamonds, respectvely. Panels (a-h) show the reconstruction for different time periods.



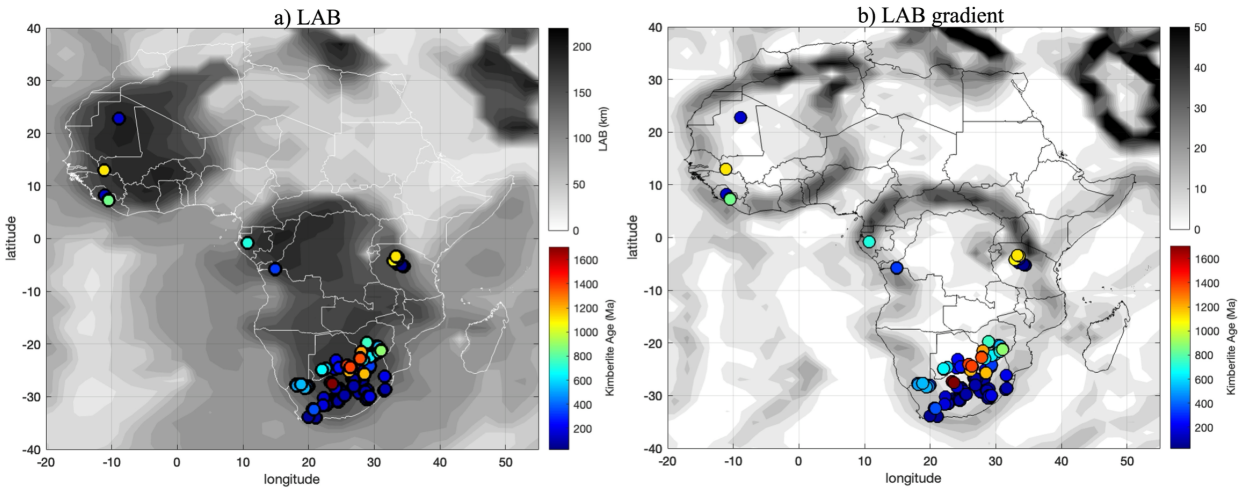
Appendix Figure B.3: Quantitative correlation between backtracked kimberlites positions and LLSVPs as a function of the kimberlites' age. The kimberlites clusters emplaced over LLSVPs are reported in panel a, while the ones not emplaced over LLSVPs are displayed in panel b. The correlation is based on three tomography models. The color lines represent the 260, 490, 590, 1110, 1160, 1620, 1680, and 1800 Ma, respectively.



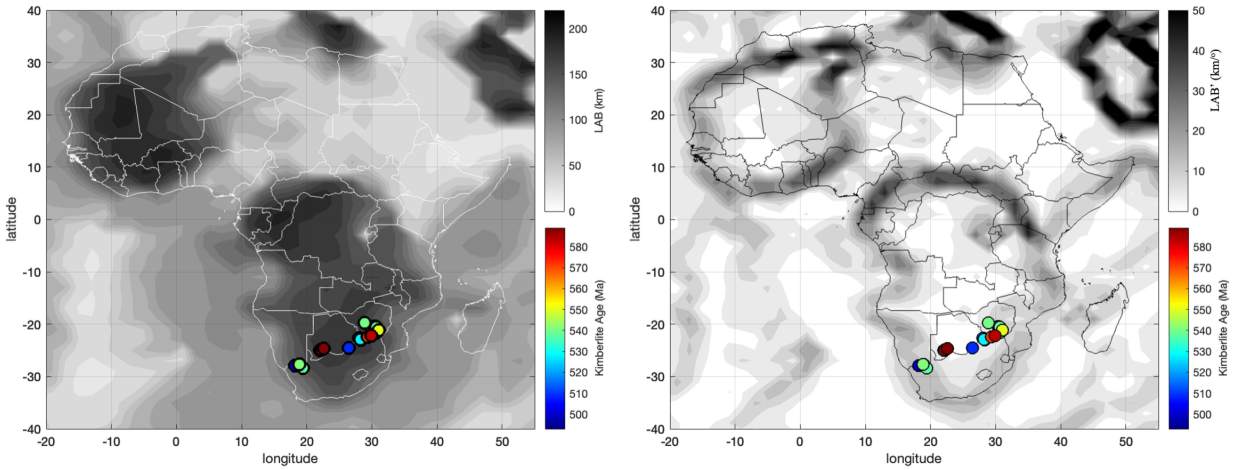
Appendix Figure B.4: Correlation between LLSVPs and all backtracked kimberlite positions. The colormap shows the seismic velocity anomaly, *dvs*, near the core-mantle boundary. The data are extracted from the TX2019slab tomography model (Lu et al. 2019). The LLSVP locations are reported in red, that is, associated with negative seismic velocity anomalies, *dvs*. The *dvs* = − 1% isocontour is reported in black. Isobath 0 is reported in blue. The present-day and backtracked locations of kimberlites emplaced over LLSVPs are displayed by green circles and black diamonds, respectively, while the present-day and backtracked locations of kimberlites not emplaced over LLSVP are displayed in blue circles and white diamonds. Panels a and b show the reconstruction for different time periods.

Appendix Table B.1: Summary of the correlation between all backtracked kimberlite positions and LLSVPs

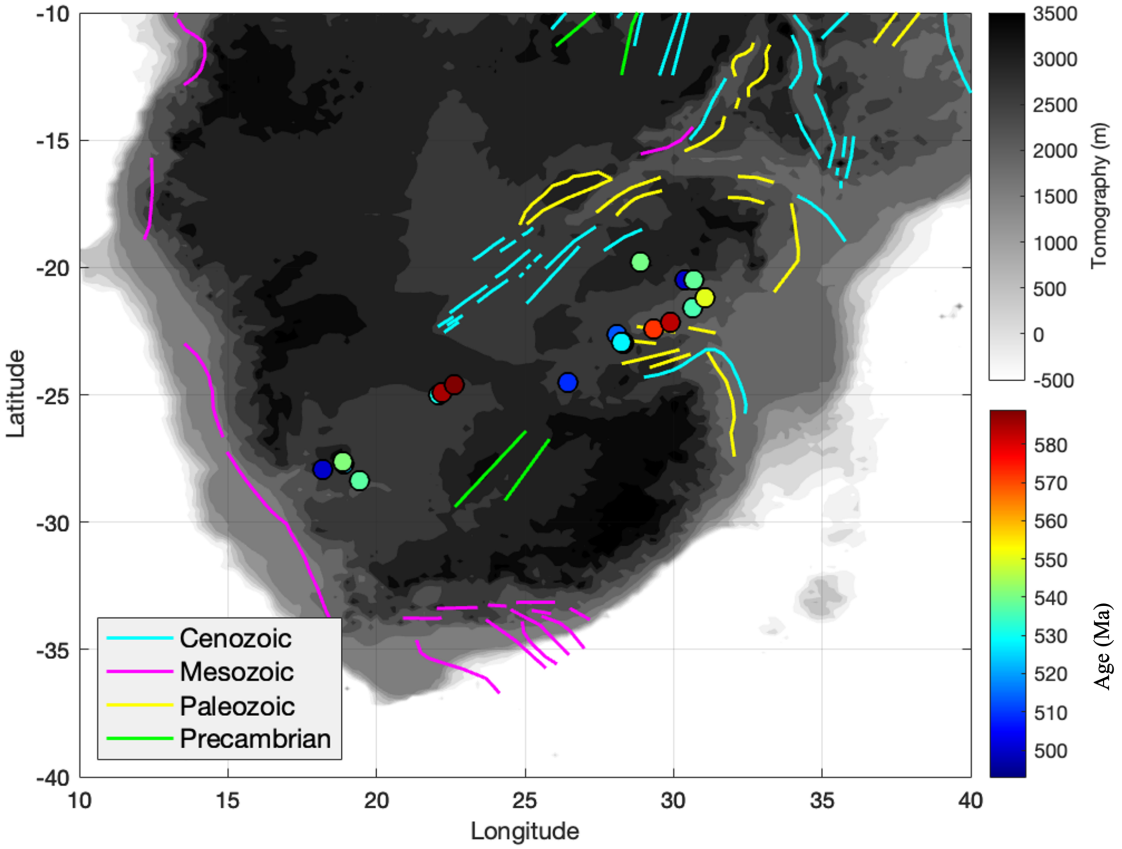
Periods (Ma)	Number of kimberlites	Number of kimberlites emplaced over LLSVPs	Percentage of kimberlites emplaced over LLSVPs	Number of kimberlites not emplaced over LLSVPs	Percentage of kimberlites not emplaced over LLSVPs
1800-260	103	17	16.5%	86	83.5%
260-0	378	282	74.6%	96	25.4%



Appendix Figure B.5: Lithosphere-Asthenosphere Boundary (LAB) and LAB gradient for all kimberlites not emplaced over LLSVPs. The colored circles display the ages and locations of kimberlites (1800-0 Ma not emplaced over LLSVPs). LAB shown in panel (a) obtained using data from Priestley et al. (2024). Panel (b) shows the corresponding LAB gradient. Country boundaries are shown as white lines in (a) and black lines in (b)



Appendix Figure B.6: Lithosphere-Asthenosphere Boundary (LAB), LAB gradient, and kimberlite clusters. The color circles display the ages and locations of kimberlites clusters with ages between 590 and 490 Ma. LAB shown in panel (a) obtained using data from Priestley et al. (2024). Panel (b) shows the corresponding LAB gradient. Country boundaries are shown as white lines in (a) and black lines in (b).



Appendix Figure B.7: Relationship between rift systems and kimberlite locations (590-490 Ma). Precambrian age (~ >541Ma) is reported in green, Paleozoic (~541-252 Ma) is reported in yellow, Mesozoic (~252-66 Ma) is reported in magenta, and Cenozoic (~66 to present) is reported in cyan. The color circles show kimberlite locations from the 490–590 Ma interval. The grey colormap shows the topography; data from Tozer et al. (2019).

Appendix Table B.2: All our kimberlite dataset. The columns display the present-day location of kimberlites (columns 1 and 2), the age of kimberlites (column 3), the corresponding line numbers in Tappe et al. (2018) Supplementary Table A (column 4), and the backtracked location of kimberlites (columns 5 and 6)

Present-day longitude	Present-day latitude	Age (Ma)	Line number	Backtracked longitude	Backtracked latitude
-8.8834	22.7668	154	567	3.3447	13.1106
-11.1417	12.9875	600	192	21.7479	-58.2023
-11.175	13.0083	1110	94	116.6278	-12.3846
-10.9833	8.6333	95	816	-8.7497	3.0383

-9.3127	8.8208	156	557	-5.3566	2.0774
-10.478579	7.312889	791	169	164.3901	-72.307
-10.478253	7.296504	841	161	40.7165	-79.6681
-1	6.5	2029	8	0	0
10.6878	-0.77614	708	176	37.6112	-46.2762
11.12496	0.89521	1850	17	0	0
11.65412	0.47105	2029	7	0	0
11.47773	0.58045	2235	3	0	0
11.61195	0.45386	2500	2	0	0
11.2756	0.89414	2848	1	0	0
14.8917	-5.8208	322	386	-15.3411	-51.6531
15.7728	-12.3431	136	653	2.8285	-26.3806
17.08915	-11.18863	252	402	-3.2295	-39.7794
18.63098	-9.64596	113	740	10.4646	-23.9117
20.8134	-8.4204	154	566	8.9175	-28.1096
23.6076	-6.1671	70	1032	21.4127	-23.1888
23.3635	-6.2869	120	718	15.736	-23.1423
23.6076	-6.1671	801	163	22.8055	-37.1556
25.100396	-6.438724	68	1041	23.1699	-23.4801
31.9167	-4.8667	0.012	1133	31.9168	-4.8725
33.4775	-4.8175	27	1131	33.9635	-12.087
33.7666	-5.2833	79.6	979	32.0663	-23.953
33.3429	-3.3759	1097	117	30.171	14.9634
32.9037	-4.1837	1149	62	22.6841	0.337
27.5667	-10.1167	35	1128	27.9034	-21.0943
35.020581	-12.558349	139.7	636	20.0043	-38.1647
31.39	-17.9013	179	497	19.5366	-38.6691
21.14181	-18.94705	83.8	952	14.8342	-34.9166
21.5333	-26.7833	87	908	12.0996	-42.1156
16.4111	-24.8694	59	1077	11.8849	-39.9935

17.5997	-25.0817	64	1055	12.0571	-40.5748
17.6778	-25.6792	116	734	-0.5742	-37.0466
20.0383	-26.7456	72	1028	12.7663	-42.8379
22.092199	-24.9867	531	247	149.288	-44.5321
29.8808	-22.17	583	205	129.0938	-45.9929
22.0205	-24.8995	647	185	122.9932	-36.7741
22.615	-24.5842	589	197	133.2631	-51.967
24.3908	-23.3042	101.2	767	12.62	-38.6017
24.194024	-23.084963	235	437	0.7728	-51.5307
24.718	-22.586	94.3	821	15.4144	-38.2974
25.6897	-21.5194	111	746	11.4378	-37.6232
25.37	-21.3078	176	503	10.0461	-39.405
28.0116	-21.4831	1217	43	-39.8981	-14.2188
28.876239	-19.791167	540	235	132.4885	-47.0077
28.967308	-19.811397	600	193	116.4056	-47.4234
28.891683	-19.789783	750	173	79.2797	-21.8979
30.6705	-20.5006	538	238	132.8358	-44.8375
31.0695	-21.1683	431	309	135.6207	-41.2113
31.0695	-21.1683	550	226	131.6466	-45.1327
31.08847	-21.204943	886	159	82.3293	-15.9004
30.6425	-21.5942	536	241	135.126	-43.649
30.6475	-21.5793	670	180	102.3424	-24.1462
30.6425	-21.5942	1156	55	5.8909	-28.0455
29.8808	-22.17	583	205	129.0938	-45.9929
29.317032	-22.435607	522	259	151.4755	-41.6751
29.3214	-22.434	572	213	134.4047	-45.3545
29.316432	-22.432107	631	189	117.8887	-38.0647
28.258	-22.946569	528	252	144.6469	-42.4792
28.319102	-22.999366	634	187	118.721	-37.6664
27.8627	-22.743	1287	42	-79.8085	-6.2341

27.8627	-22.743	1364	33	-88.1057	-14.1672
27.5024	-24.186	149	595	0.7956	-44.5991
29.319029	-24.222083	75	1006	24.2188	-41.9767
29.2388	-24.5006	200	469	17.5391	-44.9635
29.3193	-24.2214	330	381	-46.9489	-73.0346
28.3769	-25.1053	99	791	16.9787	-41.6049
28.367198	-25.106723	158	543	5.1604	-45.1776
28.3769	-25.1053	210	459	16.9826	-47.4241
28.530302	-25.760881	799	167	87.0393	-32.1183
28.5153	-25.6736	1078	150	60.9137	-14.9508
28.5153	-25.6736	1180	49	-19.5494	-29.9337
31.6381	-26.1353	203	467	19.974	-47.863
28.2781	-26.8914	89	874	19.5169	-43.5862
26.7556	-26.6736	85	938	18.7223	-43.498
26.8361	-26.7417	135.3	654	1.6519	-44.0219
26.9558	-25.3058	92	849	17.6236	-41.5833
27.391569	-25.252811	153	572	1.1372	-45.224
26.7417	-25.41	204	466	14.3493	-45.8979
26.4436	-24.501	509	267	171.262	-40.7867
26.2	-25.2833	1190	46	-27.8324	-25.0607
26.398	-24.3882	1390	31	-87.3305	-17.6636
25.8778	-24.1071	1386	32	-86.7336	-17.1347
24.930499	-24.218162	177	501	8.0339	-41.6872
24.7014	-24.5233	252	403	-10.5237	-54.1242
23.95	-24.5042	73.1	1018	17.9136	-41.3649
23.9968	-24.8115	220	453	9.754	-47.9069
22.2806	-26.4683	80	975	14.5904	-43.0002
21.5333	-26.7833	87	908	12.0996	-42.1156
23.597349	-27.551555	1303	41	-84.2196	2.0046
23.317042	-27.29467	1647	26	-100.9029	-27.8126

23.597349	-27.551555	1705	21	-76.8056	-26.55
23.721454	-27.282172	1835	19	0	0
22.3454	-29.1852	114	739	1.9399	-42.4774
19.7819	-28.3153	76	1000	11.4899	-44.2896
19.95	-28.0667	314	389	-44.5789	-63.5916
19.7819	-28.3153	440	304	148.4496	-24.6776
19.4375	-28.3625	537.6	239	151.3039	-45.1067
18.8597	-27.6233	541	234	150.1522	-46.7814
18.2653	-27.6492	317	388	-47.3335	-62.1884
18.1481	-27.7017	392	322	-170.7696	-71.5763
18.2	-27.95	500	276	-176.9684	-37.5923
18.693296	-29.287533	78.8	986	9.5028	-44.9656
19.526421	-29.211341	74.1	1009	11.1199	-45.1218
18.4269	-30.2192	54	1096	14.1301	-45.1247
18.460185	-29.947795	105	757	1.015	-42.1612
18.50408	-30.999637	92	850	5.4443	-44.5663
20.9364	-32.2447	109	750	0.0978	-44.849
20.7889	-32.5128	367	354	-165.2409	-62.5447
19.9931	-33.8783	64	1056	12.7636	-49.6076
21.0647	-34.0378	63	1060	14.4307	-49.8825
22.26919	-31.64742	178	498	0.1543	-46.7338
22.5394	-31.0342	82	959	12.8278	-47.195
22.7397	-31.5019	143	627	-9.1648	-45.6356
23.5042	-30.2506	116	735	1.541	-43.7421
24.6186	-30.3317	101	773	9.1757	-45.1235
24.2594	-31.0047	91	857	12.4445	-46.3407
25.419	-29.7623	94.8	818	12.884	-45.2571
25.19679	-29.320056	120	719	2.5074	-43.5006
24.5136	-28.1681	108.7	751	6.8405	-42.9811
24.0972	-28.4041	159	539	-1.3999	-45.1748

26.82881	-28.03544	99.7	782	13.5274	-43.8006
27.4222	-28.8111	90	866	17.5319	-45.1143
27.6359	-29.2955	92.2	841	16.7203	-45.568
28.832998	-30.467002	82	958	20.815	-47.9411
29.3578	-30.0061	194	477	13.9189	-49.4204
28.2878	-28.6397	59.3	1076	25.5674	-44.972
28.738	-29.067	94.7	819	17.1362	-45.5746
31.5417	-28.85	103	762	16.9125	-46.2881